ULTRA HIGH TEMPERATURE THERMAL INSULATION MATERIALS AND THE SIGNIFICANCE OF OPACIFICATION IN THE SUPPRESSION OF RADIATIVE TRANSPORT

ANAHITA PIRVARAM

A THESIS SUBMITTED TO THE FACULTY OF GRADUATE STUDIES
IN PARTIAL FULFILLMENT OF THE REQUIREMENTS FOR THE DEGREE OF
MATER OF APPLIED SCIENCE

GRADUATE PROGRAMME IN MECHANICAL ENGINEERING
YORK UNIVERSITY
TORONTO, ONTARIO

JANUARY 2022

© Anahita Pirvaram, 2022

Abstract

There is, nowadays, a large shift to high temperature operations in many applications such as industrial processes, power plants, and especially in the energy storage applications to reach a higher efficiency. Although some current thermal insulation materials show an excellent performance, they either don't withstand high temperatures above 1000 [°C] or have a poor thermal conductivity (higher than 0.3 [W m^{-1} K^{-1}]) at such high temperatures. Therefore, there is a strong need for developing advanced high temperature thermal insulation designs that withstand high temperatures (above 1000 [°C]) and have a good performance (thermal conductivity lower than 0.1 [W m^{-1} K^{-1}]) at such high temperatures. The aim of the present thesis is to achieve a new design of high temperature thermal insulation made with materials having high opacifying performance that tolerate high temperatures while having the minimum heat loss. At high temperatures, radiative heat transfer dominates over conduction and convection. Thus, the thesis focuses on the radiative heat transfer through the thermal insulation. To come up with a high-performance insulation design, first a multilayer insulation (MLI) design consisting of highly reflective shields placed in a low thermal conductive medium was considered. The performance of MLI design to suppress the radiation was investigated in the viewpoint of materials. A novel methodology was created to evaluate the performance of any types of material as shields in MLI design. It was revealed that maximizing reflectivity of the shields would result in a minimum radiative heat transfer. Then it was shown that metals as the highly reflective materials are the best options among the investigated materials. However, they will oxidize or, worse, melt at high temperatures which indicates the performance limitation of multilayer insulation design. In an example insulation structure, only one shield of copper could lower thermal conductivity to 0.08 [W m^{-1} K^{-1}]. However, it turns into copper oxide at high temperatures and 125 shields of copper oxide were needed to reach the same thermal conductivity which indicates the practical challenge with metals in high temperature MLI designs. Therefore, volumetric extinction design was considered as an alternative design. Volumetric design includes a large number of absorbing/scattering particles implanted into a low thermal conductive medium to suppress the radiation at high temperatures. Based on the Rayleigh theory, a numerical model was developed to predict the performance of a wide range of materials in volumetric insulation design. A novel methodology was developed to have a comprehensive investigation of materials to identify the most well performing materials. The investigation indicated that non-metals such as some oxides show a better performance to extinct the radiation in a volumetric approach. The results indicated that metal oxides perform mostly better than metals which is in favor of radiation extinction at high temperatures. At the end, the Lorentz oscillator model was used to understand how some materials are performing better than others to attenuate the radiation. In other words, this model is useful to capture the main effects on the opacifying behaviour of the materials.

Acknowledgments

First and foremost, I would like to give my warmest thanks to my supervisor, Professor Thomas Cooper for his invaluable advice, continuous support and patience during my master's study and research. His immense knowledge, guidance and advice kept me engaged with my research. Without his persistent help, thoughtful comments and recommendations this study would not have been done. I would like to thank my committee member, Professor Paul O'Brien, and the chair of my defense, Professor Simone Pisana for their brilliant comments and suggestions. I would also like to gratefully acknowledge the company of Synhelion SA for their financial contributions to this work. In addition, I am thankful to all my colleagues and friends at York University for their wonderful friendship and support. These people made my life and master's studies enjoyable. Last but not the least, I would like to thank my family for their continuous support throughout the time I spent on this research, and to those who were close, encouraging me to keep working as hard as I could to finish this thesis.

TABLE OF CONTENTS

LIST OF TABLES

LIST OF FIGURES

Chapter 1

Introduction

Thermal insulation, for many years, has attracted many interests due to its vast demand in many various industries such as HVAC market, buildings, thermal energy storage units, chemical process systems, pipelines, and space industry.

Thermal insulation refers to a low thermal conductivity material, or a specific structure of combined materials, that reduces the heat transfer rate significantly between the system and the ambient or between two regions of a system. Although the main benefit of thermal insulation is to decrease the heat losses and running expenses, using a proper insulation design provides many other advantages such as; controlling the system temperature resulting in a better operation control, lowering heat losses, and protecting the system from corrosion, extreme ambient temperature and vibration [1].

The selection of the type of thermal insulation depends on many thermal and physical properties to be considered. The main factors are:

- Low effective thermal conductivity which quantifies the capability of the insulation system to block the heat flow.
- Low density which determines the mass of material per unit volume which affects the design of insulation system.
- High compressive strength which determines the durability of the insulation and its resistance against external pressures and vibration.

Another important factor to be considered is the service temperature range which is the temperature range within which the insulation performs properly and sustains all its properties. Non-combustible, non-toxic, non-corrosive, ease of installation and resistance against moisture are other significant characteristics for thermal insulation [2].

There is, nowadays, a large shift to high temperature operations in many applications such as industrial processes, power plants, and specially in the energy storage applications [3][4][5][6][7]. For power plant applications, an increase in the temperature generally results in an increased thermal efficiency. In terms of energy storage, energy can be stored with a high density and the round-trip efficiency can be higher at high temperatures [7]. Therefore, there is a strong need for developing advanced high temperature thermal insulation designs that withstand high temperatures (above 1000 ℃) and have a good performance at such high temperatures. Before reviewing the current thermal insulation systems, it is necessary to describe the function of heat transfer in thermal insulation.

1.1 Heat transfer in thermal insulation

Understanding the heat transfer mechanism through the thermal insulation medium is of fundamental importance, since it will help guide the insulation design to minimize heat transfer rate through the medium.

Heat transport through a medium occurs via three modes: conduction, convection and radiation. Conduction heat transfer is the transport of internal energy due to microscopic collisions and movements of energy carriers such as atoms, molecules, electrons and phonons. In a porous medium, conduction heat transfer occurs through the gaseous and solid phases [8]. However, reducing the scale of pores limits the motion of molecules and decreases the gaseous heat conduction. The reason is that the gaseous heat conduction is highly dependent on the ratio of the pore scale and the mean free path of gas molecules which is the mean distance traveled by a molecule before colliding with other molecules. If the pore size is less than the mean free path of the gas, the gaseous heat conduction reduces significantly [9]. The convection heat transfer is caused by the bulk motion of gas or liquid molecules which transports the energy. Most insulation materials have small enough gas volumes that the convection heat can be negligible. However, for insulation materials with high porosity and large pores, the convection effects may need to be included. Radiation heat transfer is due to the exchange of electromagnetic radiation (photons) caused by thermally induced motion in materials. It happens through the emission, absorption and scattering (including reflection, refraction, diffraction and re-scattering of energy) mechanisms [10]. Unlike conduction and convection, radiation can be transferred in the absence of matter and can travel a large distance before transferring its energy.

To describe the heat transfer rate passing through a slab of thermal insulation, assume that the bottom surface is exposed to a high temperature and the top surface maintains a lower temperature. The one-dimensional total heat flux that flows through the medium can be described by Fourier's law as:

$$q = \frac{k_{\text{eff}} \mathit{\Delta} T}{L} \tag{1.1}$$

Where k_{eff} is the effective thermal conductivity in [W m^{-1} K^{-1}], L in [m] is the thickness of the medium along which the heat flows, $\mathit{\Delta} T$ in [K] is the temperature difference between the bottom and the top surface. In this formulation, k_{eff} is an effective property, and not a material property, which captures many details of the heat transfer behavior of the system (including material transport properties, geometry, etc.). k_{eff} considers all three heat transfer modes and includes conductive thermal conductivity (k_{cond}), convective thermal conductivity (k_{conv}) and radiative thermal conductivity (k_{rad}) as:

$$k_{\text{eff}} = k_{\text{cond}} + k_{\text{conv}} + k_{\text{rad}} \tag{1.2}$$

The heat transfer coefficient is a parameter that defines how well heat flows through a series of thermal resistances and can be defined by Newton's cooling law which indicates that the heat transfer rate from an objective to its surrounding is proportional to the temperature difference between them. The heat transfer coefficient is defined through Newton's law of cooling as:

$$q = h_{\text{eff}}(T_1 - T_2) \tag{1.3}$$

where h_{eff} is the heat transfer coefficient in [W m^{-2} K^{-1}], T_1 and T_2 in [K] are the temperature of the objective and its surrounding, respectively.

Equating Fourier's law and Newton's low cooling, allows the effective heat transfer coefficient can be expressed as:

$$h_{\text{eff}} = \frac{k_{\text{eff}}}{L} \tag{1.4}$$

Equation (1.4) includes all three heat transfer modes.

The Stefan Boltzmann's law gives the radiative heat power from a blackbody. This law indicates that the total emissive power of a blackbody (the total energy per time per surface area over all wavelength) is proportional to the fourth power of its temperature as:

$$E_{\text{b}} = \sigma T^4 \tag{1.5}$$

Where $\sigma \cong 5.67 \times 10^{-8}$ [W m^{-2} K^{-4}] is the Stefan Boltzmann constant and T in [K] is the temperature of the blackbody. Real bodies emit a fraction of blackbody's total emissive power which depends on their emissivity, ε. Then, the radiative power from a real body is:

$$E = \varepsilon\sigma T^4 \tag{1.6}$$

Considering the slab of thermal insulation mentioned before, the simple radiative heat exchange from its hot bottom to the cool top surface would be:

$$q_{\text{rad}} = \varepsilon_{\text{eff}}\sigma(T_1^4 - T_2^4) \tag{1.7}$$

where ε_{eff} is the effective emissivity of the insulation medium.

In thermal insulation, the convective heat transfer can be neglected. The reason is that convection happens due to the bulk movement of molecules of fluids and most insulation materials have small enough gas volumes that the convection heat can be negligible. Considering the radiation and conduction heat transfer modes in thermal insulation, radiation dominates over conduction at high temperatures, when convection is not present in the medium. To support this, we consider a slab of insulation that is maintained at temperature T_2 in the bottom and its top surface has temperature of T_1 ($T_2 > T_1$). We want to show the contribution of radiation and conduction to the heat flux by increasing T_2 and T_1 with a constant temperature difference of $\Delta T = 100$ [K]. To do this, we calculate the conductive and radiative heat flux by fairly assuming that the thermal conductivity is $k_{\mathrm{cond}} = 0.1$ [W m^{-1} K^{-1}], $\varepsilon_{\mathrm{eff}} = 0.02$ (as typical values for a well performing thermal insulation material [11]) and the thickness of insulation is $L = 10$ [cm] by:

- $q_{\mathrm{cond}} = k_{\mathrm{cond}}(T_2 - T_1)/L$
- $q_{rad} = \varepsilon_{\mathrm{eff}}\sigma(T_2^4 - T_1^4)$

Figure 1.1 shows the temperature dependency of the conductive and radiative heat flux which were calculated based on the assumptions. As can be seen, the contribution for conduction is relatively constant (by assuming that k_{cond} is constant) by increasing temperature, whereas the radiation heat flux increases significantly (by taking $\varepsilon_{\mathrm{eff}}$ constant). Although radiation has a small contribution at room temperatures, it begins to dominate over conduction by raising temperature so that conductive heat flux can be neglected at high temperatures.

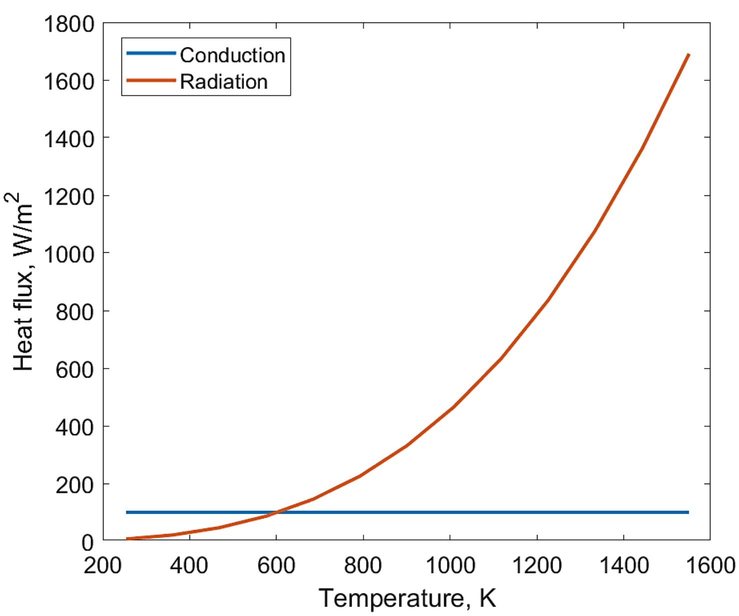

Figure 1.1. Temperature dependency of the conductive and radiative heat flux.

As explained, by considering that the insulation material has a low thermal conductivity, the heat loss by the conduction and convection can be neglected compared to the radiative heat loss, when it comes to high temperatures. Therefore, the focus of the thesis is to control the radiative heat transfer through the medium at high temperatures.

Now if we assume that the thermal insulation is exposed to a high temperature and radiation is the only way by which thermal energy can be transferred, then we can express the connection between effective thermal conductivity and the radiative heat transfer coefficient by considering equations (1.3), (1.4), and (1.7) as:

$$\frac{q}{\Delta T} = \frac{k_{\mathrm{eff}}}{L} = h_{\mathrm{rad}} = \frac{\varepsilon_{\mathrm{eff}}\sigma(T_1^4 - T_2^4)}{(T_1 - T_2)} = 4\varepsilon_{\mathrm{eff}}\sigma T_m^3 \tag{1.8}$$

Where h_{rad} is the effective radiation heat transfer coefficient and T_m in [K] is a representative average of T_1 and T_2 as $T_{\mathrm{m}} = \sqrt[3]{(T_1 + T_2)(T_1^2 + T_2^2)/4}$.

Equation (1.8) shows the relationship between the effective thermal conductivity k_{eff} and the effective emissivity $\varepsilon_{\mathrm{eff}}$ and indicates that the effective emissivity is the most important parameter to evaluate the performance of thermal insulation at high temperatures. Therefore, it is important to design a thermal insulation system with the lowest effective emissivity to minimize the radiative heat loss.

1.2 Current thermal insulation systems

There are several methods to design high performance thermal insulation with a low thermal conductivity such as; 1) achieving a porous structure inside the insulation material and filling the pores with a low thermal conductive gas or air, 2) producing vacuum inside the insulation, 3) embedding opacifiers in the insulation medium. The first two methods supress conduction and convection, whereas the third method suppresses the radiation. Accordingly, some high-performance thermal insulation designs have been developed to minimize the heat loss. Among them, some new developments such as vacuum insulation panels (VIPs), multilayer radiation shield thermal insulation systems (MLI), and aerogels can be mentioned. Aerogels are one of the newest thermal insulating materials which have a low density (high porosity) and low thermal conductivity (around 0.03 $[\mathrm{W\ m^{-1}\ K^{-1}}]$) [12]. The heat transfer through the aerogels can be defined by solid skeleton conduction, gaseous conductivity through porosities, and radiative heat transfer. Due to the nano-scaled porosity, the convection can be ignored in aerogel thermal insulations. Therefore, the heat transfer depends considerably on the thermal and optical properties of the materials used in the aerogels. Although, aerogels are considered as one of the promising thermal insulation materials because of their low thermal conductivity, thermal resistance degradation of aerogels is one of their drawbacks which is attributed to some physical changes in their porosity structure over time [13]. Based on the literature, the thermal stability of most commonly used aerogels is reported to be limited in range $280 - 470$ [℃] which seriously limits the application of aerogels at high temperatures [14][15][16][17].

Vacuum insulation panels (VIPs) are another type of newly developed thermal insulations with a low thermal conductivity typically between 0.004-0.02 $[\mathrm{W\ m^{-1}\ K^{-1}}]$ [18][19]. Most of the commercial VIP products have operational temperature lower than 100 [℃] [19]. VIPs consist of an evacuated open-porous core material placed inside a multilayer envelope and getters and desiccants. The function of core is physically supporting the envelope while maintaining the vacuum level inside the panel. The pore size of core material needs to be very small to reduce the gaseous conductivity (heat conduction that happens through the gas phase). An open pore structure is preferable to easily allow the evacuation of gas. Fumed silica, silica aerogel, polyurethane foam, fiberglass, and fiber/powder composites are some most commonly used core materials [18][20][21]. The envelope normally consists of three thin layers: the outer protective layer protects the panel against physical damages, the, the barrier layer which supports the insulation from transmission of moisture, air, and other gases and the inner sealing layer which seals the core material [18][21]. Getters and desiccants absorb the moisture and gases inside the panel to maintain the vacuum level. Figure 2 shows the schematic of a typical VIP.

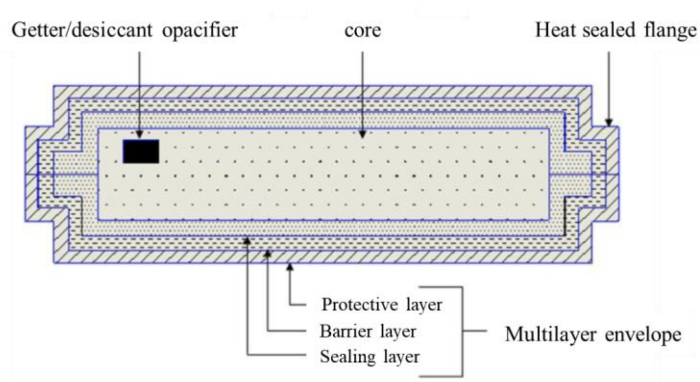

Figure 1.2. Schematic of a typical VIP [18].

In VIPs, radiation is an important heat transfer mode due to the vacuum conditions. In some advanced VIPs, absorbing/scattering particles such as silicon carbide, carbon black and titanium dioxide are added to the core material to reduce the radiative heat transfer

[18][22][23]. An increase in the density of the core material results in increasing solid conduction while decreasing the radiative transfer contribution since the optical density of the medium increases. Although VIPs have desirable thermal insulation properties, high thermal resistance, and low density, their application in high temperature processes has still remained limited. The main limitations for VIPs are their high cost in comparison to current insulation materials and their susceptibility to mechanical damages which decrease their reliability and eclipse their high performance [20].

A multilayer radiation shield thermal insulation system (MLI) consists of highly reflective thin shields placed parallel to each other to suppress radiation heat transfer and low thermal conductive spacers are arranged in between the shields. The spacers need to be selected from a material with a low enough thermal conductivity such that the conduction contribution remains low compared to the radiative contribution. In MLI systems, the heat transfer occurs by solid and gas conduction and radiation simultaneously. The results of studies show that the emissivity of shield has a significant influence on the effective thermal conductivity [24]. According to the literature, MLI systems have been a subject of interest to not only high temperature applications but also cryogenic conditions [25]. High temperature MLI materials normally have maximum operational temperature of 1000 [℃]. Although MLI systems have a very low thermal conductivity (lower than 0.1 [$\mathrm{W\,m^{-1}\,K^{-1}}$]) [26], they are not a good option for ultra high temperatures (above 1000 [℃]) as metallic reflective shields cannot survive at such high temperatures (they will oxidize or melt in the worst case).

Ultratherm is a commercial example of a high efficiency thermal insulation that has a microporous structure. This insulation design utilizes fumed silica nanoparticles as an opacifier inside its structure to suppress the radiation. Ultratherm not only has a lower thermal conductivity compared to other microporous insulation materials (lower than 0.1 [$W\ m^{-1}\ K^{-1}$]) but also shows a higher compressive strength. Although his insulation material maintains a good thermal resistance at high temperatures up to 950 [℃] [81], it is not a good option for ultra high temperatures (above 1000 [℃]).

There are several conventional high temperature thermal insulation materials such as mineral wool, insulating fire bricks, and refractory fiber glass. High temperature mineral wool insulation is a type of fibrous material that is created by mineral or rock materials. High temperature mineral wool insulation materials have good temperature resistance with operating temperatures up to 1600 [℃]. Although they can withstand very high temperatures, they have a poor thermal conductivity compared to the newly developed thermal insulation designs [27][82]. High temperature mineral wool insulation is commonly used in high temperature industrial processes due to its high thermal resistance. Insulating fire bricks is another type of high temperature insulation material that has operating temperature as high as 1800 [℃] depending on their classification. Insulating fire bricks are shaped refractory products and aluminium silicate is one of their most commonly used forms. They have a porous structure which lowers their thermal conductivity substantially. Generally, their thermal conductivity depends on the chemical composition, pore structure and the density [28]. Similar to mineral wool insulation, insulating fire bricks have a poor thermal conductivity compared to other new insulation materials. They are widely used in industrial applications, especially in furnace insulation or combustion chamber linings [82]. Refractory glass fiber insulation materials are a high temperature insulation product. They are usually produced with different density ($60 - 350$ [kg m^{-3}]) which influences their effective thermal conductivity. The main advantage of refractory glass fiber insulation is its high thermal resistance. However, its thermal conductivity increases significantly with increasing the temperature [29].

1.3 Research gap and objectives

Figure 1.3 shows the thermal conductivity of several current insulation materials as a function of temperature.

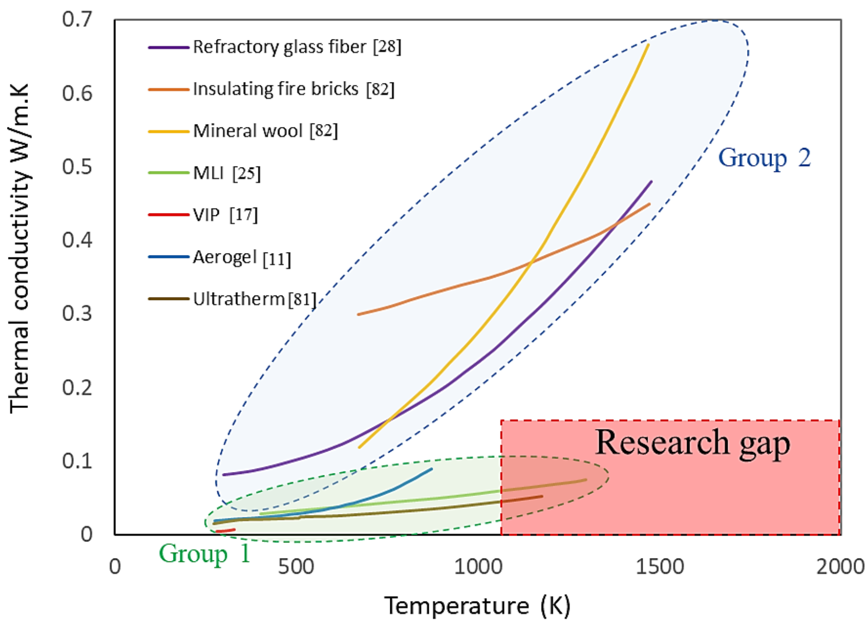

Figure 1.3. Temperature dependency of thermal conductivity for some insulation materials.

The current thermal insulation materials can be classified into two main groups; the first group is the high performance thermal insulation materials that represent a satisfactory performance for suppressing heat flow resulting in a low thermal conductivity (mostly lower than 0.1 $[\mathrm{W\,m^{-1}\,K^{-1}}]$).. However, their service temperature range is lower than 1000 $[\mathrm{°C}]$ and they are not suitable for higher temperatures. The second group is high temperature thermal insulation materials with a high thermal resistance at high temperatures, however their thermal conductivity is high compared to the first group. As shown in Figure 1.3, their thermal conductivity increases with increasing the temperature which disqualifies them for suppressing the heat flow at high temperatures. Therefore, the research gap in this field is the development of a new generation of high performance - high temperature thermal insulation materials which presents excellent thermal insulation properties (low thermal conductivity around 0.1 $[\mathrm{W\,m^{-1}\,K^{-1}}]$ at high temperatures) yet withstand ultra-high temperatures (above 1000 $[\mathrm{°C}]$).

In the present work, two research objectives have been established according to the research gap that exists in the field of high temperature thermal insulation. Two thermal insulation designs, multilayered insulation design (MLI) and volumetric extinction design, have been considered to investigate their performance looking from a materials point of view. The aim is to create a methodology to understand the behaviour of materials when we use them in each design. For this purpose, first, the most important material properties affecting radiation suppression are determined. Based on that, the best performing materials for each design are identified and their applicability to high temperatures is assessed. Accordingly, the main research goal is the development of a materials-focused pathway to improve the performance of high temperature thermal insulation by suppression of radiative transport and we specify the objectives as:

- Objective 1: to develop a methodology to predict the performance of Multilayered Shielding Insulation Design to suppress radiation. We will show that reflectance of shields is a main material property that determines the performance of the insulation design in the view of radiative transport. Then we will generate a universal performance plot of reflectance to identify the high-performance materials to suppress radiation. Finally, we will highlight the practical limits of MLI design for high temperature applications and will select the volumetric design as an alternative approach.
- Objective 2: to develop a methodology to investigate the performance of Volumetric Extinction Design to suppress radiation. It will be shown that extinction coefficient is the main material property to evaluate the performance of volumetric design. We will develop a universal performance plot for extinction coefficient by which we can compare materials. Then we identify promising materials with a strong opacifying performance which can withstand high temperatures.

1.4 Thesis outline

The general aim of this thesis is to improve the performance of high temperature thermal insulation by focusing on the role of the optical properties of the constituent materials in suppressing the radiative transport. The ultimate goal is to guide the development of novel high temperature high performance thermal insulation design that exhibits superior thermal and physical properties at high temperatures.

Chapter 2 presents the background information and literature review for the two thermal insulation designs considered in this work: 1) Multilayered Shielding Design and 2) Volumetric Extinction Design.

Chapter 3 covers the first research objective and is devoted to the Multilayered Shielding Design which consists of highly reflective shields placed in a low thermal conductive medium. A theoretical analysis has been done to build a model to describe the performance of multilayered insulation design. The model indicates that the reflectivity of shields is the most important factor to be considered for attenuating the incident radiation. Based on the model the performance of some representative materials is investigated to identify the most well performing materials to use as a shield. This investigation demonstrates the performance limits of the multilayered design and indicates the importance of developing a new design that presents an excellent performance to attenuate the radiation at high temperatures.

Chapter 4 is related to the second research objective and explains the performance of the second thermal insulation design, “volumetric extinction design” as an alternative approach. Volumetric design includes a large number of absorbing/scattering particles implanted into a low thermal conductive medium to suppress the radiation at high temperatures. Based on the Rayleigh theory, a numerical model is developed to predict the performance of volumetric insulation design in the viewpoint of material. The model investigates the performance of some representative materials to use as particles inside the medium. The numerical analysis is done based on:

- Reduced extinction coefficient as a function of refractive index and extinction index (absorptive index).
- Spectral extinction coefficient as a function of wavelength in the visible and the infrared spectrum region.
- Rosseland mean extinction coefficient and Planck mean extinction coefficient as a function of temperature.

The Lorentz model is also used to evaluate the main effects on the opacifying performance of materials.

Chapter 5 summarizes the important results of the work and discusses the future work that could be done on the proposed thermal insulation design in this thesis.

Chapter 2
Literature review and background

In this chapter, two high temperature thermal insulation designs are introduced. As mentioned in chapter one, the radiative heat transfer dominates over conductive and convective heat transfer modes at high temperatures. Therefore, this chapter focuses on the mechanism of radiation suppression in each design.

2.1 Multilayered shielding design

A multilayer radiation shielding thermal insulation (MLI) system comprises multiple highly reflective thin shields which are assembled parallel to each other with several layers of low thermal conductive spacers in between them (as shown in Figure 1). The aim of using reflective radiation shields is to reduce the rate of radiative heat transfer. Additionally, the spacers need to be selected from a material with a low enough thermal conductivity such that the conduction contribution remains low compared to the radiative contribution. To simplify the understanding of function of shields for attenuating the radiation, let’s consider two infinite shields that are placed parallel to each other with a non-participating medium (such as air or vacuum) in between them. The shields are assumed to be opaque such that their transmittance is negligible. In the view of radiative heat transfer, it is most convenient to picture the heat transfer in terms of a discrete number of energy bundles or rays that propagate energy through the system. If we assume that the surfaces are opaque and transmission is negligible, then when the rays hit the first surface, they will be either absorbed or reflected. If the reflectivity of the shield is for example 0.5, then 50% of the rays will be reflected and 50% of them will be absorbed. If the ray is absorbed, it means that the shield will be thermalized and then the absorbed ray will be re-emitted in the condition of radiative equilibrium. The emission direction might be forward or backward. If we assume that the shield is isothermal and has the same emissivity in both sides, then 50% of the rays will be emitted forward and 50% of them will be emitted backward. Therefore, it can be concluded that after a single interaction with the first shield 25% of rays can reach the second shield by assuming that the first shield has 50% reflectivity. Now if we assume that the shield has a higher reflectivity around 90%, then only 5% of the incident rays reach the second shield. And by embedding multiple highly reflective shields inside the insulation medium, the chance for the incident rays to penetrate through the medium is very low which demonstrates the excellent function of multilayered shielding design to attenuate the radiation.

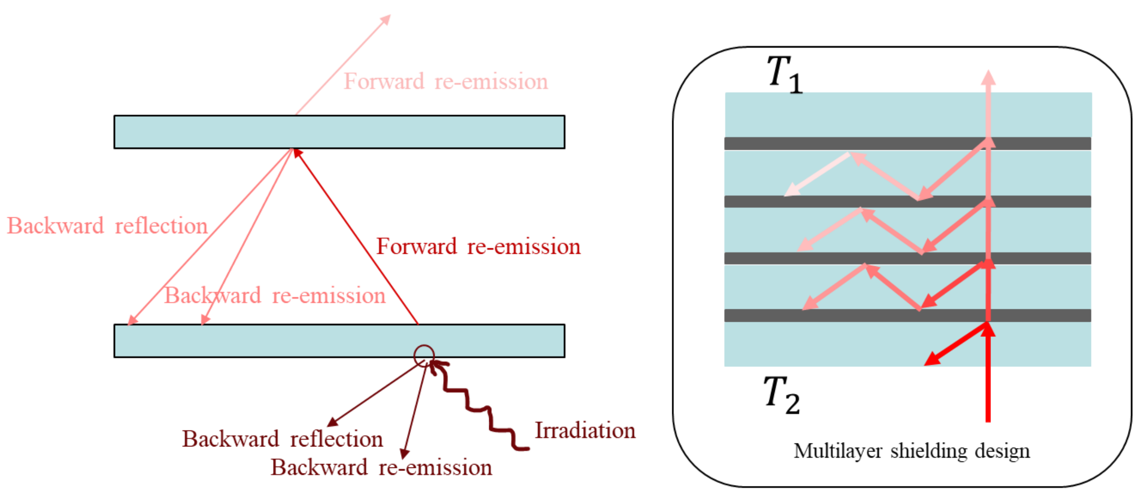

Figure 2.1. Multilayer insulation design and its function to attenuate an incident ray.

As explained, the reflectivity of shields is the most important parameter to consider in order to reach the highest insulating performance and it will be explained in detail in chapter 3. The idea of using reflective shields into the insulation medium was developed in 1950s [30] and since then it has been attracted the interest of many researchers in a wide range of fields from low temperatures (cryogenic process engineering) [31][32][33] to high temperatures such as high temperature thermal energy storage and space fields [34][35]. Numerous experimental and numerical studies have been done to investigate the performance of MLI systems and to enhance their performance by optimizing some parameters such as layer density and number, and the spacer material and structure.

Since the temperature is a highly influential parameter in the performance of MLI systems, it is attempted to review the progress in MLI systems in two sections of low temperature (for cryogenic applications) and high temperature applications.

2.1.1 Low temperature MLI

Vacuum multilayer insulation systems are one of the most effective insulation elements used in cryogenic applications. The cryogenic temperature range is normally from 77 [K] to absolute zero [36], therefore, which is much lower than the high temperature applications which are the scope of the thesis. However, even though radiation is low at cryogenic temperatures, it dominates over conduction/convection due to the vacuum environment. In the field of space cryogenic, radiative heat transfer becomes important since vacuum condition exists. Therefore, MLIs are a good option for such low temperature applications to insulate the systems from radiation heat load [37]. In an ideal MLI design, the insulation consists multiple separated floating shields in a high vacuum environment. Low-conductive spacers are needed to place between the shields so that they do not touch each other. Accordingly, there are commonly still gas molecules in the spacers so that gas and solid conductions need to be considered together with radiation even at vacuum conditions [37]. In the low temperature MLI systems, some techniques such as netting spacers or embossed spacers have been used to lower the contact area between spacers and the shields to decrease the conductive heat transfer. In a study done by M. Takeshi et al. [31], a novel Non-Interlayer-Contact-Spacer MLI (NICS-MLI) has been introduced in order to minimize the conductive heat transfer. In this design, they use separated spacer segments made of polyethereketone that are attached in a special way in which the contact area can be considered negligible. As figure 2 shows, instead of using a conventional method of fastening films in which the spacers and shields are attached by stitching, they use the separated spacers, and the spacers are pined vertically to each other by placing the shields between them. In their design, six reflective shields were attached by four vertical beams of spacers and the temperature of the outer and inner surfaces were 300 and 77 $[K]$. A rectangular boil-off calorimeter was used to evaluate the thermal performance of the new NICS-MLI. Experimental results revealed that the heat loss of NICS-MLI was much smaller than a conventional multilayered insulation and the effective thermal conductivity of NICS-MLI reduced to 3.85×10^{-4} [W m^{-1} K^{-1}].

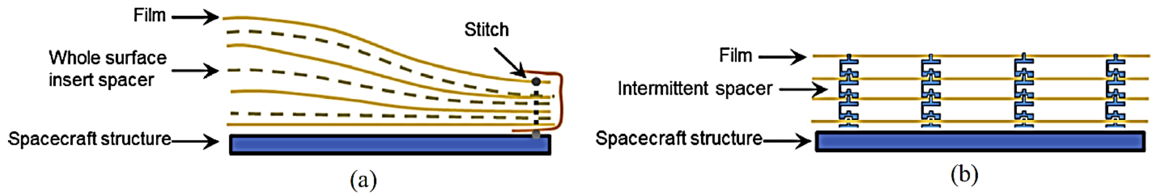

Figure 2.2. Structure of a conventional MLI (a) and the novel NICS-MLI (b) [31].

In a theoretical and experimental study, B. Wang et al. [32] investigated the influence of layer density, spacer material and thickness on the performance of a Variable Density Multilayer Insulation (VDMLI) in a temperature range of $77 - 353\ [K]$. Considering that increasing the temperature results in increasing the thermal conductivity, they divided the MLI medium into three parts in the thickness direction. Part 1 was exposed to a low temperature while part 3 was adjacent to the high temperature environment. Their numerical results indicated that the number of shields at the part that was close to a high temperature needed to be higher compared to the part that was adjacent to the cold temperature. In their analysis, the optimum configuration was when the number of spacer layers between every two shields was six in part 1 (with 4 shields), and then it lowered gradually in part 2, reaching to two and maintained at this number in the part 3 (as shown in figure 3).

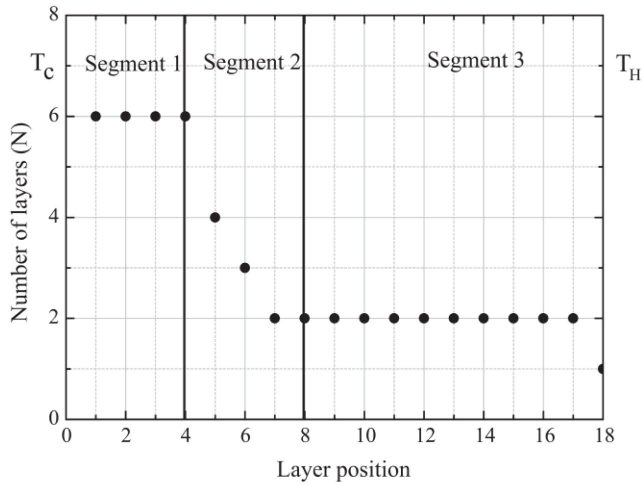

Figure 2.3. Distribution of layer density in the optimized structure [32].

They showed that using the optimized configuration (using Dacron net as spacer and layer density of $6.35, 12.7, 19.05$ [layers/cm] for part 1, 2, 3, respectively) lowered the effective thermal conductivity from 6.75×10^{-5}[W m^{-1} K^{-1}] to 3.6×10^{-5}[W m^{-1}K^{-1}] compared to a conventional case using non-woven fiber cloth as spacer with the uniform layer density (12.7 [layers/cm] in the all parts). Moreover, the heat flux reduced from 1.1 to 0.3 [W m^{-2}] in the optimum case. They found that using Dacron net as spacer instead of non-woven fiber cloth lowered the effective heat transfer by 54% under the same layer density distribution. Their results also revealed that layer density of 26 [layers/cm] resulted in the lowest heat transfer coefficient in all cases of uniform configurations. This has an agreement with the results of investigation done by B. Deng et al. [33] in which they evaluated the influence of layers' number and density and materials of shields and spacers on the thermal performance of the insulation in the temperature range of $77 - 293$ [K]. Their theoretical and experimental results indicated that layer density of 25 [layers/cm] led to the minimum effective thermal conductivity for 30-80 number of layer (as shown in figure 4). Furthermore, 50 was the optimum number for all layer densities. In the view of spacer and shields materials, they studied the performance of four different cases with two different spacers and shields which is shown in Table 2.1. As it can be seen, using Double-aluminized Mylar as shield and Fiberglass paper as spacer decreases the heat flux and thermal conductivity to 1.43 [W m^{-2}] and 0.135×10^{-3} [W m^{-1} K^{-1}], respectively.

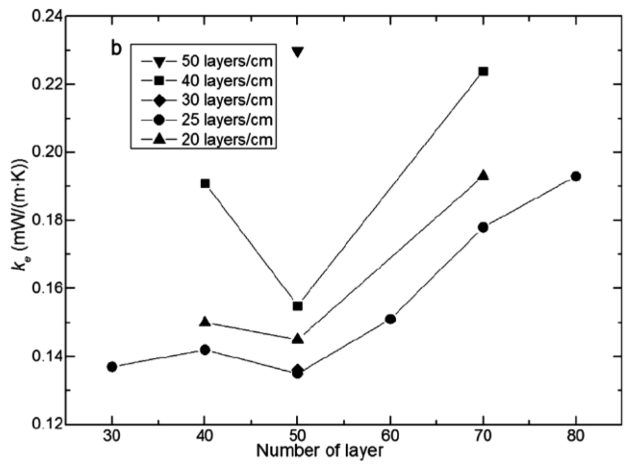

Figure 2.4. Experimental effective thermal conductivity vs. number of layers for different layer densities [33].

Table 2.1. Experimental effective thermal conductivity and heat flux for four different cases [33].

Shield	Spacer	q [W m^{-2}]	K_e [mW m^{-1} K^{-1}]
Double-aluminized Mylar	Fiberglass paper	1.43 ± 0.06	0.135 ± 0.006
Double-aluminized Mylar	Dacron net	2.15 ± 0.09	0.205 ± 0.009
Aluminum foil	Fiberglass paper	4.55 ± 0.19	0.430 ± 0.018
Aluminum foil	Dacron net	4.49 ± 0.19	0.425 ± 0.018

2.1.2 High temperature MLI

In the previous section, the significant role of shields, as well as the spacer's material and structure in the evacuated low temperature applications were shown. At high temperatures (beyond $300\,[^\circ\mathrm{C}]$), radiation dominates which highlights the importance of shield performance. A wide range of studies have been carried out to investigate and improve the performance of high temperature MLI. Considering high temperatures, some materials such as fibrous, microporous and refractory materials can be used as high temperature-low conductive spacers. In terms of thermal shields, the literature studies show that the emissivity of shields have a great influence on the effective thermal conductivity. In the field of hypersonic vehicles, T. Ji et al. [34] developed a two-dimensional model to predict the total heat transfer rate in the MLI systems at high temperatures. In their work, ceramic screens coated with gold were used as reflective shields (with thickness of 0.1 [mm]) inside a fibrous medium. By keeping the thickness of MLI design as 20 [mm], they investigated the influence of $N = 10$, 18, and 34 number of insulation layers ($\text{number of shields} = N - 1$) on the temperature of the cold side. Figure 2.5 demonstrates the effect of number of shields on the temperature of the cold side (bottom surface) which indicates that increasing the number of layers wouldn't necessarily result in a better performance and there is an optimum number (18 layers in this investigation). The fact is that the thickness of the shields is considerable in their investigation and the shields are made of materials with higher thermal conductivity than the spacer and as their number increases the contribution of conductive heat transfer becomes important. They also found that the layout of shields wouldn't affect considerably the system's thermal performance.

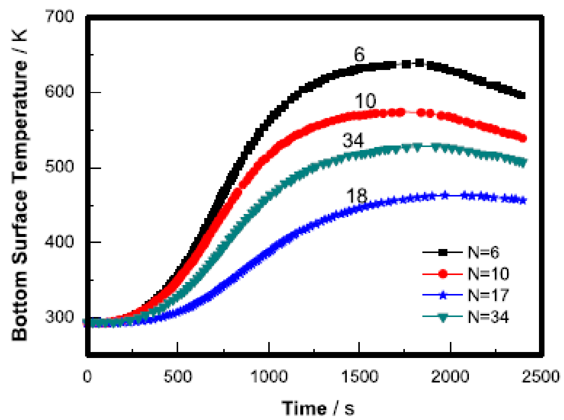

Figure 2.5. Cold side temperature vs. time for various insulation layers [34].

Due to the study done by M. Spinnler et al. [35], a numerical model of combined conductive and radiative heat transfer within a medium separated by shields was developed to study the thermal performance of the system at around 1000 [℃]. In their investigation, they considered two spacers of fibrous and micro-porous materials and two shields of low reflective stainless steel ($\varepsilon_{\text{eff}} = 0.6$) and high reflective gold ($\varepsilon_{\text{eff}} = 0.05$). Their theoretical model was based on the energy conservation method so that the MLI medium was divided into k number of sections and in every section there were multi-isothermal-optically thin-spacer layers (N-number of spacers) placed between two adjacent shields (shown in figure 6).

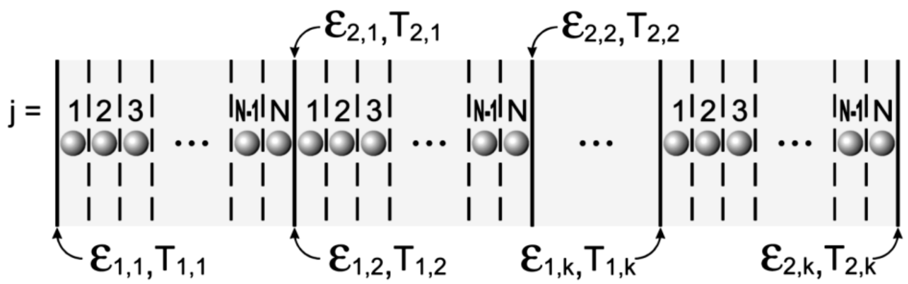

Figure 2.6. The structure of the insulation design with k sections including N layers [35].

Figure 7. (a) demonstrates their theoretical and experimental result of the ceramic-fiber spacer (Saffil) with and without gold and stainless steel shields, while figure 7. (b) shows the results for the micro-porous spacer under the condition of 30 [mm] spacer, four number of shields placing with the same distance (the first shield was 5 [mm] away from the hot side). Figure 7. (a) shows that the results of experiments had a good agreement with the theoretical values. Based on figure 7. (a), embedding four golden shields inside the fibrous insulation could lower the effective thermal conductivity significantly at high temperatures, while at low temperatures it had a minor effect. This demonstrates that reflective shields perform effectively at high temperatures at which the radiation dominates the heat transfer rate. The results for micro-porous insulation (figure 7. (b)) reveal some important differences. As can be seen, the results of theory didn't show a good correspondence with that of experiments which indicates that their model couldn't predict the behaviour of reflective shields inside a highly absorbing spacer. Based on their report, the mean extinction coefficient β $(T = 700$ [°C]) of ceramic-fiber and micro-porous material was 5097 and $32{,}044$ [m^{-1}], respectively. Comparing figures 7. (a) and (b), it

can be interpreted that the influence of shields lowers substantially with enhancing opacity of the insulation medium. They also reported that in the cold side, radiation had a low allocation of the total heat flux (5%) for the highly absorber spacer while this value was 15% for the ceramic-fiber spacer. This shows that at high temperatures, optically thick micro-porous spacers are more effective to suppress the radiation than the optically thin fibrous spacers even including the highly reflective shields.

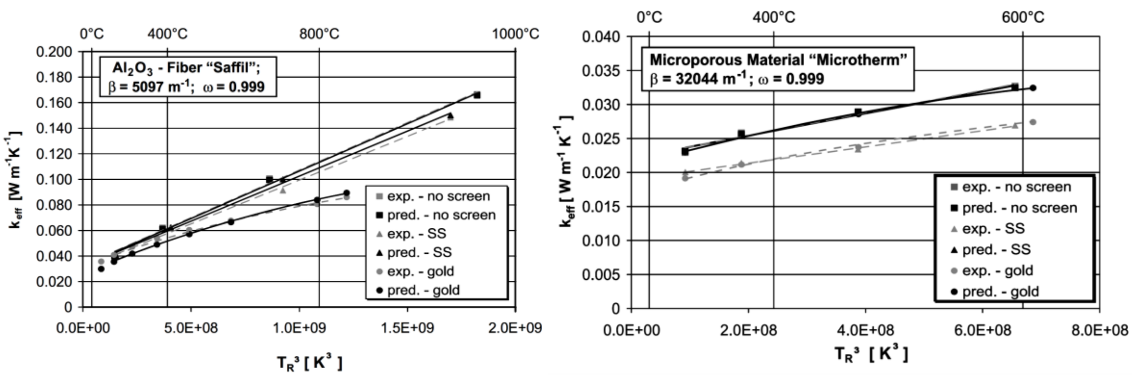

Figure 2.7. Effective thermal conductivity vs. temperature (dashed line: experimental value, solid line: numerical value). a) Ceramic-fiber spacer; b) Microporous spacer [35].

So far, the function of multilayered insulation design to attenuate the radiation was explained and an overview of previous studies on this design was given. As concluded, the main point about MLI design is the emissivity (or reflectivity) of the shields (which will be discussed in details in chapter 3). Chapter 3 will theoretically explain that metals are the most optimum materials with having the highest reflectivity to use as shields inside the MLI and will show the limitations of using metals at ultra-high temperatures which affects the performance of the MLI system over time. Accordingly, this work considers another thermal insulation design, named volumetric insulation design, as an alternative option.

2.2 Volumetric extinction design

The alterative design considered in the present work is the volumetric extinction design which utilizes radiatively participating (absorbing/scattering) media dispersed throughout the volume of the insulation medium. Figure 8 shows the volumetric design adopted in this work which includes a large number of very small particles inside the insulation which act as radiant barrier to supress the radiation inside the insulation medium. The function of particles is so that when an electromagnetic wave hits particles inside the medium, a part of it will be propagated trough the medium by scattering and another part will be absorbed by particles and then re-emitted isotropically. Eventually, the radiation will be spread out throughout the insulation and its intensity will be gradually reduced after interacting with a large number of particles. The higher absorbing/scattering ability that particles have, the higher radiation attenuation occurs.

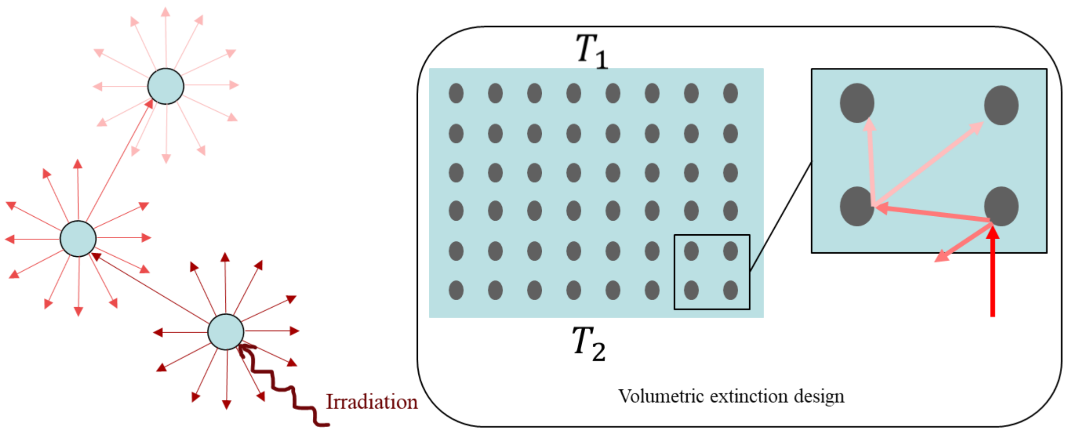

Figure 2.8. Volumetric extinction design and its function to attenuate an incident ray.

Many insulation structures such as aerogels exhibit a good thermal performance at low temperatures where thermal conductivities below 0.1 [W $m^{-1}K^{-1}$] are routinely achieved. However, their (effective) thermal conductivity increases significantly with increasing temperature, as the radiation becomes dominant over the conduction and a method is needed to supress the radiation. Embedding opacifier particles inside the insulation medium is an effective method to enhance the thermal performance of insulation at high temperatures by increasing the effective extinction coefficient. Y. Lei et al. [38] embedded nano-filler graphene oxide into the silica aerogel bed to reach a lower thermal conductivity. Their results showed that thermal conductivity of the composite silica/graphene oxide aerogel reduced from 23% compared to a regular silica aerogel. They also found that the new composite aerogels had a higher mechanical strength. Due a study done by J. Feng [39], infrared opacifiers were added to the fumed silica to maintain the thermal conductivity low at high temperatures. They investigated the effect of adding four different types of opacifiers (SiC, BN, $ZrSiO_4$, KT_6) compared to the pure fumed silica. Their results showed that the mass specific extinction coefficient increased significantly, as can be seen in figure 9. SiC was the optimum material in a wide range of wavelength among the investigated materials. They also showed that composite of SiC/fumed silica with the mass ratio of 25% SiC with the particle size of 3.029 [μm] had the highest specific extinction coefficient among the other numbers of mass ratio and particles sizes.

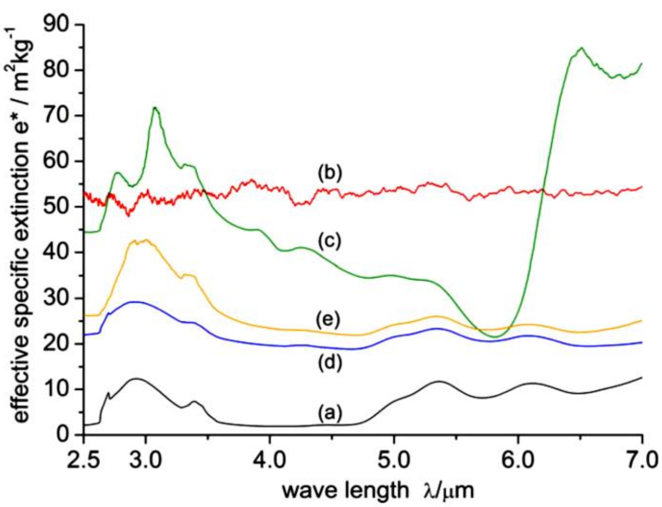

Figure 2.9. Effective extinction coefficient as a function of temperature for fumed silica comprising opacifiers with 20 wt%; a) pure fumed silica, b) SiC, c) BN, d) $ZrSiO_4$, e) KT_6 [39].

X. Wang et al. [40] built a model to investigate the effect of various types of opacifiers (carbon black, coal ash, SiC, TiO_2, Al_2O_3, and ZrO_2) with different particle sizes ($2 - 8$ [μm]) on the radiative performance of silica aerogel/opacifier composite. Their results revealed that the performance of opacifier depended significantly on the temperature. Figure 2.10 shows the Rosseland mean extinction coefficient as a function of temperature. As shown, carbon had the highest extinction ability over the whole temperature range.

However, the carbon black structure changes with increased temperature which makes it unsuitable to use at high temperatures. SiC and coal ash were, therefore, found to be the optimum opacifiers at high temperatures. Their investigation also indicated that there was an optimum diameter at various temperatures as shown in Figure 11. It can be seen that the radiative thermal conductivity of the un-opacified silica aerogel is 0.0024 [$\mathrm{Wm^{-1}K^{-1}}$] at 300 [K] and increases significantly with increasing the temperature, reaching 0.62 [$\mathrm{Wm^{-1}K^{-1}}$] at 1300 [K]. While, opacifing the aerogel with SiC decreases the radiative thermal conductivity substantially, especially at high temperatures. Loading SiC with diameters of 4, $3, 5, 6, 8$, and 2 [μm] lowers the thermal conductivity to 0.0584, 0.0605, 0.0635, 0.0734, 0.0927 and 0.0945 [$\mathrm{Wm^{-1}K^{-1}}$], respectively at 1300 [K].

Based on the fact that there is a temperature gradient inside the medium in the thickness direction, they suggested that developing a multi-section design with either different opacifier types or one opacifier with various particle sizes would be optimum. Therefore, they embedded SiC with different particles sizes of 4, 5, and 6 [μm] inside the silica aerogel as shown in figure 12. Their simulation-based result showed that the radiative thermal conductivity of the new design lowered 11% compared to the optimum uniform design.

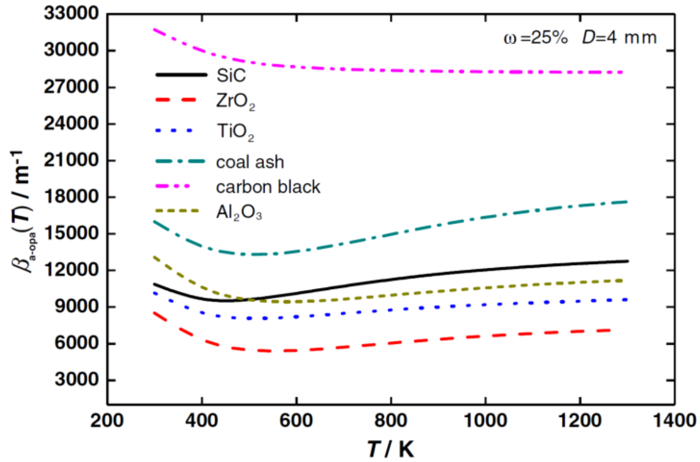

Figure 2.10. Rosseland mean extinction coefficient as a function of temperature for various silica aerogel/opacifier composite [40].

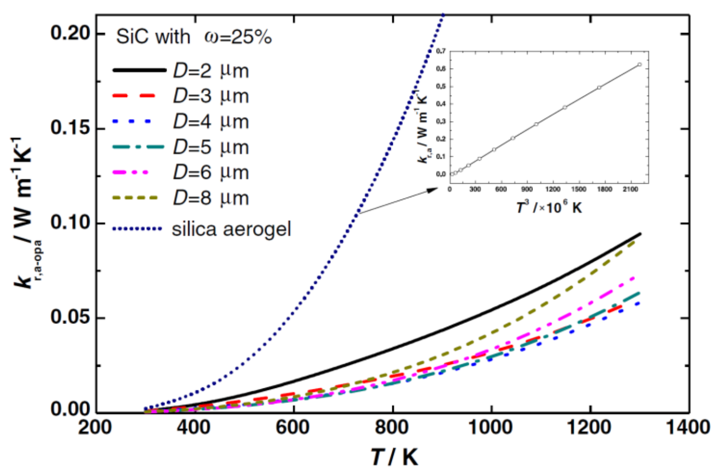

Figure 2.11. The temperature dependency of radiative thermal conductivity for un-opacified and SiC-opacified silica aerogels with various SiC diameters [40].

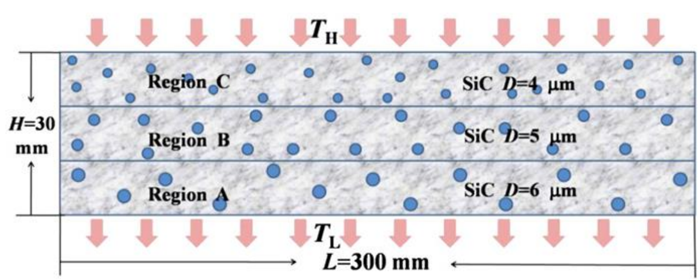

Figure 2.12. SiC particle size distribution in the thickness direction [40].

A similar work was carried out by J. Zhao et al. [41]. Mie theory was used to investigate the influence of opacifier material, particle diameter, and physical form on the Rosseland mean extinction coefficient at high temperatures. Based on the results of their model, carbon black was the optimal material for the temperature below 600 [K], while for higher temperatures, SiC showed a better performance as a radiant barrier (shown in figure 13. (a)). In the view of particle size, they investigated the performance of SiC with different particle diameters over the temperature range of $300 - 900$ [K]. Figure 13. (b) shows that particle diameter of 4 [μm] is the optimum value for temperature lower than 400 [K], while for higher temperature, diameter of 3 [μm] is the optimum number to reach the highest Rosseland extinction coefficient. Regarding the opacifier shape, oblate spheroid showed the maximum ability to extinct the radiation compered to the spherical, cylindrical and cubic shapes.

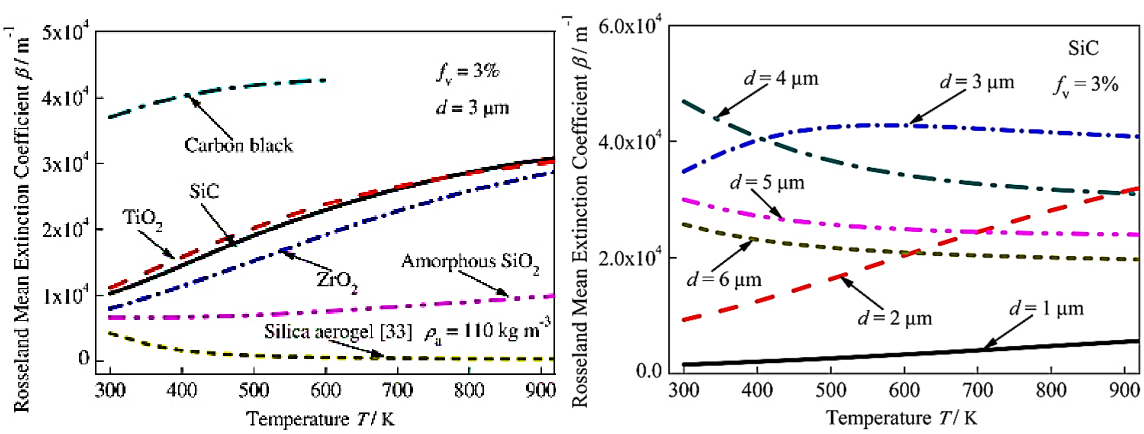

Figure 2.13. Rosseland mean extinction coefficient as a function of temperature; a) various opacifier particles loaded in silica aerogel, b) silica aerogel/SiC composite with various SiC particle sizes [41].

An overview of previous studies indicates that MLI design works well in cryogenic applications and especially when a vacuum environment presents [36][86][87]. Even though MLI designs have an excellent thermal conductivity (mostly lower than 0.1 $[\mathrm{W\,m^{-1}\,K^{-1}}]$) they have maximum operational temperature of 1000 [℃] since they normally consist of metal shields [35][25]. On the other hand, opacified thermal insulation takes advantage of opacifying particles to suppress radiation. A comparison between a MLI design and an opacified microporous material showed that enhancing the opacity of insulation medium is more effective than shielding it to suppress radiation [35]. Another important point regarding the previous studies is that even though numerous studies have been done to enhance the performance of MLI design or volumetric approach by trying different materials, there is not a universal methodology by which every material can be evaluated. Hens, this work presents a novel methodology for each design which is useful to have a comprehensive comparison and evaluation for any types of material.

Chapter 3
Multilayer insulation design

Chapter 3 is devoted to the multilayered shielding design and presents a theoretical analysis to describe the performance of multilayered insulation design. As mentioned in chapter 2, a multilayer thermal insulation includes multiple layers of radiation shields separated by spacers. Since this thesis focuses on high temperature conditions, the performance of shields to block the radiation propagation inside the insulation medium is considered. The complex index of refraction of different materials has been used to determine their performance to suppress the radiation in order to identify the optimal materials with the highest performance.

3.1 Minimizing the radiative heat transfer in MLI systems

To describe the radiative heat transfer phenomenon through the system, we consider a radiation shield placed between two large parallel plates of emissivities ε_1 and ε_2 maintained at uniform temperatures of T_1 and T_2, respectively. $\varepsilon_{3,1}$ and $\varepsilon_{3,2}$ are the emissivities of the radiation shield facing plates (1) and (2), respectively. Thermal resistance networks are a useful way to describe the resistance of systems to the flow of heat which depends on the geometry and the thermal properties of the systems. The thermal resistance circuit of the mentioned geometry is shown in figure 3.1.

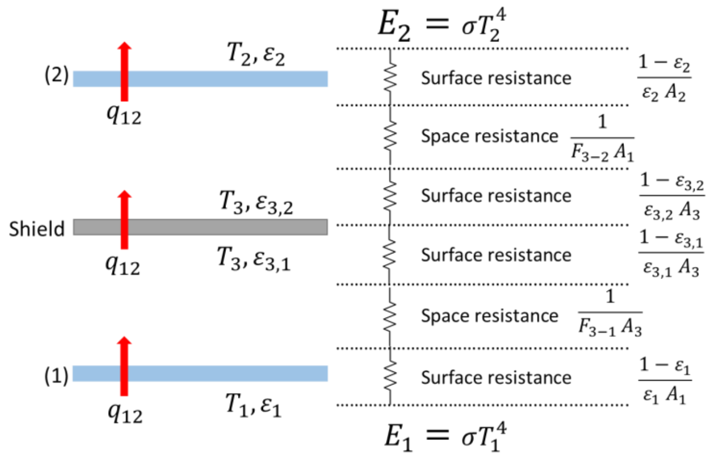

Figure 3.1. Thermal resistance network of a radiation shield placed between two plates.

Considering that all surfaces are gray (their optical properties are independent of wavelength) and diffuse (their optical properties are independent of direction), the one-dimensional radiative heat flow through the geometry can be defined as:

$$Q_{12} = \frac{E_1 - E_2}{R_1 + R_{1-3} + R_{3,1} + R_{3,2} + R_{3-2} + R_2}$$
$$= \frac{\sigma(T_1^4 - T_2^4)}{\frac{1-\varepsilon_1}{\varepsilon_1\, A_1} + \frac{1}{F_{3-1}\, A_3} + \frac{1-\varepsilon_{3,1}}{\varepsilon_{3,1}\, A_3} + \frac{1-\varepsilon_{3,2}}{\varepsilon_{3,2}\, A_3} + \frac{1}{F_{3-2}\, A_1} + \frac{1-\varepsilon_2}{\varepsilon_2\, A_2}} \tag{3.1}$$

Where E_1 $(= \sigma T_1^4)$ and E_2 $(= \sigma T_2^4)$ are the potentials at nodes 1 and 2, A_1, A_2, A_3 are the areas of surface 1, 2, and 3, and F_{3-1} and F_{3-2} are the view factors form surface 3 to surface 1 and 2, respectively. The view factor from surface *i* to surface j (F_{i-j}) is explained as the fraction of diffuse energy leaving surface *i* and directly reaches surface *j*.

The second part of the Equation 3.1 applies only for gray diffuse plates and an important question that might appear here is that how strict is the gray and diffuse assumption? In fact, if the plates are infinitely wide and one-dimensional heat flow is considered, the same result applies for the specular surfaces or even for any directional dependence of reflectance. Regarding the wavelength dependency, where the gray assumption comes in here is that the emissivity of plates has a single value and are not a function of wavelength. For non-gray surfaces, the procedure is that the emissivity used in the Equation 3.1 must be spectrally averaged. The Planck distribution can be used to obtain the total emissivity which is spectrally averaged over the whole wavelength (the procedure of using Planck distribution to reach a total value will be explained in Chapter 4). The Planck distribution is a function of temperature; therefore, the temperature of the surface is needed to calculate the total emissivity of that surface. On the other hand, the temperature distribution is not specified until the Equation 3.1 is solved. Accordingly, the temperature of surfaces can be defined iteratively. One suggestion is that the temperature distribution can be guessed (it could be for example linear), the total emissivity can be then evaluated based on the temperature assumption. Then the heat flow will be defined. Based on the heat flow and the thermal resistance circuit, the temperature of each surface will be specified and can be used as a new guess. This procedure will be continued iteratively until the values converge. If we assume that $F_{31} = F_{23} = 1$ and $A_1 = A_2 = A_3 = A$, then equation 3.1 simplifies to:

$$Q_{12} = \frac{A\sigma(T_1^4 - T_2^4)}{(\frac{1}{\varepsilon_1} + \frac{1}{\varepsilon_2} - 1) + (\frac{1}{\varepsilon_{3,1}} + \frac{1}{\varepsilon_{3,2}} - 1)} \tag{3.2}$$

Equation 3.2 is valid when we have one shield between two parallel plates. If we consider that two parallel plates are separated by N_S number of radiation shields, the radiative power becomes:

$$Q_{12} = \frac{A\sigma(T_1^4 - T_2^4)}{\left(\frac{1}{\varepsilon_1} + \frac{1}{\varepsilon_2} - 1\right) + \left(\frac{1}{\varepsilon_{3,1}} + \frac{1}{\varepsilon_{3,2}} - 1\right) + \cdots + \left(\frac{1}{\varepsilon_{N_\mathrm{S}+2,1}} + \frac{1}{\varepsilon_{N_\mathrm{S}+2,2}} - 1\right)} \qquad (3.3)$$

When we assume that the emissivities of the radiation shields are all equal (ε) , but the emissivity of top and bottom plates are different from the shields, equation 3.3 reduces to:

$$Q_{12} = \frac{A\sigma(T_1^4 - T_2^4)}{\left(\frac{1}{\varepsilon_1} + \frac{1}{\varepsilon_2} - 1\right) + N_\mathrm{S} * \left(\frac{2}{\varepsilon} - 1\right)} \qquad (3.4)$$

Then if we assume that all emissivities are equal, the radiative power becomes:

$$Q_{12} = \frac{A\sigma(T_1^4 - T_2^4)}{(N_\mathrm{S} + 1) * (\frac{2}{\varepsilon} - 1)} \qquad (3.5)$$

According to the radiative heat exchange between two surfaces ($Q_{\mathrm{rad}} = \varepsilon_{\mathrm{eff}}\sigma A(T_1^4 - T_2^4)$), we can specify:

$$\varepsilon_{\mathrm{eff}} = \frac{1}{(N_\mathrm{S} + 1) * (\frac{2}{\varepsilon} - 1)} \qquad (3.6)$$

Where $\varepsilon_{\mathrm{eff}}$ is the effective emissivity of the system. Additionally, if we assume that the top and the bottom surfaces are blackbodies, equation 3.3 reduces to:

$$\varepsilon_{\mathrm{eff}} = \frac{1}{N_S\left(\frac{2}{\varepsilon} - 1\right) + 1} \quad (3.7)$$

In chapter 1, it was indicated that $\varepsilon_{\mathrm{eff}}$ must be decreased to minimize the heat loss. Equation 3.7 shows that increasing the number of radiative shields or decreasing their emissivity would decrease the effective emissivity of the system.

The radiative shields are assumed to be opaque so that the transmission is negligible. Therefore, the relationship between the absorptivity (α) of the shields and their reflectivity (ρ) can be expressed as:

$$\alpha = 1 - \rho \quad (3.8)$$

Due to Kirchhoff's law, the relationship between the emissivity and absorptivity of any gray diffuse surface is:

$$\alpha\ (T) = \varepsilon\ (T) \quad (3.9)$$

Considering equations 3.8 and 3.9, we can express:

$$\varepsilon = 1 - \rho \quad (3.10)$$

Equation 3.10 shows that emissivity lowers with an increase in reflectivity. Considering equations 3.7 and 3.10, it can be concluded that radiative shields having the highest reflectivity would result in the lowest radiative heat transfer. The complex index of refraction as a fundamental material property which governs the interaction with electromagnetic waves can be used to investigate the performance of materials to reflect the incident radiation. To come up with the high performance materials with having a high reflection, it is important to investigate the connection between the reflection and the complex index of refraction.

3.2 Reflectivity investigation

When an electromagnetic wave encounters the interface between two media, both reflection and refraction may happen as shown in figure 3.2. θ_i and θ_r are the incidence angle and reflected angle, while χ is the angle of refraction.

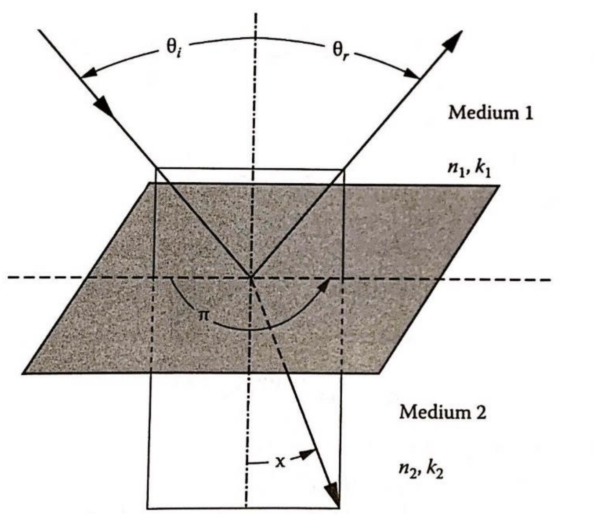

Figure 3.2. Interaction of the electromagnetic wave at an interface between two media [10].

Now we assume that medium 1 is the main medium and medium 2 is the radiative shield (surface). We start with an optically smooth surface as a simplest case and don’t consider the effect of roughness. Therefore, the surface is specular, and the reflective angle is equal to the incident angel. In order to investigate the reflection of the electromagnetic wave at the interface of the medium and the surface, the complex index of refraction for both of them is required to be specified (equation 3.11).

$$\bar{n}_\lambda = n_\lambda - ik_\lambda \tag{3.11}$$

n_λ and k_λ are the real and imaginary parts of the refractive index which are denoted as the refractive index and absorptive index, respectively. The subscript λ stands for the wavelength which shows that the refractive index and the absorptive index are spectral parameters and depend on the wavelength.

For unpolarized incident radiation, the specular reflectivity of a ray on a surface at angle θ_i can be taken as an average of the parallel-polarized reflectivity and the perpendicular-polarized reflectivity, which can be determined as [10]:

$$\rho_{\lambda,\parallel}(\theta_i) = [\frac{\tan(\theta_i - \chi)}{\tan(\theta_i + \chi)}]^2 \tag{3.12}$$

$$\rho_{\lambda,\perp}(\theta_i) = [\frac{\sin(\theta_i - \chi)}{\sin(\theta_i + \chi)}]^2 \tag{3.13}$$

$$\rho_\lambda(\theta_i) = \frac{\rho_\parallel(\theta_i) + \rho_\perp(\theta_i)}{2} \tag{3.14}$$

These are known as Fresnel's relations [42]. The relationship between the reflected angle and the refraction angle can be described by the Snell's law as:

$$\frac{sin\chi}{sin\theta_i} = \frac{\bar{n}_1}{\bar{n}_2} = \frac{n_1 - ik_1}{n_2 - ik_2} \tag{3.15}$$

Subscript 1 is with respect to the medium, while subscript 2 refers to the surface. $\sin\chi$ is complex since the relation described in equation 3.15 is complex.

Considering equations 3.12-3.15, the reflectivity for the normal incidence in which the angle of incident beam is zero ($\theta_i = 0$) can be expressed as [10]:

$$\rho_{\lambda,\mathrm{n}} = \frac{(n_2 - n_1)^2 + (k_2 - k_1)^2}{(n_2 + n_1)^2 + (k_2 + k_1)^2} \tag{3.16}$$

If we consider that rays pass through a medium which is air or vacuum ($n_1 = 1$ and $k_1 = 0$) and coincide with a material with $\bar{n} = n - ik$, equation 3.16, then, reduces to:

$$\rho_{\lambda,\mathrm{n}} = \frac{(n-1)^2 + k^2}{(n+1)^2 + k^2} \tag{3.17}$$

ρ_n expresses the connection between the normal reflectivity of the incident rays and the optical properties of the surface. Providing a surface plot is helpful to describe the relationship between the two independent parameters of n and k and the designated dependent parameter of $\rho_{\lambda,\mathrm{n}}$. Figure 3.3 demonstrates the surface plot of normal reflectivity as a function of n and k and shows at what range of n and k, normal reflectivity is high or vice versa.

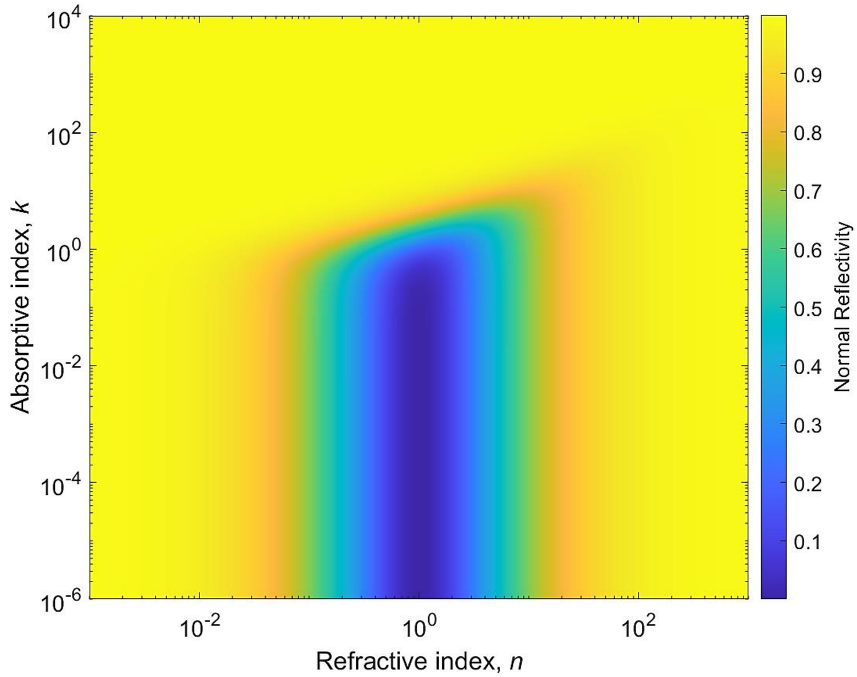

Figure 3.3. Normal reflectivity as a function of n and k.

Until now, only the beam with the angle of zero has been considered and normal reflectivity was discussed. To be more general, the directionality of the incident radiation needs to be taken into account. By considering the polar angle of the incident rays into air or a vacuum, the alternative forms of Fresnel's relations for the parallel reflectivity and the perpendicular reflectivity can be predicted as [42]:

$$\rho_{\lambda,\parallel}(\theta_i) = \frac{(p - \sin\theta_i \, \tan\theta_i)^2 + q^2}{(p + \sin\theta_i \, \tan\theta_i)^2 + q^2}\rho_{\lambda,\perp}(\theta_i) \tag{3.18}$$

$$\rho_{\lambda,\perp}(\theta_i) = \frac{(\cos\theta_i - p)^2 + q^2}{(\cos\theta_i + p)^2 + q^2} \tag{3.19}$$

where

$$p^2 = \frac{1}{2}[\sqrt{(n^2 - k^2 - \sin^2\theta_i)^2 + 4n^2k^2} + (n^2 - k^2 - \sin^2\theta_i)] \tag{3.20}$$

$$q^2 = \frac{1}{2}[\sqrt{(n^2 - k^2 - \sin^2\theta_i)^2 + 4n^2k^2} - (n^2 - k^2 - \sin^2\theta_i)] \tag{3.21}$$

Then, in order to obtain the spectral hemispherical reflectivity, the directional reflectivity can be integrated over the hemisphere [43] as:

$$\rho_\lambda = \int_0^1 \rho(\theta_i)\, d(\sin^2\theta_i) = \int_0^1 \frac{\rho_\parallel(\theta_i) + \rho_\perp(\theta_i)}{2}\, d(\sin^2\theta_i) \tag{3.22}$$

Equation 3.22 expresses the spectral hemispherical reflectivity which is in fact a function of refractive index and absorptive index of shields. Figure 3.4 depicts the surface plot of hemispherical reflectivity as a function of k and n which is a universal performance plot for MLI design and allows us to understand at what range of k and n we have the maximum reflectivity. As it can be seen in this figure, the graph of the hemispherical reflectivity is relatively similar to that of the normal reflectivity, but more comprehensive, since the hemispherical reflectivity includes all incident waves with all angles.

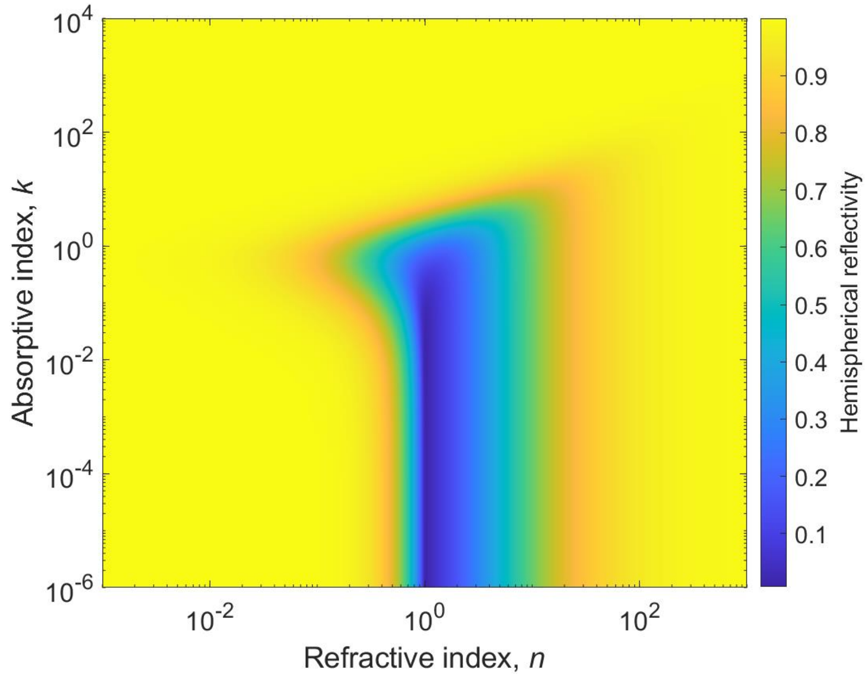

Figure 3.4. Hemispherical reflectivity as a function of n and k.

In section 3.1 it was revealed that the higher the reflectivity the radiation shields are, the lower radiative losses through the insulation system. Accordingly, the main aim is to come identify materials with having the highest reflectivity to use as reflective shields inside the insulation medium. For this purpose, the hemispherical reflectivity plot has been used as a performance plot for MLI design to evaluate the performance of different materials. For various representative materials, a curve of k as a function of n has been plotted and merged with the hemispherical reflectivity map to see where each curve lies in the hemispherical reflectivity plot. The materials that lie within the maximum reflection region (yellow region in the map) are then identified as the well performing materials. The result of investigation of different materials has been shown in figure 3.5. The references of investigated materials are listed in Table 4.1 in Chapter 4.

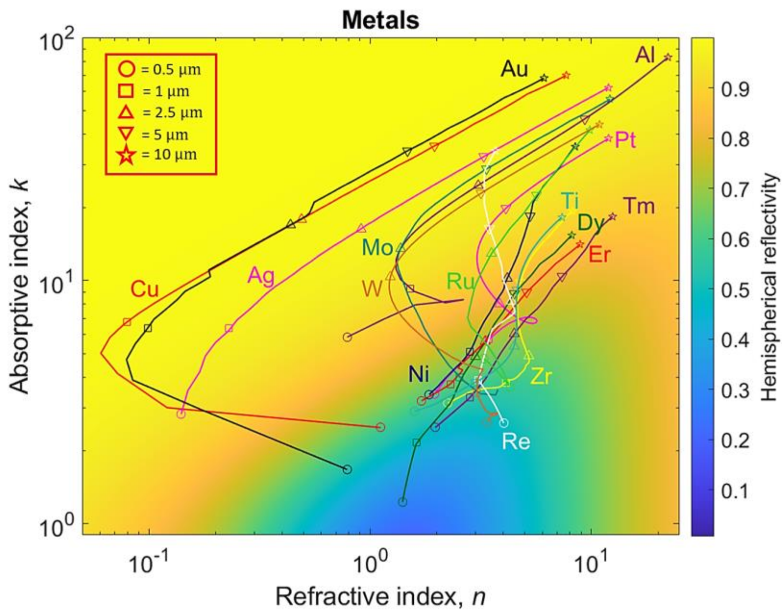

a

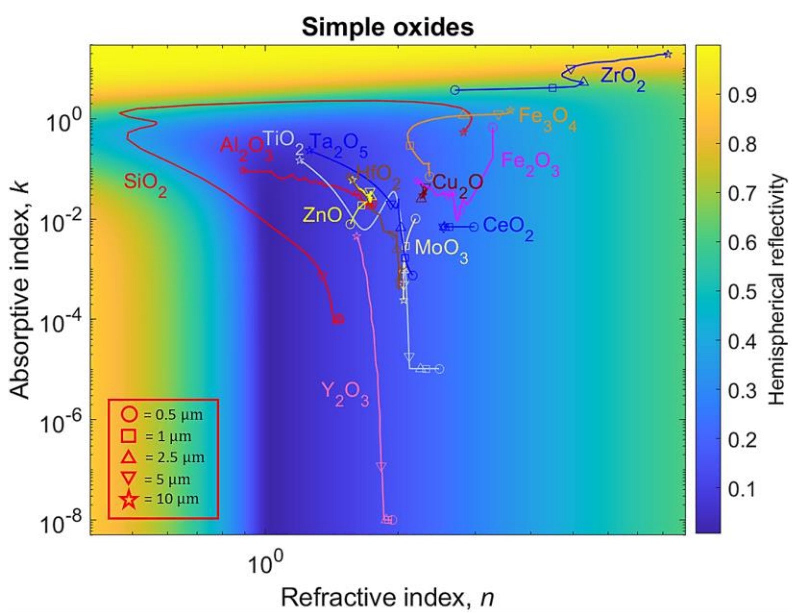

b

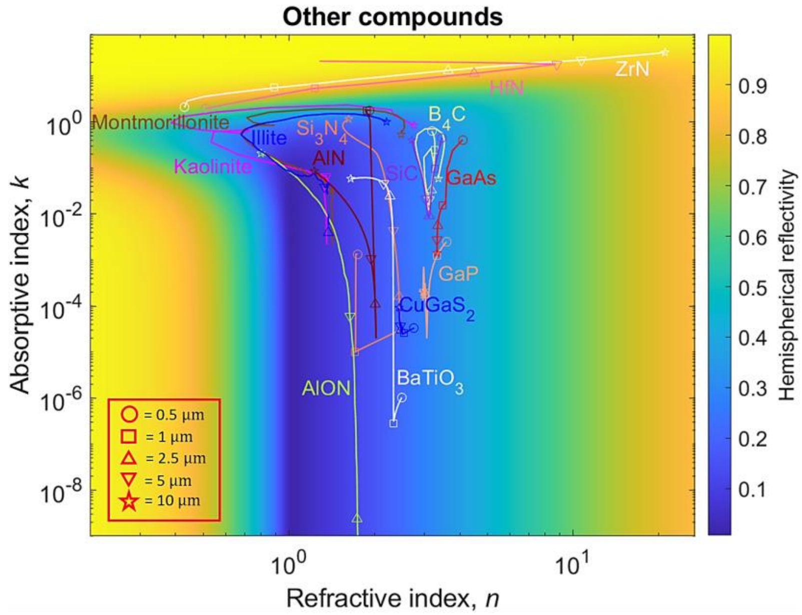

c

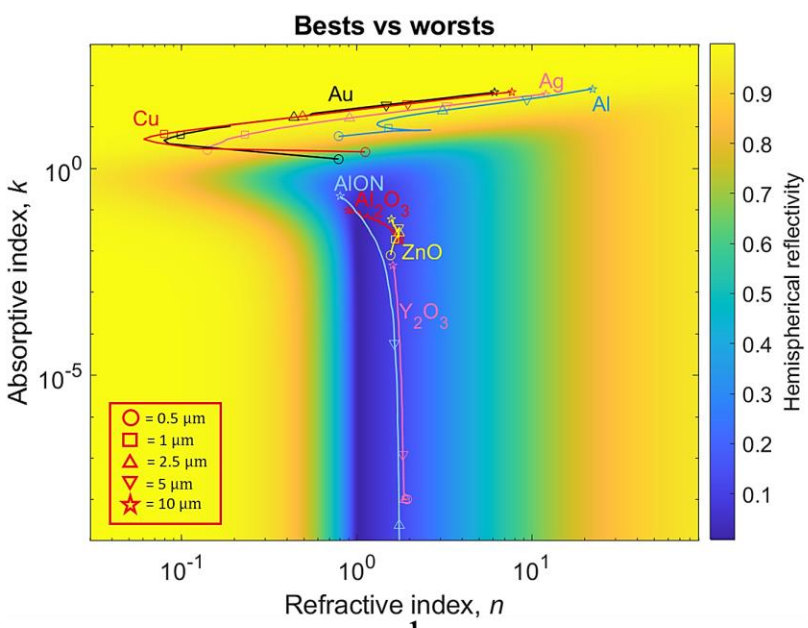

d

Figure 3.5. Evaluation of different materials performance based on the connection between the hemispherical reflectivity and their complex index of refraction for; a) metals, b) oxides, and c) other compounds. d) shows the most reflective materials vs. the least reflectives.

Figure 3.5 shows the performance of various materials to reflect the radiation in the wavelength range of $0.5 - 10$ [μm]. Materials have been classified into three different groups of; metals, simple oxides and other compounds. As can be seen, metals lie in the maximum region of hemispherical reflectivity (figure 3.5. (a)) which indicates that metals have a much higher reflectivity compared to the non-metals such as oxides, clays, nitrides or other compounds (figure 3.5. (b) and figure 3.5. (c)). This reveals that multilayer insulation system works best with metals that have the highest reflectivity to minimize the radiative losses. An overview of studies on the MLI design indicates that metals are the most commonly used materials as shields in this design [30][34]. Our methodology in fact provides a comprehensive investigation on a wide range of materials in different types and proves that metals are the best option to reflect the radiation. The present methodology can also be used to have a comparison between the metals to find the most reflective one. In spite of the fact that metals possess a very high reflectivity, using them as highly reflective shields in the MLI design have two main limits at high temperatures. The first limit is that most of the metals have melting temperature lower than 2000 [K] which disqualifies them for using in the ultra-high temperature applications. Table 3.1 lists the melting point of several metals [83]. The second and the most important limit with respect to metals is that they have the tendency to oxidize at high temperatures [44][45]. The nickel oxide scale growth, for example, as a function of time and temperature is shown in figure 3.6 [46] which indicates that increasing the temperature accelerates the oxidation rate substantially. Oxidization influences the surface properties of metals and lowers their reflectivity significantly. At high temperatures, metals which are shown as the highest reflective materials will turn into the metal oxides which are considered as the worst materials in the view of high reflectivity (as demonstrated in figure 3.5. (d)). Taking Al and Cu, for example, as two of the most effective materials for suppressing the radiation, they will change into Al_2O_3 and Cu_2O, respectively, at high temperatures which are quite ineffective materials to reflect the radiation (figure 3.7). Therefore, the multilayer insulation design is fated to be either unsuitable (if using metals as radiative shields) or non-optimal (if using non-metals with lower reflectivity as shields) at high temperatures. That is why MLI design is often used in spacecraft, cryogenics and other applications in vacuum where oxidization is not a problem [31][86][87]. For use in high temperature applications, the MLI is suggested to utilize vacuum technologies which are high in cost and susceptible to mechanical damages.

Table 3.1. Metals melting point [83].

Metal	**Melting point (K)**	**Metal**	**Melting point (K)**
Aluminum	933	Iron	1811
Copper	1358	Dysprosium	1680
Gold	1337	Erbium	1802
Silver	1235	Ruthenium	2607
Molybdenum	2896	Rhenium	3459
Nickel	1726	Lead	600
Platinum	2041	Bismuth	544
Titanium	1941	Cadmium	594
Tungsten	3695	Chromium	2180
Zinc	693	Cobalt	1768

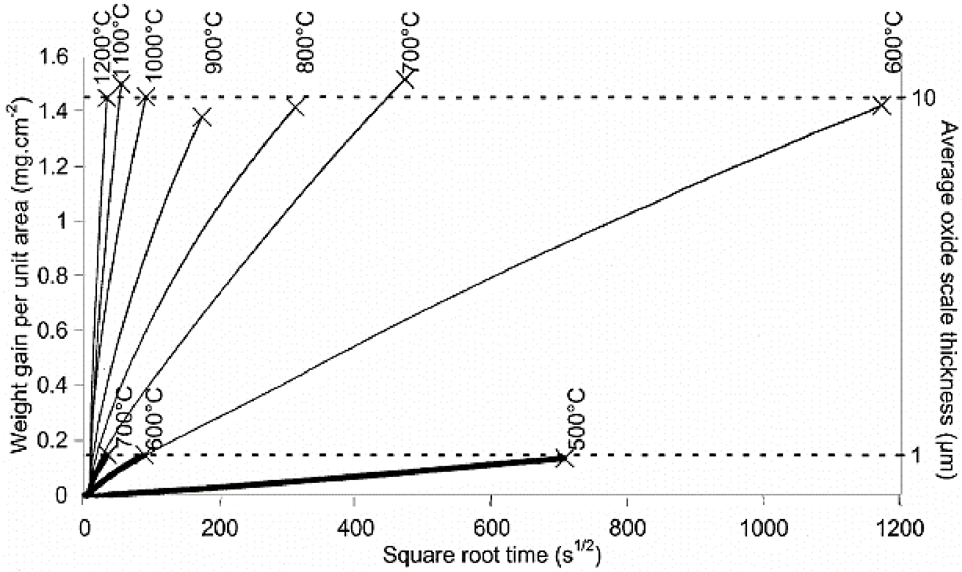

Figure 3.6. Oxide scale growth of NiO as a function of time for oxidation of pure Nickel [46].

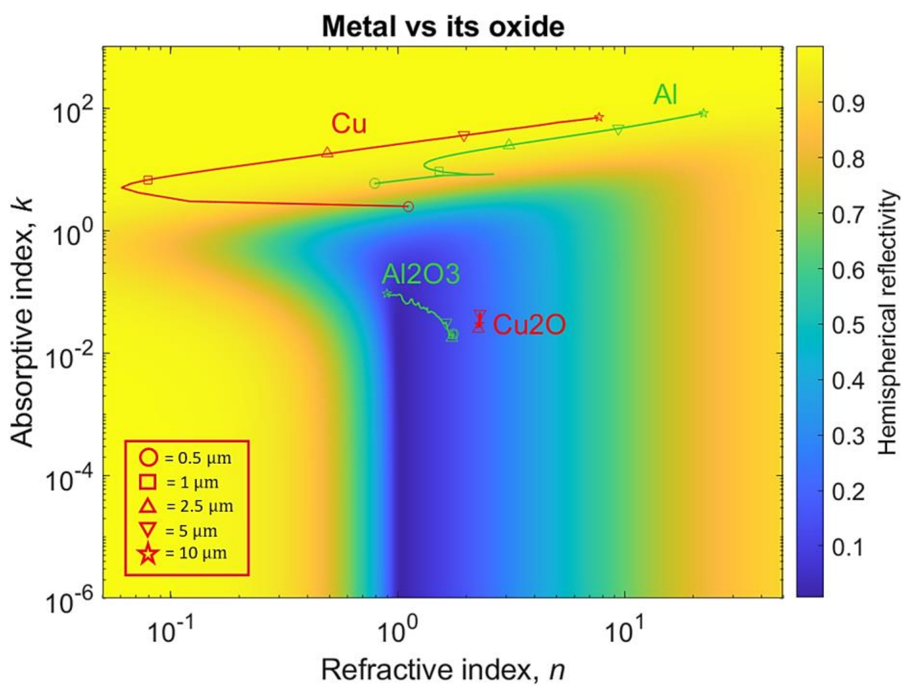

Figure 3.7. The hemispherical reflectivity of Al and Cu vs. their oxides, Al_2O_3 and Cu_2O.

3.3 Application of the theory to the MLI design

So far, the radiative heat transfer phenomenon through the MLI system was described through a model and the reflectivity of several materials was studied. In this section, we explain how to apply the theory to the MLI design to calculate the performance of a given material, as reflective shields for suppressing the radiation. For this purpose, we set a goal which is coming up with an insulation design that has a good effective thermal conductivity (lower than 0.1 [$\mathrm{W\,m^{-1}K^{-1}}$]) at high temperatures. For example, we consider an insulation material that has an effective thermal conductivity lower than 0.08 [$\mathrm{W\,m^{-1}K^{-1}}$] at temperature $T = 1273$ [K]. By applying the theory presented in the previous sections, we study the performance of four representative materials, Al and Cu as highly reflective materials and Al_2O_3 and Cu_2O as poorly reflective materials. For each material, we calculated the number of shields that is needed to reach $k_{\mathrm{eff}} \leq 0.08$ [$\mathrm{Wm^{-1}K^{-1}}$].

If we assume that the thickness of the insulation is 10 [cm] and one side of it is exposed to a high temperature of $T_2 = 1273$ [K], while the other side is at the room temperature ($T_1 = 298$ [K]), then we can calculate the effective emissivity by re-arranging Equation 1.8 as:

$$\varepsilon_{\mathrm{eff}} = \frac{k_{\mathrm{eff}}}{L\sigma(T_1^2 + T_2^2)(T_1 + T_2)} = \frac{0.08}{0.1(5.67 \times 10^{-8})(298^2 + 1273^2)(298 + 1273)} = 0.0053$$

To calculate the number of shields that is needed to reach $\varepsilon_{\mathrm{eff}} \leq 0.0053$, first the emissivity of the shields must be determined. We use Equations 3.17-3.22 to determine the spectral normal and the spectral hemispherical reflectivities for each material. Considering that the shields are opaque (no transmittance), emissivity of the shields can be defined using

Equation 3.10. Figure 3.8 demonstrates the results for Cu, Cu_2O, Al, and Al_2O_3. The right Y-axis shows the blackbody spectral hemispherical emissive power (Planck function) that is calculated for different temperatures.

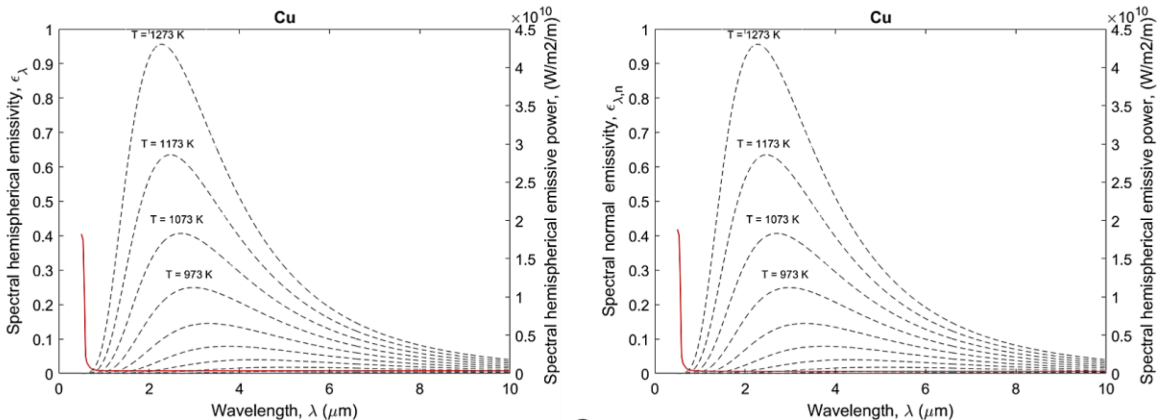

a

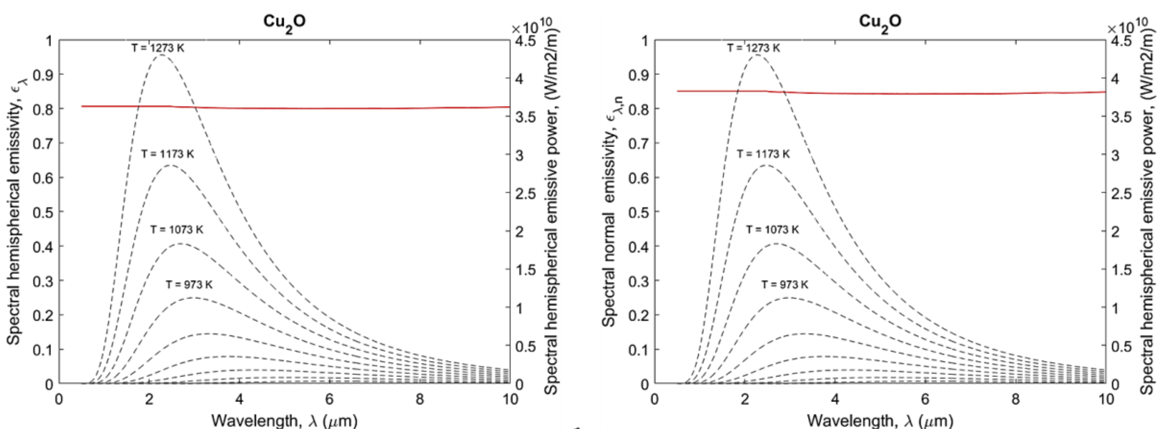

b

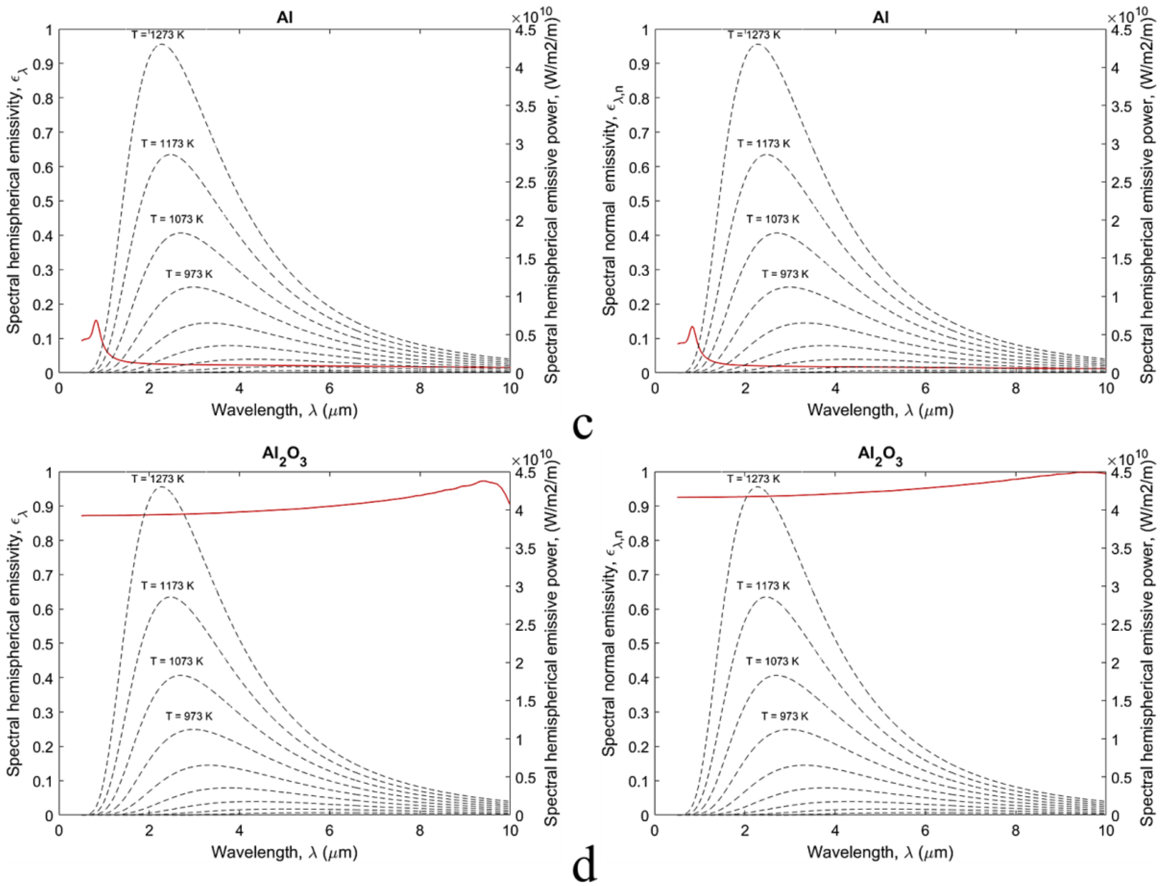

Figure 3.8. Spectral normal emissivity and spectral hemispherical emissivity as a function of wavelength for a) Cu, b) Cu_2O, c) Al, d) Al_2O_3.

To determine the total emissivity at a specific temperature, we use the Planck function to have a spectrally averaged of emissivity over the range of wavelength (the procedure is similar to Equation 4.14 in Chapter 4). Therefore, the total normal emissivity and total hemispherical emissivity are weighted by the blackbody emission spectrum and can be expressed, respectively as:

$$\varepsilon_n(T) = \frac{\int_{\lambda=0}^{\infty} \varepsilon_{\lambda,n} E_{\lambda b}(T) d\lambda}{\int_{\lambda=0}^{\infty} E_{\lambda b}(T) d\lambda} = \frac{\int_{\lambda=0}^{\infty} \varepsilon_{\lambda} E_{\lambda b}(T) d\lambda}{\sigma T^4} \qquad (3.23)$$

$$\varepsilon(T) = \frac{\int_{\lambda=0}^{\infty} \varepsilon_\lambda E_{\lambda b}(T) d\lambda}{\int_{\lambda=0}^{\infty} E_{\lambda b}(T) d\lambda} = \frac{\int_{\lambda=0}^{\infty} \varepsilon_\lambda E_{\lambda b}(T) d\lambda}{\sigma T^4} \tag{3.24}$$

The total normal emissivity and total hemispherical emissivity Cu, Al, Cu_2O and Al_2O_3 were calculated using Equations 3.23 and 3.24 for the wavelength range of $0.5 - 10$ [μm]. The results are shown in Figure 3.9.

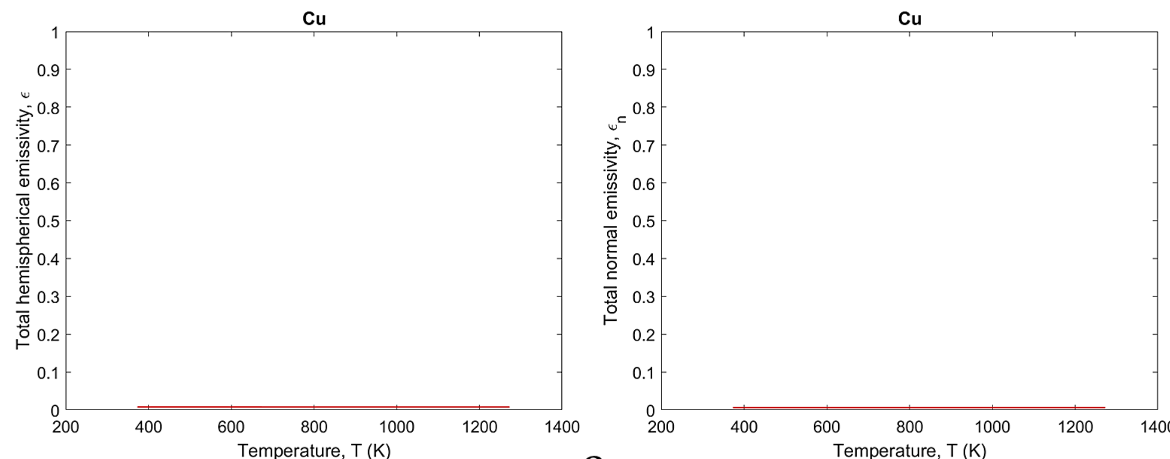

a

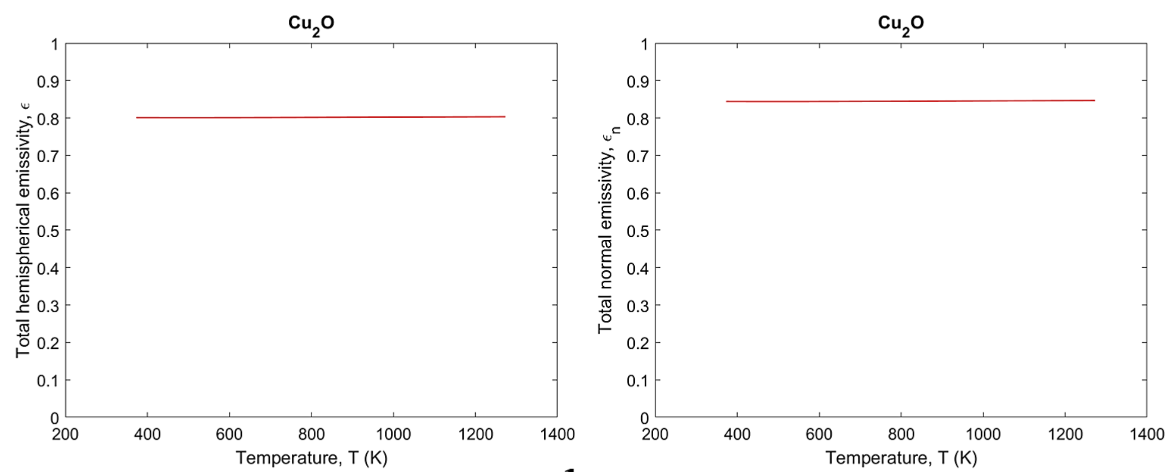

b

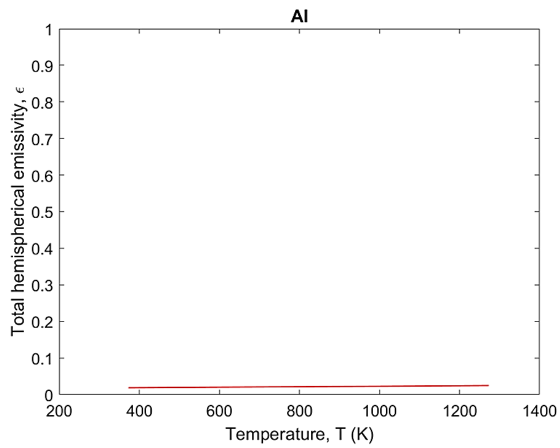

c

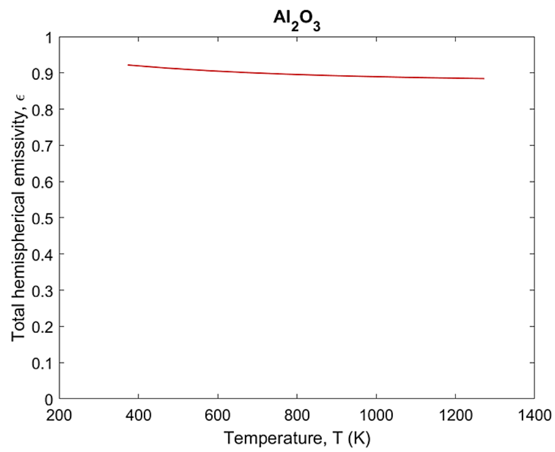

d

Figure 3.9. The total normal emissivity and total hemispherical emissivity as a function of temperature for a) Cu, b) Cu_2O, c) Al, d) Al_2O_3.

As can be seen in Figure 3.9, the total emissivity of these materials is not a strong function of temperature. Therefore, we can use a single value of total emissivity to calculate the number of shields that is needed to reach $k_{\text{eff}} \leq 0.08\ [\text{Wm}^{-1}\text{K}^{-1}]$. We assume that the top and bottom surfaces have emissivity of 0.5 ($\varepsilon_1 = \varepsilon_2 = 0.5$) and there are N_S number of reflective shields between them. According to Equation 3.4, ε_{eff} can be defined as:

$$\varepsilon_{\text{eff}} = \frac{1}{\left(\frac{1}{\varepsilon_1} + \frac{1}{\varepsilon_2} - 1\right) + N_{\text{S}} * \left(\frac{2}{\varepsilon} - 1\right)} \tag{3.25}$$

For Cu, the average values of total hemispherical emissivity and total normal emissivity are 0.008 and 0.006, while the range of emissivity reported in the literature is 0.02-0.07 (see Table 3.2 [85]). As we see, the calculated total emissivity of Cu is lower than the range reported in the literature. The reason might be that we considered the spectral emissivity in the wavelength range of $0.5 - 10$ [μm] to calculate the total emissivity and Cu has a very low emissivity in this range, while for lower wavelengths it has a much higher emissivity. Using the total hemispherical emissivity of Cu in Equation 3.26, the number of Cu shields that we need to place inside the insulation to reach $k_{\text{eff}} \leq 0.08$ [$\text{Wm}^{-1}\text{K}^{-1}$] ($\varepsilon_{\text{eff}} \leq 0.0053$) can be calculated as:

$$N_{\text{Cu}} = \frac{1 - \varepsilon_{\text{eff}} * \left(\frac{1}{\varepsilon_1} + \frac{1}{\varepsilon_2} - 1\right)}{\varepsilon_{\text{eff}} * (\frac{2}{\varepsilon} - 1)} = \frac{1 - 0.0053 * \left(\frac{1}{0.5} + \frac{1}{0.5} - 1\right)}{0.0053 * \left(\frac{2}{0.008} - 1\right)} = 0.75 \approx 1$$

For Cu_2O, the average values of total hemispherical emissivity and total normal emissivity are 0.8 and 0.84, respectively. Both values are in the range of values reported in the literature ($0.77 -$ 0.87). Using the total hemispherical emissivity of Cu_2O in Equation 3.26, the number of Cu_2O shields needed to reach $k_{\text{eff}} \leq 0.08$ [$\text{Wm}^{-1}\text{K}^{-1}$] ($\varepsilon_{\text{eff}} \leq 0.0053$) can be determined as:

$$N_{\text{Cu}_2\text{O}} = \frac{1 - \varepsilon_{\text{eff}} * \left(\frac{1}{\varepsilon_1} + \frac{1}{\varepsilon_2} - 1\right)}{\varepsilon_{\text{eff}} * \left(\frac{2}{\varepsilon} - 1\right)} = \frac{1 - 0.0053 * \left(\frac{1}{0.5} + \frac{1}{0.5} - 1\right)}{0.0053 * \left(\frac{2}{0.8} - 1\right)} = 124.88 \approx 125$$

With respect to Al, the average values of total hemispherical emissivity and total normal emissivity are 0.022 and 0.017, respectively. While, the range of values in the literature is 0.02-0.06. Using the total hemispherical value, the number of Al shields can be defined as:

$$N_{\mathrm{Al}} = \frac{1 - \varepsilon_{\mathrm{eff}} * \left(\frac{1}{\varepsilon_1} + \frac{1}{\varepsilon_2} - 1\right)}{\varepsilon_{\mathrm{eff}} * (\frac{2}{\varepsilon} - 1)} = \frac{1 - 0.0053 * \left(\frac{1}{0.5} + \frac{1}{0.5} - 1\right)}{0.0053 * \left(\frac{2}{0.022} - 1\right)} = 2.083 \approx 3$$

Finally, for Al_2O_3, the average values of total hemispherical emissivity and total normal emissivity are 0.9 and 0.95. However, this value is much higher than the reported value in the literature (0.2-0.31). The reason might be that we assumed that Al_2O_3 is completely opaque in our calculations, while in fact a layer of aluminum oxide has a certain amount of transmittance in the infrared region which cannot be neglected [84] unless it is a very thick slab of material. Therefore, we consider two cases of Al_2O_3 to calculate the number of shields. In the first case, we consider a very thick layer of pure Al_2O_3 so that there is no transmittance. Hence, the value of total emissivity is 0.9 and the number of Al_2O_3 shields can be defined as:

$$N_{\mathrm{Al_2O_3}} = \frac{1 - \varepsilon_{\mathrm{eff}} * \left(\frac{1}{\varepsilon_1} + \frac{1}{\varepsilon_2} - 1\right)}{\varepsilon_{\mathrm{eff}} * \left(\frac{2}{\varepsilon} - 1\right)} = \frac{1 - 0.0053 * \left(\frac{1}{0.5} + \frac{1}{0.5} - 1\right)}{0.0053 * \left(\frac{2}{0.9} - 1\right)} = 153.27 \approx 154$$

In the second case, we consider that Al partially oxidizes and there is a thin layer of Al_2O_3. Therefore, by using an average value of emissivities reported in the literature ($\varepsilon = 0.25$) [85], the number of Al_2O_3 shields that is needed to have $k_{\mathrm{eff}} \leq 0.08\ [\mathrm{Wm^{-1}k^{-1}}]$ ($\varepsilon_{\mathrm{eff}} \leq 0.0053$) is:

$$N_{\mathrm{Al_2O_3}} = \frac{1 - \varepsilon_{\mathrm{eff}} * \left(\frac{1}{\varepsilon_1} + \frac{1}{\varepsilon_2} - 1\right)}{\varepsilon_{\mathrm{eff}} * \left(\frac{2}{\varepsilon} - 1\right)} = \frac{1 - 0.0053 * \left(\frac{1}{0.5} + \frac{1}{0.5} - 1\right)}{0.0053 * \left(\frac{2}{0.25} - 1\right)} = 26.76 \approx 27$$

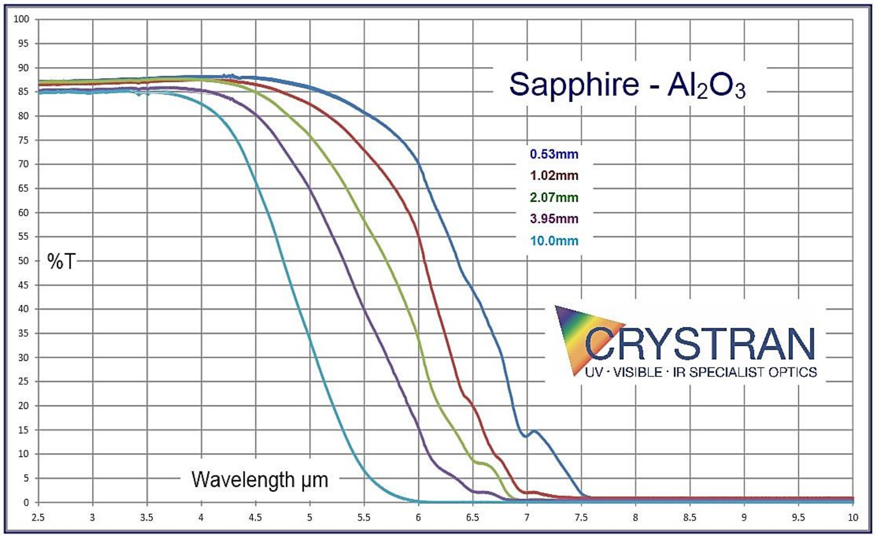

Figure 3.10. Transmittance of a layer of Al_2O_3 with different thicknesses as a function of wavelength [84].

Table 3.2. Emissivity of materials [85].

Material	Emissivity-literature values	Emissivity-calculated values ($\varepsilon_{\mathrm{hemispherical}}$)	Emissivity-calculated values ($\varepsilon_{\mathrm{normal}}$)
Al	0.02− 0.06	0.022	0.017
Cu	0.02− 0.07	0.008	0.006
Al_2O_3	0.2− 0.31	0.9	0.95
Cu_2O	0.77− 0.87	0.8	0.84

Results of calculated number of shields for the investigated materials are shown in Table 3.3. As can be seen, using 3 and 1 numbers of Al and Cu, respectively, inside the insulation medium can decrease the thermal conductivity to $0.08\ [\mathrm{Wm^{-1}K^{-1}}]$ which shows the excellent performance of pure metals. However, they will oxidize at high temperatures and an oxide layer would form on their surface which lowers their performance significantly. Forming a layer of Cu_2O on the Cu surface would increase the needed number of shields from 1 to 125. With respect to Al, forming a thin and thick layer of oxide on its surface would increase the number of shields from 3 to 27 and 154, respectively.

Table 3.3. Number of shields needed to be placed in a slab of insulation with thickness of 10 [cm] to reach $\boldsymbol{k_{\mathrm{eff}} \leq 0.08}$ $[\mathbf{Wm^{-1}K^{-1}}]$ at $\boldsymbol{T = 1273}$ $[\mathbf{K}]$.

Material	**Number of shields**
Cu	1
Cu_2O	125
Al	3
Thin layer of Al_2O_3	154
Thick layer of Al_2O_3	27

Accordingly, it seems that with metals, a relatively small number of shields are needed to meet the target thermal conductivity value. However, it should be kept in mind that the real challenge is that metals don't perform well at high temperatures since they will oxidize or melt, in worst case. On the other hand, oxides that are naturally stable materials at high temperatures, do not have a good performance at suppressing the radiation since they have a low reflectivity. Therefore, even though MLI approach seems to be theoretically feasible in that using small number of metals results in a very low thermal conductivity, there are practical challenges that necessitates the search for an alternative approach for suppressing the radiation at high temperatures.

Chapter 4
Volumetric extinction design

The performance of MLI design at high temperatures was summarized in Chapter 2. The theoretical analysis showed that the MLI design is fated to either be inappropriate or insufficient at high temperatures. Volumetric extinction is an alternative approach for suppressing radiative transport at high temperatures. Chapter 4 investigates the performance of the volumetric extinction design through a theoretical approach.

4.1 Minimizing the radiative heat transfer in the volumetric extinction design

The volumetric approach utilizes radiatively participating (absorbing/scattering) particles dispersed throughout a low-conductivity host medium. The function of the design to suppress the radiation was discussed in chapter 2. To describe the radiative heat transfer through the system, consider a simple configuration of a participating medium placed between two infinite gray diffuse plates with emissivities ε_1 and ε_2 maintained at uniform temperatures of T_1 and T_2, respectively (Figure 4.1).

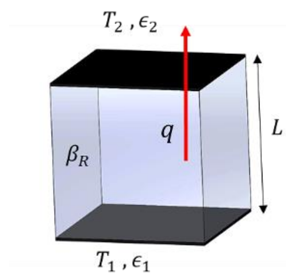

Figure 4.1. A participating medium with a mean extinction coefficient ($\boldsymbol{\beta}_{\mathbf{R}}$) placed between two infinite gray diffuse plates.

Considering that the participating media is optically thick, the one-dimensional radiative heat flux through the design can be described as [42]:

$$q_r = \frac{\sigma(T_1^4 - T_2^4)}{\frac{3}{4}\beta_{\mathrm{R}}L + \frac{1}{\varepsilon_1} + \frac{1}{\varepsilon_2} - 1} \tag{4.1}$$

where β_{R} is the Rosseland mean extinction coefficient which is spectrally averaged of spectral extinction coefficient, β_λ, over wavelengths (will be explained in section 4.3) and L is the thickness. As we will see in section 4.3, the Rosseland mean extinction coefficient is a function of temperature and it can be calculated at a representative temperature inside a non-gray medium not for the whole medium, since the medium is not isothermal. However, if we assume that the medium is gray, the extinction coefficient is not a function of wavelength then we just have β instead of β_{R} in Equation 4.1.

In the volumetric design, the extinction coefficient of the participating medium (which is a volumetric property) is the most important parameter to control the heat transfer rate. Due to equation 4.1, increasing the extinction coefficient decreases the radiative heat transfer. Therefore, the aim is to maximize the extinction coefficient of the design.

4.2 Spectral extinction coefficient by Rayleigh theory

The spectral extinction coefficient is a combination of the spectral absorption (κ_λ) and spectral scattering coefficient (σ_λ) [10] as:

$$\beta_\lambda = \kappa_\lambda + \sigma_\lambda \tag{4.2}$$

Effective absorption and scattering coefficients for clouds of particles can be determined by different theories. To select the suitable theory, it is important to define the state of scattering (dependent or independent). In case of dependent scattering, scattering from surrounding particles affects the scattering behavior of a given particle (known as the "near-field" effect) and also interferes with the incident radiation field which known as the "far-field" effect. For the independent scattering, the clearance between the particles is considered to be sufficiently large so that each of particles is exposed to a parallel beam of light, and there is an enough space for each particle to have an independent scattering pattern without any disturbance by surrounding particles. The state of scattering depends on two variables; 1) size parameter, and 2) volume fraction [10]. Size parameter is a non-dimensional scaling parameter which compares the size of the particles to the wavelength of the incident radiation. For spherical particles, size parameter is expressed as the ratio of the perimeter of the particle with diameter *D* to the wavelength of the light (equation 4.3).

$$\xi = \frac{\pi D}{\lambda} \tag{4.3}$$

For a cloud of particles with a single size, the volume fraction can be defined as:

$$f_v = \frac{V_{\text{particles}}}{V_{\text{tot}}} = N\pi \frac{D^3}{6} \tag{4.4}$$

where N (number density) is number of particles per a given volume. Figure 4.2 [10] shows the regions of dependent and independent scattering as a function of size parameter and volume fraction. As can be seen, the near-field and far-filed effects play a more important role at larger particle volume fractions.

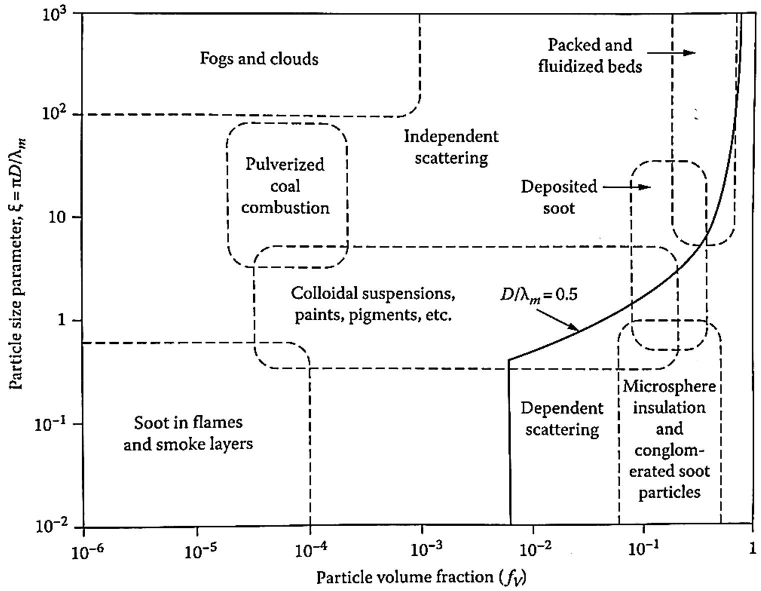

Figure 4.2. Dependent and independent scattering regions based on size parameter and volume fraction [10].

Considering Figure 4.2, the simplest condition is when the size of particles is much smaller than the wavelength of radiation and the volume fraction is vey low (lower than 0.006 approximately) which guarantees independent scattering. In this case, the Rayleigh theory can be used to determine the absorption and scattering coefficients of particles. In the Rayleigh theory, the particle size is assumed to be much smaller than the wavelength of the incident radiation (($\xi = \pi D/\lambda) < 0.1$ [47]).

The absorption and scattering coefficients can be expressed in terms of the particle density and the cross-sections of an individual particle as:

$$\kappa_\lambda = NC_{\lambda,a} = NQ_{\lambda,a}\pi\frac{D^2}{4} \qquad \sigma_\lambda = NC_{\lambda,s} = NQ_{\lambda,s}\pi\frac{D^2}{4} \tag{4.5}$$

where $C_{\lambda,a}$ and $C_{\lambda,s}$ are the absorption and scattering cross sections, and $Q_{\lambda,a}$ and $Q_{\lambda,s}$ are efficiency factors with respect to absorption and scattering, respectively [10]. $\pi\frac{D^2}{4}$ is the geometrical cross section with respect to a sphere of diameter *D*. Efficiency factors for scattering and absorption are ratio of scattering and absorption per the geometrical cross section of particles. Generally, the scattering and absorption efficiency factors are dependent on the orientation of the particles and the state of polarization of the incident light beam. However, for spherical particles, their efficiency factors are not dependent of these parameters because of the symmetry [48].

Based on the Rayleigh theory, $Q_{\lambda,a}$ and $Q_{\lambda,s}$ can be defined as [10]:

$$Q_{\lambda,s} = \frac{8}{3}\xi^4 \left|\frac{\bar{n}^2 - 1}{\bar{n}^2 + 1}\right|^2 \qquad \bar{n} = \frac{n_2 - ik_2}{n_1 - ik_1} \tag{4.6}$$

$$Q_{\lambda,a} = -4\xi Im\left(\frac{\bar{n}^2 - 1}{\bar{n}^2 + 1}\right) \qquad \bar{n} = \frac{n_2 - ik_2}{n_1 - ik_1} \tag{4.7}$$

Subscript 1 is with respect to the host medium, while subscript 2 refers to the particles. Based on equations 4.6 and 4.7, it can be noted that $Q_{\lambda,a}$ is proportional to ξ, while $Q_{\lambda,s}$ is proportional to ξ^4. Since ξ is assumed to be very small in the Rayleigh theory, scattering by small particles may be neglected as compared with absorption [42]. Therefore, the spectral extinction coefficient is approximately equal to the spectral absorption coefficient as:

$$\beta_\lambda = N(Q_{\lambda,a} + Q_{\lambda,s})\pi\frac{D^2}{4} = NQ_{\lambda,a}\pi\frac{D^2}{4} \tag{4.8}$$

For simplification, we assume that participating particles are dispersed in a non-participating host medium such as air or vacuum ($n_1 = 1,\ k_1 = 0$). Then, equation 4.7 can be re-written as [10]:

$$Q_{\lambda,a} = \frac{24\pi D}{\lambda}\left[\frac{nk}{(n^2 - k^2 + 2)^2 + 4n^2k^2}\right] \tag{4.9}$$

If we plug $Q_{\lambda,a}$ from equation 4.9 into equation 4.8, then β_λ can expressed as [42]:

$$\beta_\lambda = \frac{6N\pi^2 D^3}{\lambda}\left[\frac{nk}{(n^2 - k^2 + 2)^2 + 4n^2k^2}\right] \tag{4.10}$$

Equation 4.10 can be written as a function of volume fraction instead of particle diameter. Then, considering equations 4.4 and 4.10, the spectral extinction coefficient can be determined as:

$$\beta_\lambda = \frac{3}{2}\frac{f_v}{D}Q_{\lambda,a} = \frac{36\pi f_v}{\lambda}\left[\frac{nk}{(n^2 - k^2 + 2)^2 + 4n^2k^2}\right] \tag{4.11}$$

Therefore, in the Rayleigh theory that holds for very small particles, the absorption coefficient only depends on the volume fraction of particles not on the particle size distribution.

As mentioned in the previous section, the target is to maximize the extinction coefficient of the design in order to minimize the radiative losses. As can be seen in equation 4.11, the extinction coefficient is a function of volume fraction, wavelength, and the real and the imaginary parts of the refractive index. To have a general investigation which is independent of volume fraction and wavelength, we can introduce the reduced form of the extinction coefficient which is only a function of materials properties (n and k) as:

$$\frac{\beta_\lambda}{(\frac{f_v}{\lambda})} = 36\pi[\frac{nk}{(n^2 - k^2 + 2)^2 + 4n^2k^2}] \tag{4.12}$$

Equation 4.12 states the connection between the reduced extinction coefficient of the design and the two independent parameters of n and k. Figure 4.3 shows a surface plot of reduced extinction coefficient as a function of n and k, indicating at what range of n and k the reduced extinction coefficient is high. In fact, Figure 4.3 represents a novel performance plot for the volumetric design which is useful to evaluate the opacifying performance of any types of material. It is seen that when k is around 1.4 and n is lower than around 2, reduced extinction coefficient has the highest value.

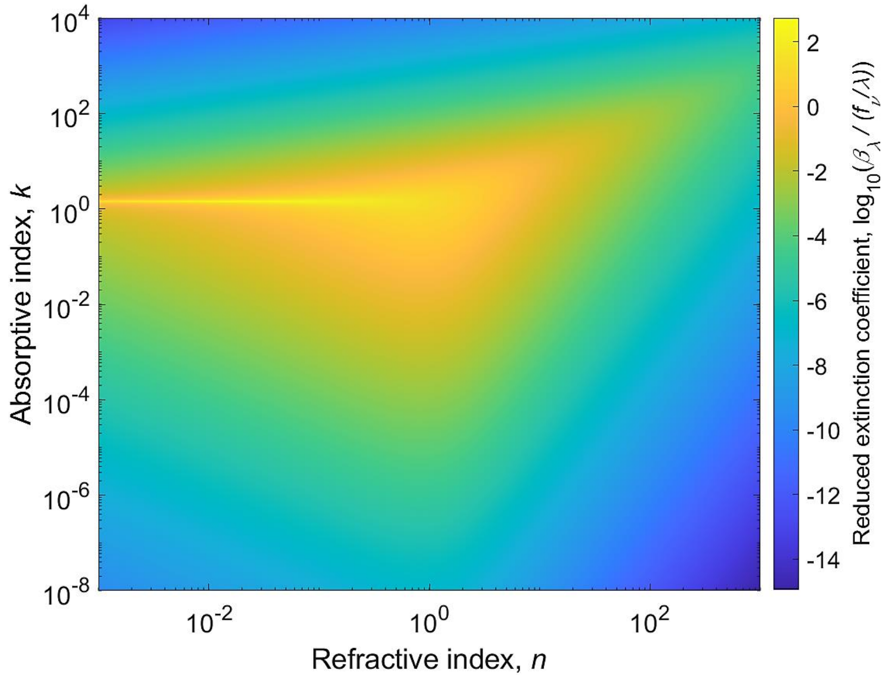

Figure 4.3. Reduced extinction coefficient as a function of n and k.

4.3 Materials investigation based on spectral and mean extinction coefficients

In previous studies, the performance of some materials such as Al_2O_3, TiO_2, SiC and ZrO_2 as opacifying patricles has been investigated. They indicated that SiC is one the materials that has a desirable opacifying performance. Even though the opacifying performance of several materials have been evaluated in the past studies, they did not provide a general methodology by which every material can be evaluated. Figure 4.3 allows us to consider different groups of materials and to have a comprehensive comparison between them. Therefore, the performance of different materials can be evaluated to find materials with having the maximum ability of radiation extinction to use as dispersed opacifier particles. For various representative materials, a curve of k as a function of n has been plotted and superimposed onto the reduced spectral extinction coefficient map to see where the curve of each material lies. The materials that lie on the maximum extinction region are the optimal materials. The result has been shown in figure 4.4 which is classified into metals, oxides, and other compounds including some nitrides, carbides, perovskites and so on. Table 4.1 shows the list of references for the investigated materials. The curves in figure 4.4 are prepared for wavelength in rage 0.5-10 [μm]. The investigation shows that:

- Unlike the MLI design that was shown to work best with metals, there are many non-metal materials that exhibit a very effective performance for attenuating the radiation, yet withstand the extremely high temperatures. Among the investigated materials some oxides such as Fe_3O_4, clays, and some perovskites such as $LaFeO_3$ show a good performance.

- A comparison between the metals and their oxides shows that oxides have a higher performance as opacifiers in the volumetric design. In Chapter 3 it was demonstrated that Al_2O_3 and Cu_2O have a very poor performance in the MLI design compared to Al and Cu which indicates the limitation of the MLI design at high temperatures. The investigation of the volumetric extinction design, in contrast, shows that Al_2O_3 and Cu_2O perform even better than Al and Cu which indicates that their oxidization at high temperatures is in favor of the radiation extinction.
- Even though some materials such as Dysprosium (Dy), Erbium (Er) and Thulium (Tm) which are located at a high region of the map represent a good extinction ability, they are metals and they will not survive at high temperatures.

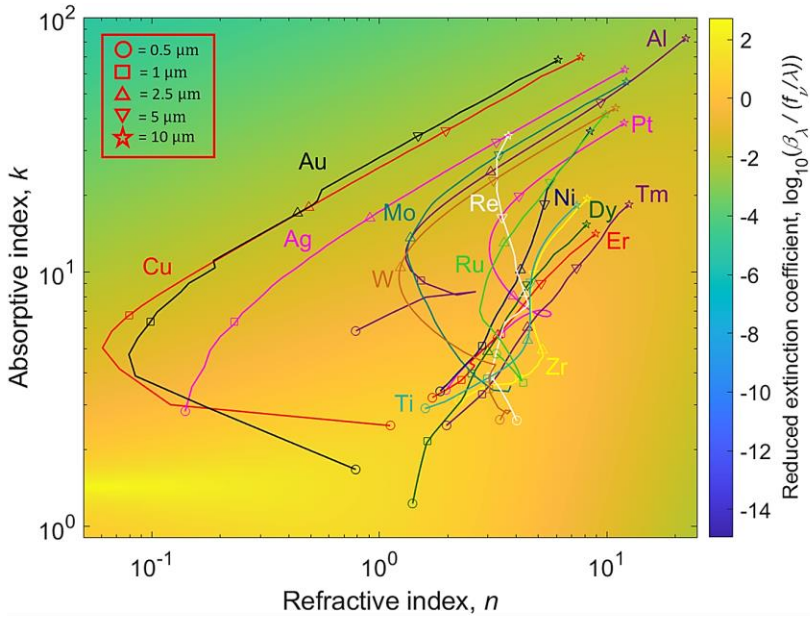

a

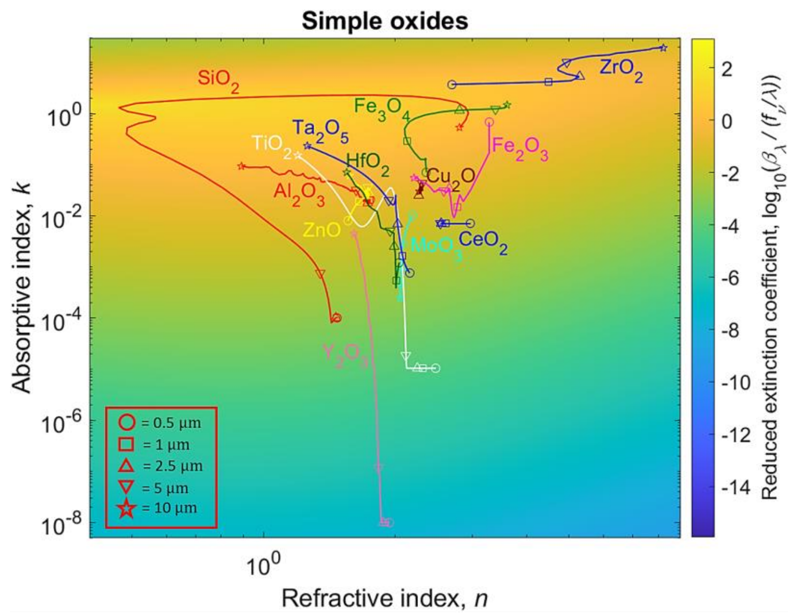

b

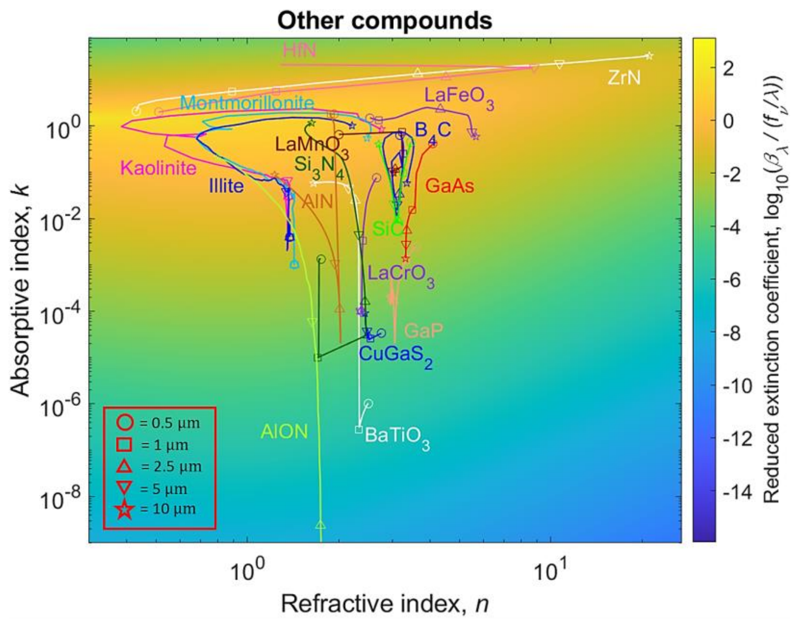

c

Figure 4.4. Evaluation of different materials performance based on their optical properties and the reduced extinction coefficient color map.

Table 4.1. List of the references used to export the data of refractive index and absorptive index of materials.

Material	Reference	Material	Reference
Al_2O_3	[49]	ZrO_2	[50]
CeO2	[49]	Ag	[51]
Fe_2O_3	[49]	Cu	[51]
Fe_3O_4	[49]	Al	[51]
ZnO	[49]	W	[51]
MoO_3	[52]	Ti	[51]
SiO_2	[53]	Pt	[51]
TiO_2	[54]	Pd	[51]
HfO_2	[55]	Mo	[56]
Y_2O_3	[57]	Ni	[58]
Illite	[59]	Rh	[60]
Montmorillonite	[59]	Zr	[59]
Kaolinite	[59]	B_4C	[61]
$CuGaS_2$	[62]	ZrN	[63]
GaAs	[64]	SiC	[65]
GaP	[64]	AlN	[66], [67]
HfN	[68]	$BaTiO_3$	[69]
AlON	[70]	Dy	[67]
Er	[71], [67]	Ru	[67], [72]
Tm	[67], [73]	Ta_2O_5	[74]
Fe	[56]	Si_3N_4	[75]
Ta	[56]	$LaFeO_3$	[76]
Si	[77]	$LaMnO_3$	[76]
Zn	[59]	$LaCrO_3$	[76]
SiO	[78]	---	

The reduced extinction coefficient figure is a general map which investigates materials in a general way and doesn't show the influence of wavelength directly. The extinction coefficient determines how strongly a substance attenuates the incident radiation by scattering and absorption. In other words, the extinction coefficient is a measure of the suppression of radiative energy as it travels through the medium and changes strongly by changing the wavelength of the radiation. The next step is to investigate the influence of wavelength on the extinction coefficient of materials. In other words, we will show the performance of materials to extinct the radiation with different wavelengths. The spectral extinction coefficient was calculated for each material by assuming that the particles volume fraction is 0.1% and the diameter of particles is 10 [nm]. Figure 4.5 shows a comparison between the spectral extinction coefficients, β_λ, of different materials as a function of wavelength. The right y-axis shows the blackbody spectral hemispherical emissive power curves ($E_{\lambda b}$) for temperatures of 2000, 1500, 1000 [K] (dashed lines). Blackbody emissive power is a function of temperature and wavelength and is higher at high temperatures which indicates that the higher temperature objectives have, the more radiation are emitted at shorter wavelengths. The blackbody emissive power curves have been used to have a meaningful comparison between the materials behavior in a particular temperature. As the aim is to assess the ability of materials to extinct the radiation at high temperatures, the blackbody emissive power curve with respect to $T = 2000\ [K]$ is more favorable to compare the materials. As can be seen in figure 4.5 (a), the spectral extinction coefficient of metals varies remarkably by changing the wavelength. Although their extinction coefficient is low at large wavelengths, they tend to have a very high extinction coefficient at low wavelengths which is favorable since there is a higher emissive power at wavelengths around 1-3 $[\mu m]$, for the temperature of $T = 2000\ [K]$. However, metals are not good options for such high temperatures since most of them will melt. Moreover, even if their melting point is above the intended operating temperature, they will likely still not survive due to oxidation. Figure 4.5 (b) depicts that there are some high attenuating oxides with having high extinction coefficients such as Fe_3O_4, ZrO_2, and ZnO. Fe_3O_4, for example has a very high spectral extinction coefficient within the entire wavelength range, even higher than all investigated metals. Comparing metals with their oxides, it can be seen that for most metals their oxides have higher extinction coefficients (figure 4.5 (d)) which indicates that oxides may perform even better than metals at high temperatures. Among the other compounds (figure 4.5 (c)) also there are several good materials with high extinction coefficients. ZrN, B_4C, SiC, HfN, and some perovskites such as LaFeO3 and LaMnO3 are shown as effective materials to attenuate the radiation. Montmorillonite, illite and kaolinite clays also have a very high extinction coefficient in the middle infrared region (3-10 [μm]), however, their ability to extinct the shorter wavelengths is lower than some others.

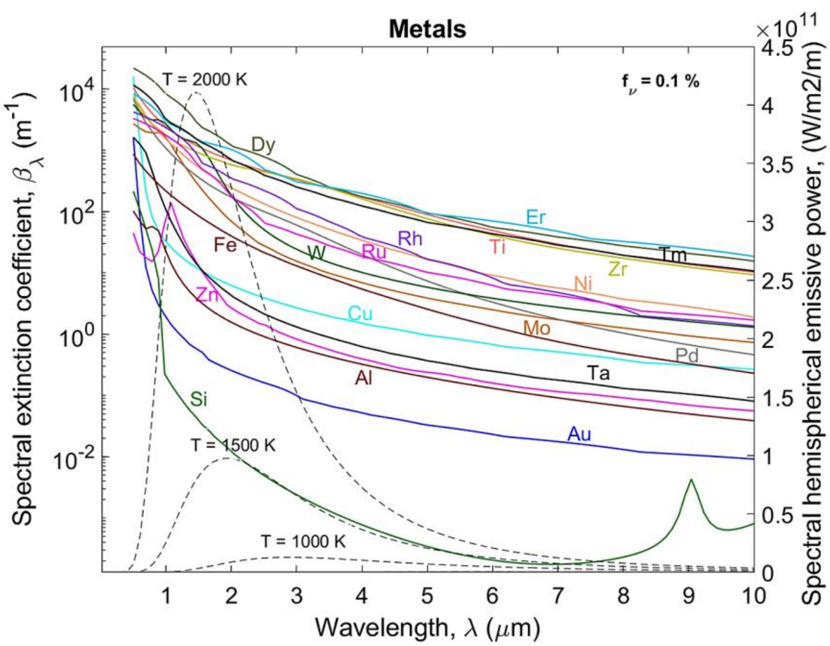

a

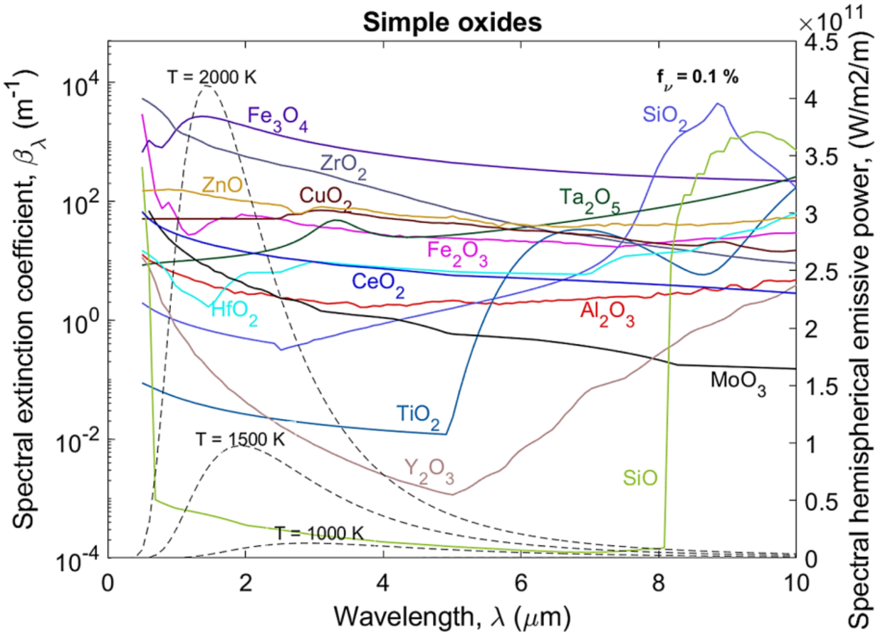
Simple oxides
T = 2000 K
T = 1500 K
T = 1000 K
f_ν = 0.1 %
Fe3O4
ZrO2
ZnO
CuO2
Ta2O5
SiO2
Fe2O3
CeO2
HfO2
Al2O3
MoO3
TiO2
Y2O3
SiO
Spectral extinction coefficient, β_λ (m^-1)
Spectral hemispherical emissive power, (W/m2/m)
Wavelength, λ (μm)

b

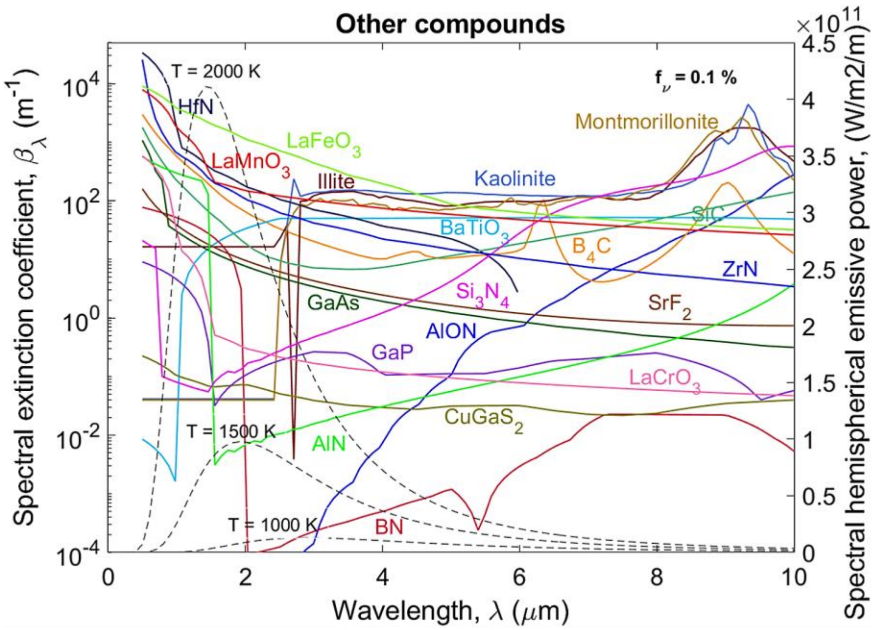
Other compounds
T = 2000 K
T = 1500 K
T = 1000 K
f_ν = 0.1 %
HfN
LaFeO3
LaMnO3
Illite
Kaolinite
Montmorillonite
BaTiO3
SiC
B4C
ZrN
Si3N4
GaAs
AlON
GaP
SrF2
LaCrO3
CuGaS2
AlN
BN
Spectral extinction coefficient, β_λ (m^-1)
Spectral hemispherical emissive power, (W/m2/m)
Wavelength, λ (μm)

c

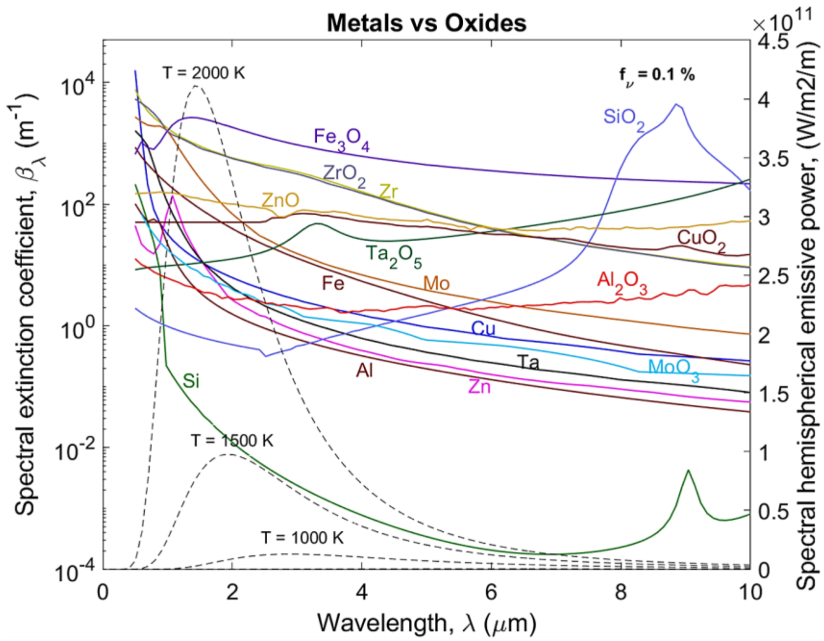

d

Figure 4.5. Spectral extinction coefficient as a function of wavelength for different types of opacifier.

Figure 4.6 also demonstrates a comparison between the spectral extinction coefficients of different materials as a function of wavelength together with the Rosseland function ($\partial E_{\lambda b}/\partial E_b$) in the right y-axis for temperatures of 2000, 1500, 1000 [K] (dashed lines). These curves are useful when we aim for calculating the Rosseland mean extinction coefficient that we will see later.

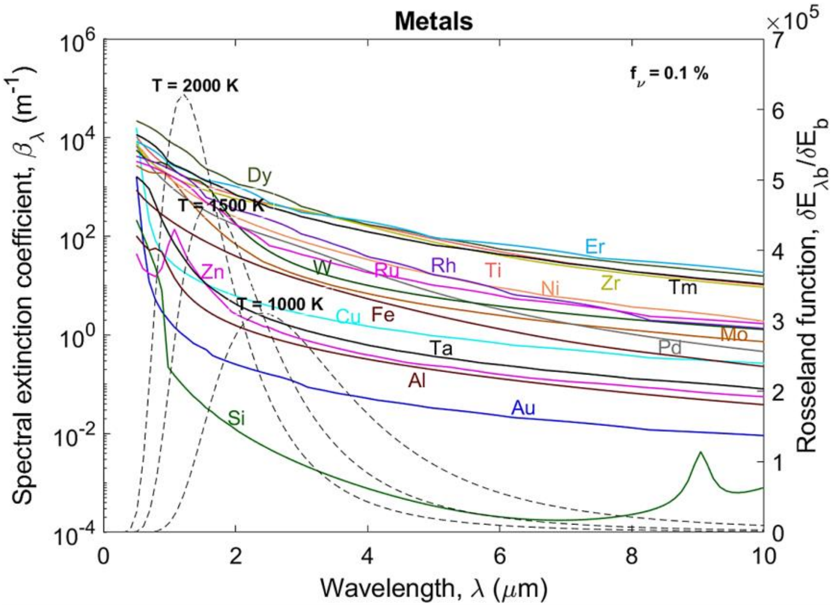
Metals
f_ν = 0.1 %
T = 2000 K
T = 1500 K
T = 1000 K
Dy
Er
W
Ru
Rh
Ti
Ni
Zr
Tm
Zn
Cu
Fe
Mo
Pd
Ta
Al
Au
Si
Spectral extinction coefficient, β_λ (m^-1)
Rosseland function, δE_λb/δE_b
×10^5
Wavelength, λ (μm)

a

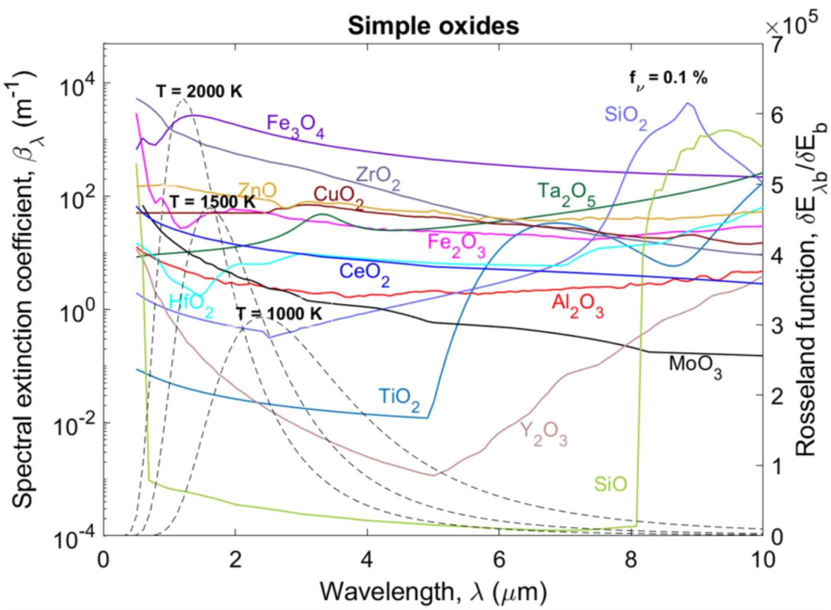
Simple oxides
f_ν = 0.1 %
T = 2000 K
T = 1500 K
T = 1000 K
Fe3O4
ZrO2
ZnO
CuO2
Ta2O5
SiO2
Fe2O3
CeO2
HfO2
Al2O3
MoO3
TiO2
Y2O3
SiO
Spectral extinction coefficient, β_λ (m^-1)
Rosseland function, δE_λb/δE_b
×10^5
Wavelength, λ (μm)

b

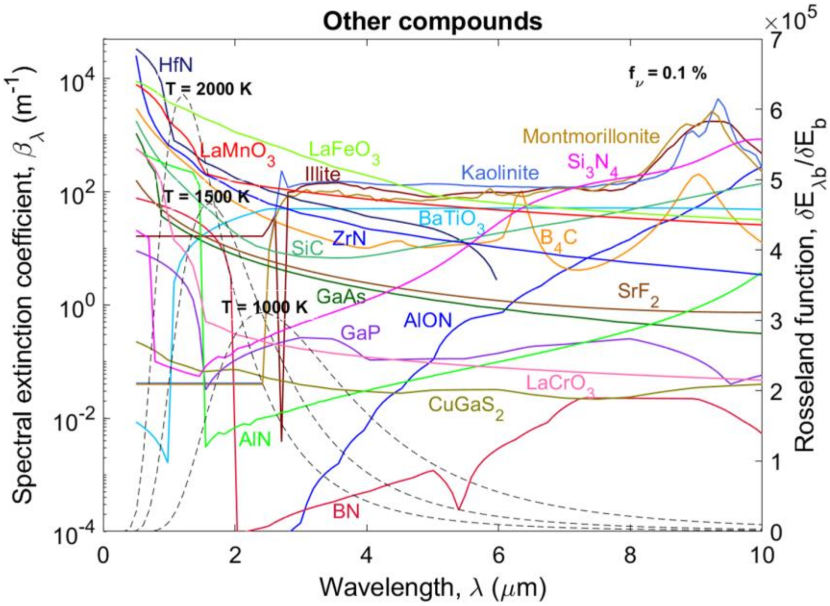

c

Figure 4.6. Spectral extinction coefficient as a function of wavelength together with the Rosseland function.

So far, the materials have been assessed by their spectral extinction coefficients in a range of wavelengths. It was seen that the extinction coefficient of materials can vary significantly with wavelength. Therefore, for the evaluation of total extinction coefficient for the entire range of wavelength it is convenient to use mean extinction coefficients such as Rosseland mean extinction coefficient and Planck mean extinction coefficient which are spectrally averaged over the range of wavelength [42][10]. The mean extinction coefficients are beneficial to assess the overall decay rate of the radiation intensity in the medium.

In the present study, the Rosseland extinction coefficient and the Planck extinction coefficient, as local radiative properties, are used to investigate the radiative heat transfer through the medium. They are local properties since their values change over the thickness as the gradients change. The Rosseland mean extinction coefficient works reasonably well for optically thick media ($\beta_\lambda . L \gg 1$) in which radiation would be attenuated in a short path, while Planck mean extinction coefficient is valid for optically thin situations ($\beta_\lambda . L \ll 1$) [42]. Therefore, they can vary by several orders of magnitude. It should be mentioned that Rosseland mean extinction coefficient is more appropriate here since the diffusion approximation has been used to calculate the heat flux through a slab of material (as seen in Equation 4.1), whereas Planck mean extinction coefficient is the more appropriate spectral averaging to calculate the emission from a surface to a free space.

The Rosseland extinction coefficient is defined as [42][10]:

$$\frac{1}{\beta_R(T)} = \int_{\lambda=0}^{\infty} \left(\frac{1}{\beta_\lambda}\right)\left(\frac{\partial E_{\lambda b}}{\partial E_b}\right) d\lambda = \frac{\pi}{2}\frac{C_1 C_2}{\sigma T^5}\int_{\lambda=0}^{\infty}\left(\frac{1}{\beta_\lambda}\right)\left(\frac{\exp\left(\frac{C_2}{\lambda T}\right)}{\lambda^6\left[\exp\left(\frac{C_2}{\lambda T}\right)-1\right]^2}\right)d\lambda \qquad (4.13)$$

Where $\partial E_{\lambda b}$ and ∂E_b are blackbody spectral emissive power and blackbody total emissive power, T is temperature, $C_1 = 0.595522 \times 10^{-16}\, W.m^2/sr$ and $C_2 = 0.01438777\, m.K$. The $\partial E_{\lambda b}/\partial E_b$ is found by differentiating Planck's law after substituting $T = (E_b/\sigma)^{1/4}$.

The Planck mean extinction coefficient is weighted by the blackbody emission spectrum and can be expressed as [42][10]:

$$\beta_P(T) = \frac{\int_{\lambda=0}^{\infty}\beta_\lambda E_{\lambda b}(T)d\lambda}{\int_{\lambda=0}^{\infty}E_{\lambda b}(T)d\lambda} = \frac{\int_{\lambda=0}^{\infty}\beta_\lambda E_{\lambda b}(T)d\lambda}{\sigma T^4} \qquad (4.14)$$

where $E_{\lambda b}$ can be determined by [42]:

$$E_{\lambda b} = \frac{2\pi C_1}{\lambda^5 \left[\exp\left(\frac{C_2}{\lambda T}\right) - 1 \right]} \tag{4.15}$$

Rosseland and Planck mean extinction coefficients as a function of temperature have been calculated for all materials and are shown in figure 4.7. For metals (figure 4.7 (a)), the results of Rosseland mean extinction coefficient is close to that of Planck mean extinction coefficient for low temperature. However, the values of Planck mean are higher at high temperatures. The reason is that metals have a larger optical thickness at high temperatures since their spectral extinction coefficients are high at shorter wavelengths where blackbody emissive power is high. Therefore, the results of Rosseland mean can be more trustful at higher temperatures. For oxides that have a roughly spectrally flat profile of β_λ over all wavelengths, there is a good agreement between the results of Rosseland extinction coefficient and that of Planck mean extinction coefficient (as shown in figure 4.7 (b)). On the contrary, the spectral extinction coefficient of TiO_2, SiO_2, and Y_2O_3 varies sufficiently with wavelength. Hence, the results of Rosseland and Planck mean extinction coefficients are quite different. To obtain a mean extinction coefficient for materials that are optically thick in some wavelengths and optically thin in other regions, one approach is applying a Rosseland mean over the optically thick regions of spectrum and a Planck mean over the optically thin portions [79]. For $BaTiO_3$, Si_3N_4, AlON, and Clays, Rosseland mean extinction coefficients don’t agree with the Planck mean results. As it was shown before, clays have a large extinction coefficient in wavelengths 3-10 [μm] and a low extinction coefficient at shorter wavelength 0.5-3 [μm] which is the reason of disagreement. However, there is good agreement for the other materials in the group of other compounds. Figure 4.7, in general, indicates that some materials such as Fe_3O_4, ZrO_2, ZnO, Al_2O_3, $LaFeO_3$, $LaMnO_3$, and some rare metals like Dysprosium and Erbium have a high mean extinction coefficient over the whole range of temperature. Among them, oxides and perovskites are good options to use as opacifying particles inside the insulation since they are stable at high temperatures.

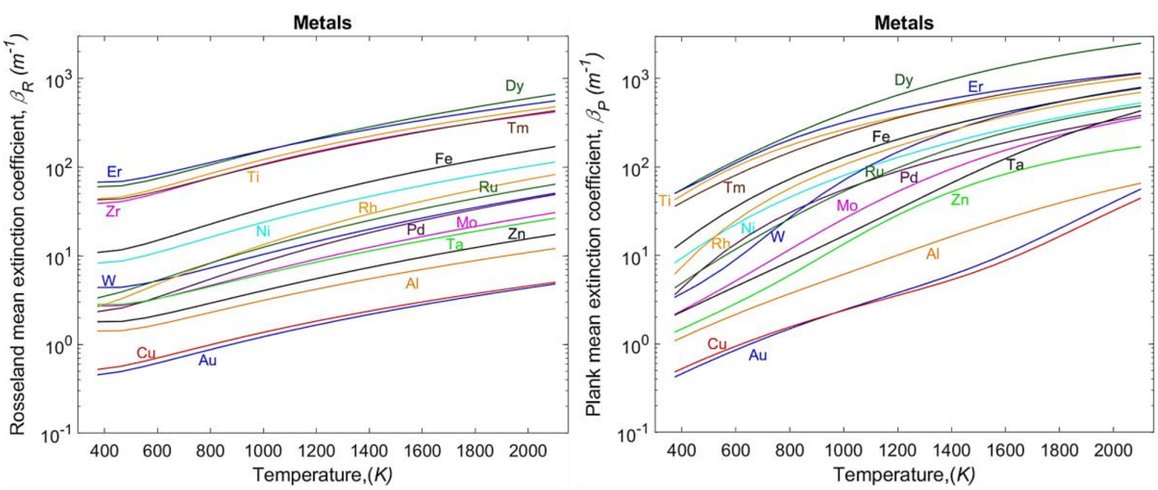

a

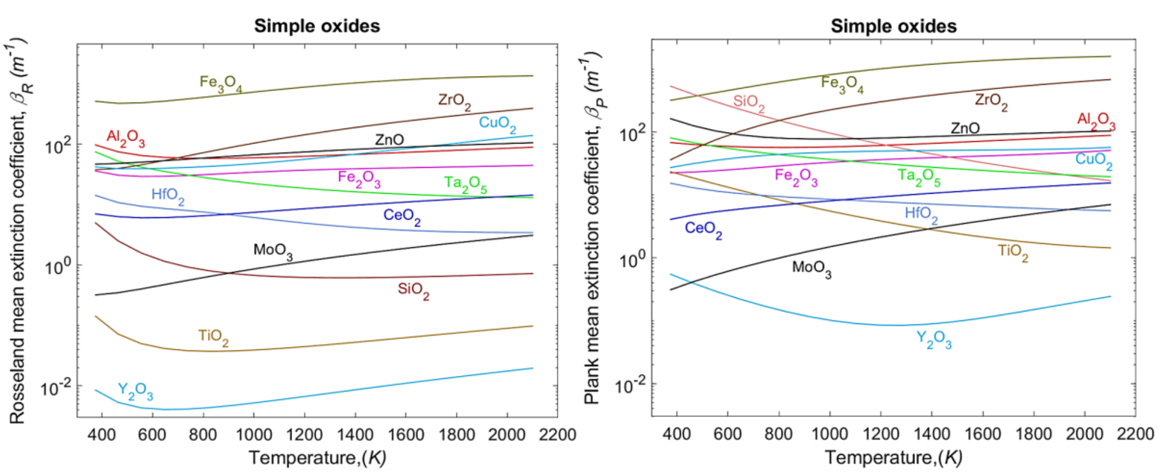

b

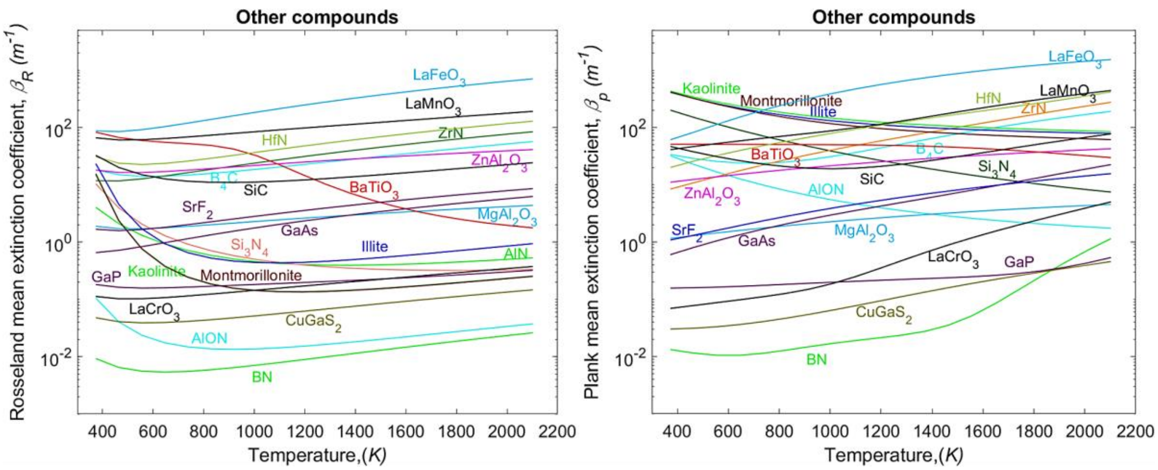

c

Figure 4.7. Rosseland mean and Planck mean extinction coefficients of materials as a function of temperature.

At this point, the performance of different groups of materials as opacifier particles inside the volumetric extinction design was investigated. It was revealed that the ability of materials for attenuating the radiation strongly depends on their complex index of refraction under the same physical properties and conditions. Refractive index and absorptive index of representative materials were exported form the literature to use in the model in or order to identify the most well performing materials. It was shown that the performance of materials to suppress radiation strongly depends on their refractive index and absorptive index. In fact, the shape of the complex refractive index curve for a material depends on the different absorption lines and bands within a material. It was seen that some materials are performing better than others to attenuate radiation due to some effects such as their absorption lines and bands in the spectrum range. These are a complex function of the electronic and vibrational structure of the material. To capture the main effects, we can consider a simple harmonic oscillator model. In the present work, Lorentz model is used to calculate the frequency dependence of real and imaginary parts of the complex dielectric constant. Then, the complex dielectric constant of a medium can be related to its complex refractive index to evaluate the opacifying performance.

4.4 Lorentz oscillator model

The Lorentz oscillator model is a model that considers atoms as oscillating electric dipoles which emit and absorb electromagnetic waves at discrete frequencies. To provide a simple explanation for the Lorentz oscillator model, we consider the case of a bound electron that is connected to the nucleus with a hypothetical spring representing a restoring force (shown in Figure 4.8). Since the nucleus has a heavy mass compared to the electron, we assume that it stays stationery, whereas, the electron oscillates back and forth at the resonant frequency (ω_0) creating an electric dipole which varies with the time. Figure 4.8 demonstrates the connection between the time varying displacement of the electron ($x(t)$) from its equilibrium position and the diploe ($p(t)$) [80]. The dipole model can be used to understand the behaviour of the atom when an external electromagnetic wave at frequency ω hits it. The external wave applies forces to the atom and drives the oscillations. If the frequency of the external wave, ω, coincides with any of the resonant frequencies of the atom, ω_0, the resonance phenomenon happens and the energy of the wave will be absorbed and re-emitted by the atom. If ω does not coincide with any ω_0 of the atom, the medium shows a transparent behaviour without having absorption. However, the velocity of the wave decreases as a result of multiple scattering process.

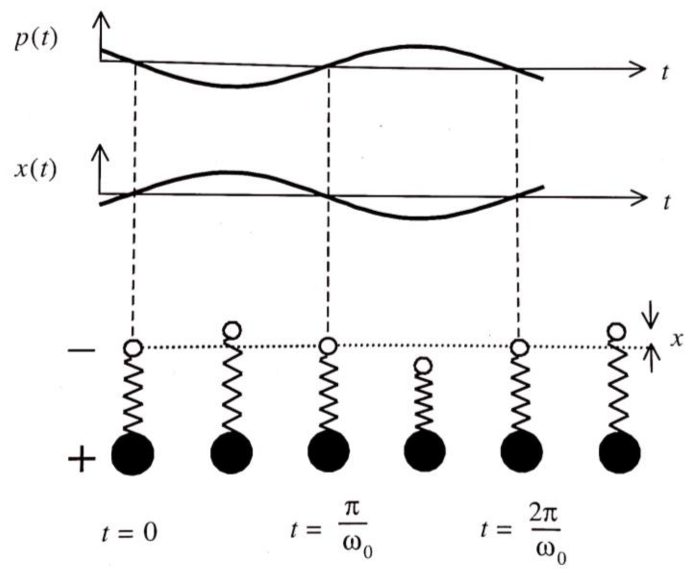

Figure 4.8. An oscillating dipole (atom) comprising a heavy positive charge (nucleus) connected to a light negative charge (bound electron) [80].

The general explanation of dipole oscillator model was given and now we want to determine the refractive index and absorptive index as a function of frequency by using the model. To do this, first we calculate the frequency dependence of complex dielectric constant.

The Lorentz model expresses the complex dielectric constant as [80]:

$$\bar{\epsilon_r}(\omega) = 1 + \chi + \frac{\omega_P^2}{(\omega_0^2 - \omega^2 - i\gamma\omega)} \tag{4.16}$$

where γ, ω_p and χ are the damping rate, plasma frequency and the electric susceptibility, respectively. The concept of damping term (γ) is a result of the fact that the energy of the oscillating electric dipoles lowers by collisional processes. The electric susceptibility (χ)

is another important term in the Lorentz model. If we apply an electric field to a material, the electrons will be displaced, producing several dipoles. The electric susceptibility is a non-dimensional parameter that states the magnitude of polarization in case of applying an electric field. The higher electric susceptibility of materials, the more displacement of electrons and the higher ability of polarization. The plasma frequency is the frequency of oscillation of electron-ion in the plasma which is a natural gas of heavy ions and light electrons.

We can split the complex dielectric constant into the real part ($\epsilon_1(\omega)$), and the imaginary part ($\epsilon_2(\omega)$) to obtain [80]:

$$\epsilon_1(\omega) = 1 + \chi + \frac{\omega_P^2(\omega_0^2 - \omega^2)}{(\omega_0^2 - \omega^2)^2 + \omega^2\gamma^2} \tag{4.17}$$

$$\epsilon_2(\omega) = 1 + \chi + \frac{\omega_P^2\gamma\omega}{(\omega_0^2 - \omega^2)^2 + \omega^2\gamma^2} \tag{4.18}$$

The complex dielectric constant of a medium can be connected to its complex refraction index according to:

$$\bar{n} = \sqrt{\bar{\epsilon_r}} \tag{4.19}$$

Then, the real and imaginary parts of complex refraction index can be calculated through [80]:

$$n = \frac{1}{\sqrt{2}}(\epsilon_1 + (\epsilon_1^2 + \epsilon_2^2)^{\frac{1}{2}})^{\frac{1}{2}} \tag{4.20}$$

$$k = \frac{1}{\sqrt{2}}(-\epsilon_1 + (\epsilon_1^2 + \epsilon_2^2)^{\frac{1}{2}})^{\frac{1}{2}} \tag{4.21}$$

Which shows that if we know the real and imaginary parts of dielectric constant, we can obtain the real and imaginary parts of complex refraction index.

Figure 4.9 [80] helps us to have a general understanding about the typical shape of ϵ_1 and ϵ_2 as a function of angular frequency (due to equations 4.17 and 4.18) and shows the reaction of a dipole oscillator at frequencies close to resonance. In this example, the dipole oscillator has $\omega_0 = 100\,THz$, $\chi = 9$, $\omega_P = 145\,THz$, $\gamma = 5\,THz$. ϵ_{st} and ϵ_∞ represent the low and high limits of $\epsilon_r(\omega)$ and are defined as:

$$\bar{\epsilon_r}(\omega = 0) \equiv \epsilon_{\mathrm{st}} = 1 + \chi + \frac{\omega_P^2}{\omega_0^2} \tag{4.22}$$

$$\bar{\epsilon_r}(\omega = \infty) \equiv \epsilon_\infty = 1 + \chi \tag{4.23}$$

The subscript "st" stands for "static".

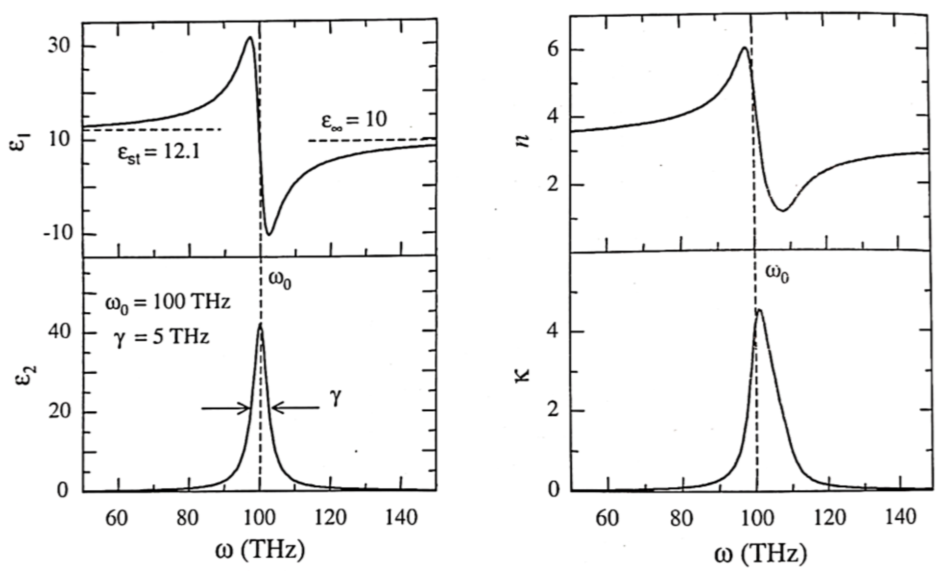

Figure 4.9. The real and imaginary parts of complex dielectric constant as a function of frequency [80].

Figure 4.9 demonstrates the frequency dependence of the real and imaginary parts of dielectric constant. As can be seen, ϵ_2 has a strong peak centered at the resonance frequency, and γ represents the absorption width of frequency at $\epsilon_2 = \epsilon_{2,\max}/2$. For ϵ_1 curve, it increases from the low frequency limit of ϵ_{st}, hitting a maximum value at $\omega = \omega_0 - \gamma/2$. It then drops suddenly and reaches its minimum value at $\omega = \omega_0 + \gamma/2$. Finally, it increases again to reach the high frequency value of ϵ_∞ [80].

In this section, the approach is to change the four effective variables of ω_0, ω_P, γ and χ, to predict how they affect the complex index of refraction in order to reach the desirable n and k. For this purpose, we have selected four different typical values for each variable. There are four steps and in each step, we kept three variables constant and changed one variable to investigate the influence of that variable on n and k. As our interest range of wavelength is 0.5-10 [μm], we consider the corresponded angular frequency that is in range $1.88 \times 10^{14} - 37.7 \times 10^{14}$ $[rad/s]$ ($\omega = 2\pi c_0/n\lambda$, where c_0 is speed of light in vacuum and n is the refractive index of the medium).

- **Step 1: Investigating the influence of $\boldsymbol{\omega_0}$ on $\boldsymbol{n}$ and $\boldsymbol{k}$**

To investigate the influence of ω_0 on the behavior of n and k, we kept γ, ω_P and χ fixed and changed ω_0. All selected values of ω_0 are in the range of angular frequency $1.88 \times 10^{14} - 37.7 \times 10^{14}$ $[rad/s]$. The selected values and the results are shown in figure 4.10. As it shows, increasing the resonant frequency from 5×10^{14} $[rad/s]$ to

28×10^{14} $[rad/s]$ not only decreases the peak values of n and k significantly but also lowers the values of n before the peak. Moreover, the lower resonant frequency, the lager range of frequency in which the n and k fluctuate. In the view of the extinction coefficient map plot, increasing ω_0 shrinks the curve of k vs n and shifts the right side of the curve towards down.

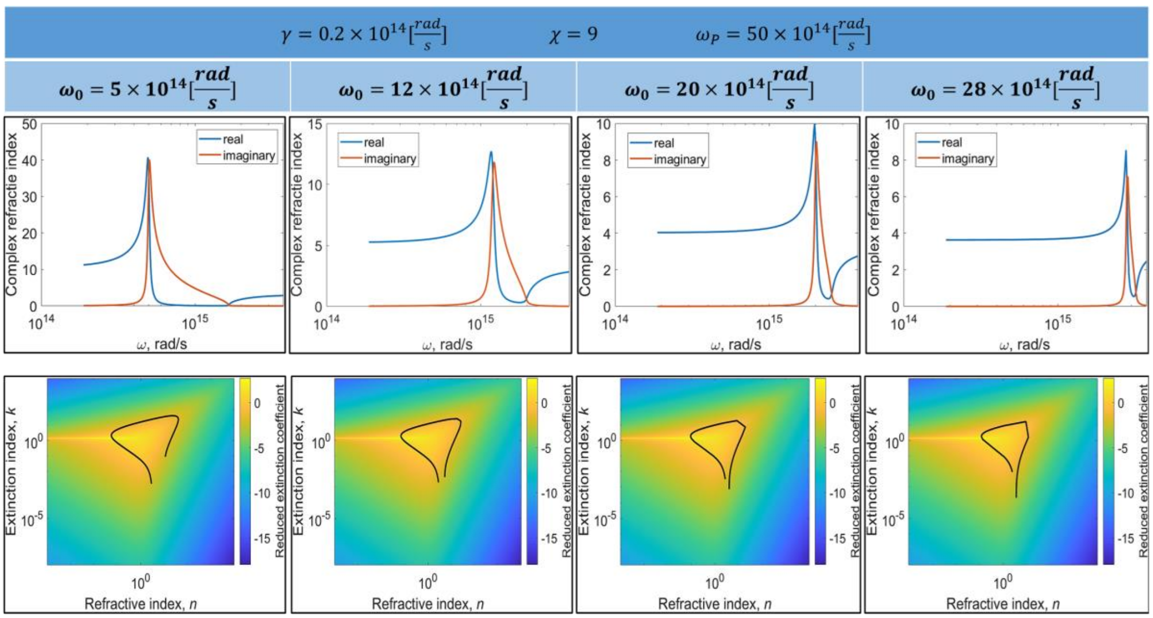

Figure 4.10. Effect of resonant frequency on the behavior of n and k.

- **Step 2: Investigating the influence of γ on n and k**

To assess the effect of γ on the behavior of n and k, we kept ω_0, ω_P and χ fixed and changed γ. To have fairly typical values of the damping rate γ, we have selected four values of $\gamma = [0.03\omega_0, 0.05\omega_0, 0.07\omega_0, 0.1\omega_0]$. Figure 4.11 demonstrates the selected numbers of parameters and their results. It can be seen that an increase in the damping term results in decreasing the peak of n and k as a function of frequency, and also broadening their lines which agrees with the explanations in [80]. In terms of color map, enhancing γ contracts the curve of k vs n towards its center keeping the overall shape unchanged.

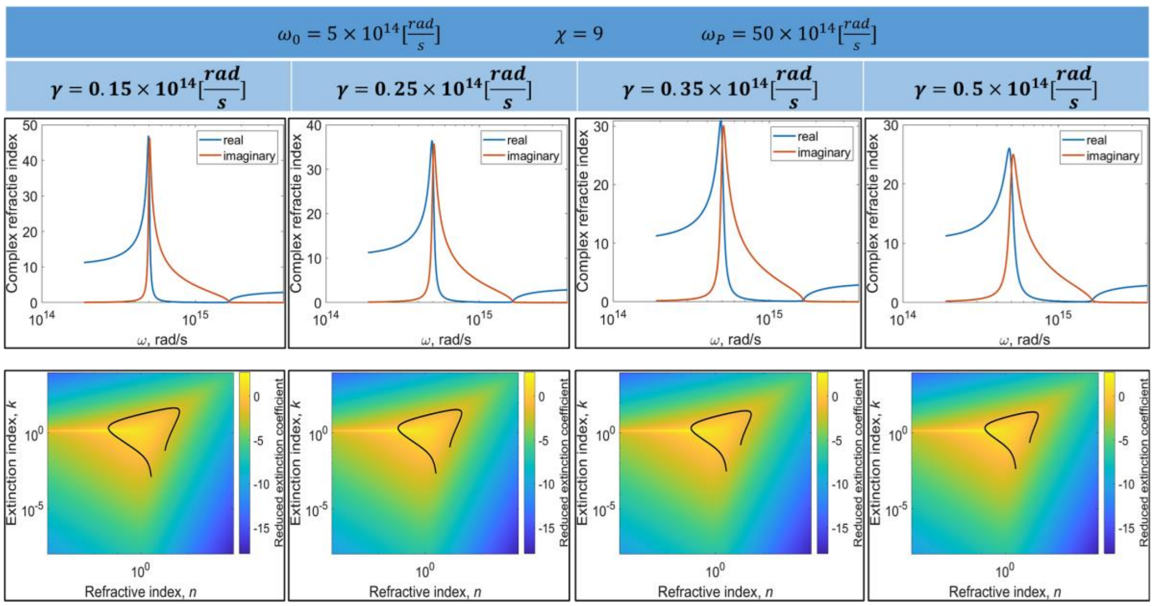

Figure 4.11. Effect of damping term on the behavior of n and k.

- **Step 3: Investigating the influence of χ on n and k**

To study the influence of χ on the behavior of n and k, we maintained γ, ω_P and ω_0 constant and changed χ. The selected numbers are tabulated in the figure 4.12 as well as the results. The results indicate that increasing the electric susceptibility lowers the range of frequency in which the n and k fluctuate. However, χ affects the behavior of n and k only after their peaks and doesn't make any change before their peaks. In addition, the peaks values remain unchanged with changing the electric susceptibility. Regarding the surface plot, enhancing χ shifts the left side of the k-n curve towards the light and down, while keeping the right side of the curve unaffected.

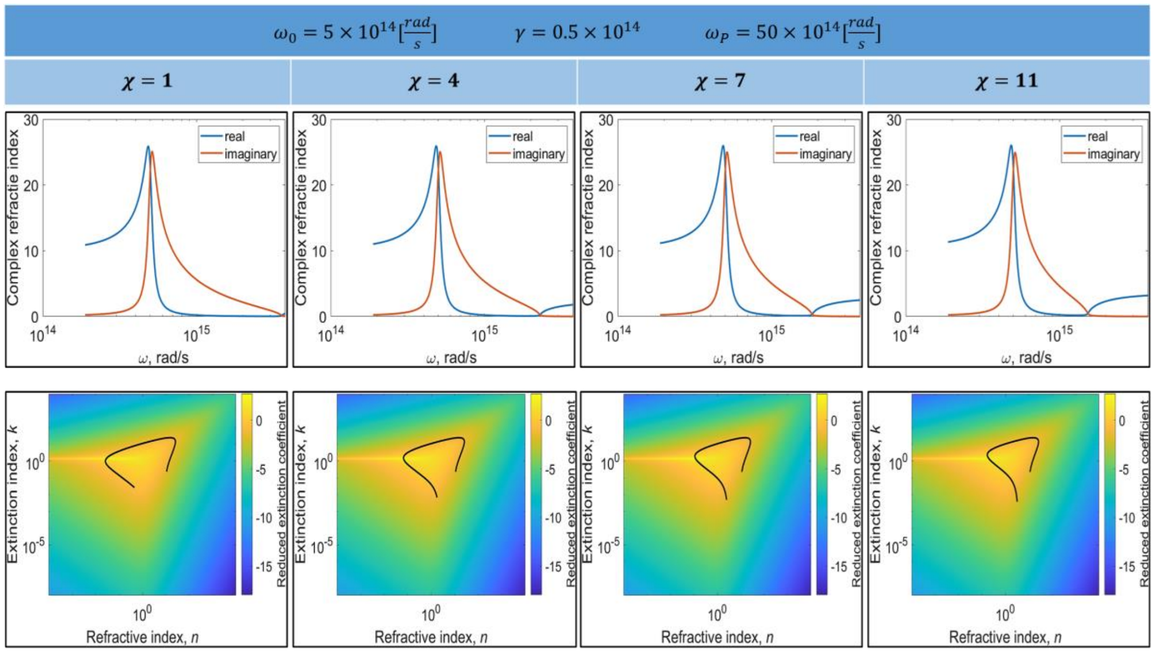

Figure 4.12. Effect of electric susceptibility on the behavior of n and k.

- **Step 4: Investigating the influence of $\boldsymbol{\omega_P}$ on $\boldsymbol{n}$ and $\boldsymbol{k}$**

To investigate the influence of ω_P on the behavior of n and k, we changed ω_P by keeping γ, ω_0 and χ constant. As shown in figure 4.13, the complex refractive indices increase and peak at higher values with increasing the plasma frequency. In addition, the larger plasma frequency, the wider fluctuation frequency toward the higher values. According to the reduced extinction coefficient plot, increasing ω_P broadens the left side of the k-n curve and shifts slightly the whole curve towards the right-up.

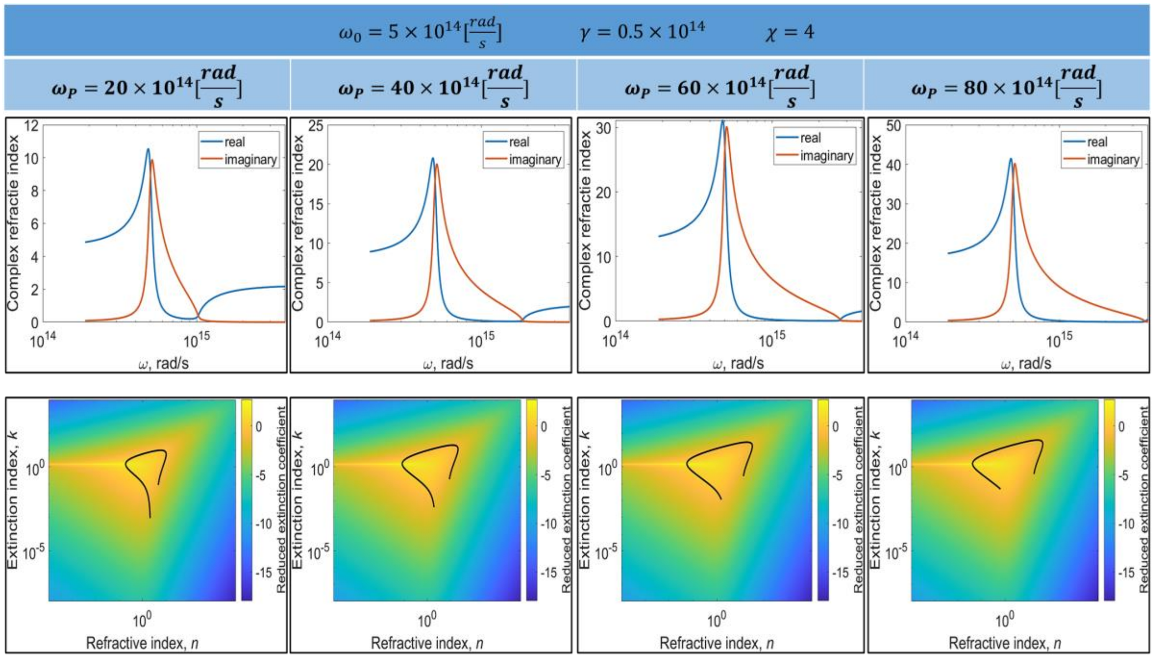

Figure 4.13. Effect of plasma frequency on the behavior of n and k.

4.5 Application of the theory to the volumetric extinction design

Previously, the radiative heat transfer phenomenon through the volumetric design was described and it was revealed that the extinction coefficient of the medium must increase to lower the radiative heat transfer through the medium. Based on the Rayleigh theory, a model was built to describe the opacifying performance of several materials as dispersed particles throughout the insulation medium and it was shown that some materials have a better attenuating performance compared to others. Therefore, the Lorentz oscillator model was used to capture the main effects on the opacifying performance of materials. In this section, we will explain how to apply the theory to the volumetric design and will calculate the performance of two representative materials, as dispersed particles inside the main medium for suppressing the radiation. Similar to our approach in Section 3.3, we set a goal which is coming up with an insulation design that has an effective thermal conductivity lower than 0.08 $[\mathrm{W\,m^{-1}K^{-1}}]$ at temperature $T = 1273$ [K]. By applying the theory presented in the previous sections, we study the performance of two representative materials, Fe_3O_4 and SiO_2. For each material, we calculated the amount of volume fraction that is needed to reach $k_{\mathrm{eff}} \leq 0.08$ $[\mathrm{Wm^{-1}K^{-1}}]$.

In Section 3.3, we saw that if we assume that the thickness of the insulation is 10 [cm] and one side of it is exposed to a high temperature of $T_2 = 1273$ [K], and the other side is at the room temperature ($T_1 = 298$ [K]), then the effective emissivity has to be lower than 0.0053 to reach $k_{\mathrm{eff}} \leq 0.08$ $[\mathrm{Wm^{-1}K^{-1}}]$.

To calculate the amount of volume fraction that is needed to reach $\varepsilon_{\mathrm{eff}} = 0.0053$, first the needed amount of the Rosseland mean extinction coefficient must be determined. As mentioned before, Rosseland mean extinction coefficient is a local property which changes through the thickness of insulation since the temperature changes. However, we assume that the value of Rosseland mean extinction coefficient is not changing much through the thickness and considering Equation 4.1, we can define the effective emissivity of the volumetric design as:

$$\varepsilon_{\mathrm{eff}} = \frac{1}{\frac{3}{4}\beta_{\mathrm{R}}L + \frac{1}{\varepsilon_1} + \frac{1}{\varepsilon_2} - 1} \tag{4.24}$$

If we assume that the optically thick insulation medium is paced between two gray diffuse plates with emissivity of 0.5, we can calculate the Rosseland mean extinction coefficient as:

$$\beta_{\mathrm{R}} = \frac{\frac{1}{\varepsilon_{\mathrm{eff}}} - \frac{1}{\varepsilon_1} - \frac{1}{\varepsilon_2} + 1}{\frac{3}{4}L} = \frac{\frac{1}{0.0053} - \frac{1}{0.5} - \frac{1}{0.5} + 1}{0.75 \times 0.1} = 2.475 \times 10^3 \ [m^{-1}]$$

Therefore, the Rosseland mean extinction coefficient of the insulation must be higher than 2.475×10^3 [m^{-1}] to obtain $k_{\mathrm{eff}} \leq 0.08$ [$\mathrm{Wm}^{-1}\mathrm{K}^{-1}$]. Now we calculate the amount of volume fraction that is needed if we use the dispersed particles of Fe_3O_4 or SiO_2 throughout the host medium (is assumed to be vacuum or air). Figure 4.6 shows the Rosseland mean extinction coefficient of some oxides as a function of temperature which is calculated for a volume fraction of 0.1%. As mentioned, the Rosseland mean extinction coefficient is a local property and its value changes over the thickness as the gradients change. Therefore, we pick an average representative value of Rosseland extinction coefficient which is approximately 903.09 and 1.05 [m^{-1}] for Fe_3O_4 and SiO_2, respectively. These values are calculated for a volume fraction of 0.1%, and since the volume fraction is a constant value (not a function of wavelength and temperature), we can calculate volume fraction of each material to reach $\beta_{\mathrm{R}} \geq 2.475 \times 10^3$ [m^{-1}] simply as:

$$f_{v,\mathrm{Fe_3O_4}} = \frac{2.475 \times 10^3 \times 0.001}{903.09} = 0.0027 = 0.27\%$$

$$f_{v,\mathrm{SiO_2}} = \frac{2.475 \times 10^3 \times 0.001}{1.05} = 2.3571 \simeq 237\%$$

According to Figure 4.2, embedding Fe_3O_4 particles with the volume fraction of 0.27% and size parameter of lower than 0.1 into the host medium is quite applicable to still remain at the region of independent scattering. Whereas, loading SiO_2 particles with the volume fraction of 236% and size parameter of lower than 0.1 would violate the independent scattering assumption in the Rayleigh theory. Therefore, it can be concluded that it is not applicable to make an insulation material having effective thermal conductivity of 0.08 $[\mathrm{Wm^{-1}K^{-1}}]$ which is made of SiO_2 with the volume fraction of 236%. The results are summarized in Table 4.2.

Table 4.2. The volume fraction of particles needed in a slab of insulation with thickness of 10 [cm] to reach $\boldsymbol{k}_{\mathbf{eff}} \leq [\mathbf{Wm^{-1}K^{-1}}]$ at T=1273 [K].

Material	Particles volume fraction
Fe_3O_4	0.27 %
SiO_2	236 %

We can use the oscillator Lorentz model to evaluate the radiation extinction performance of SiO_2 and to introduce a new hypothetical material that shows a better opacifying behaviour compared to SiO_2. The approach is to change the Lorentz oscillator parameters of SiO_2 ($\omega_0, \omega_p, \gamma$ or χ) to reach a higher Rosseland mean extinction coefficient. First, we need to define the Lorentz oscillator parameters of SiO_2. To do this, we considered the complex refractive index of SiO_2 as a function of wavelength and by trial and error we tried to find $\omega_0, \omega_p, \gamma$ and χ in order to reach the same n and k using Equations 4.17-4.21. It was found that the Lorentz oscillator parameters of $\omega_0 = 2.069\ \times 10^{14}$ [rad $\mathrm{s^{-1}}$], $\omega_p = 1.45\ \times 10^{14}$ [rad $\mathrm{s^{-1}}$], $\gamma = 1\ \times 10^{13}$ [rad $\mathrm{s^{-1}}$] and $\chi = 1$ would give almost the same n

and k as SiO_2 as demonstrated in Figure 4.14. This figure shows that Lorentz model was able to model the complex refractive index of SiO_2 successfully. Even though Lorentz oscillator model is not the most accurate method to model the optical properties of materials, it helps us to develop a general trend for materials which is close to their actual optical trend (as what we did for SiO_2 for example). Therefore, it can be said that the accuracy of Lorentz model is enough to capture the materials optical properties in our work and other accurate detailed models might not be needed.

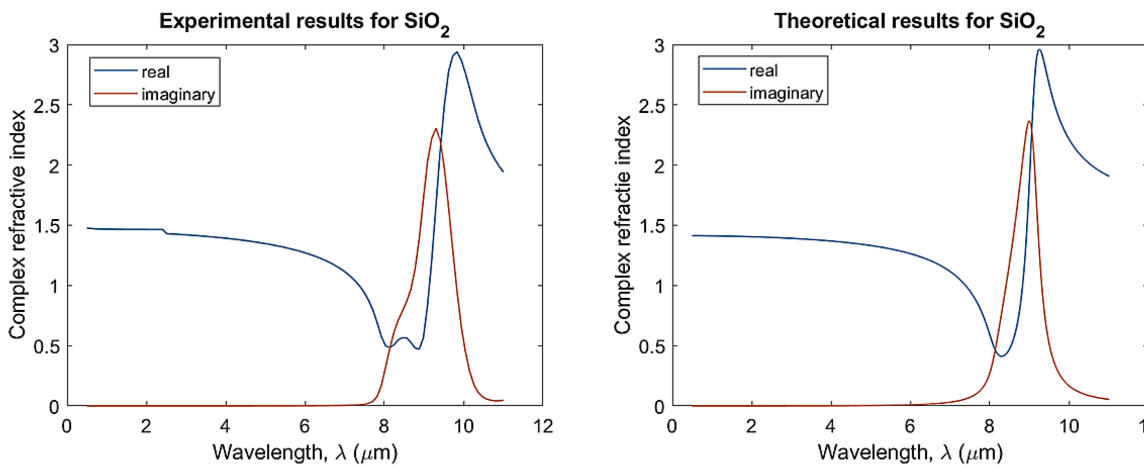

Figure 4.14. Complex refractive index of SiO_2 as a function of wavelength calculated by experiments [53] and Lorentz model.

Now by knowing the Lorentz oscillator parameters of SiO_2, we can try to reach a desirable n and k by changing the Lorentz oscillator parameters. The goal is to find a hypothetical material having a higher Rosseland extinction coefficient. Based on the investigation in section 4.4, we know that increasing ω_P broadens the curve of k-n towards the right-up. We can use this result to move the initial curve of SiO_2 towards the high extinction region. Figure 4.15. (a) shows the actual k-n curve of SiO_2 with the

Lorentz oscillator parameters of $\omega_0 = 2.069 \times 10^{14}$ [rad s^{-1}], $\omega_p = 1.45 \times 10^{14}$ [rad s^{-1}], $\gamma = 1 \times 10^{13}$ [rad s^{-1}] and $\chi = 1$. Figures 4.15 indicates that increasing the plasma frequency from 1.45×10^{14} [rad s^{-1}] (Figure 4.15. (a)) to 13×10^{14} [rad s^{-1}] (Figure 4.15. (d)) enhances the Rosseland extinction coefficient more than 10% from 0.57 [m^{-1}] to 59.97 [m^{-1}]. It should be mentioned that the Rosseland extinction coefficient is calculated at $T = 1273$ [K]. To increase β_{R} more, we can change ω_0 and γ. In section 4.4, it was seen that increasing ω_0 and γ shrinks the curve towards the center. This is in the favour in this case since the curve of k-n in Figure 4.15. (d) is located around the maximum region and increasing ω_0 and γ shrinks the curve and moves it towards the high region of extinction coefficient. Figure 4.16 demonstrates that increasing ω_0 and γ from 2.069×10^{14} [rad s^{-1}] and 1×10^{13} [rad s^{-1}] (Figure 4.16. (a)) to 5×10^{14} [rad s^{-1}] and 5×10^{13} [rad s^{-1}] (Figure 4.16. (d)), respectively, will enhance β_{R} from 59.97 [m^{-1}] to 188.13 [m^{-1}]. Finally, Figure 4.17 shows that if we decrease χ from 1 to 0, β_{R} increases from 188.13 [m^{-1}] to 234.10 [m^{-1}]. Whereas, increasing χ from 1 to 3 results in decreasing β_{R} from 188.13 [m^{-1}] to 116.97 [m^{-1}]. The reason is that enhancing χ shifts the left side of the k-n curve towards down, moving it away from the high region zone in the color map.

Therefore, we can conclude that a material with having $\omega_0 = 5 \times 10^{14}$ [rad s^{-1}], $\omega_p = 13 \times 10^{14}$ [rad s^{-1}], $\gamma = 5 \times 10^{13}$ [rad s^{-1}] and $\chi = 0$, performs strongly better than SiO_2 to extinct the radiation as the Rosseland extinction coefficient enhances from 0.57 $[\mathrm{m}^{-1}]$ to 234.10 $[\mathrm{m}^{-1}]$.

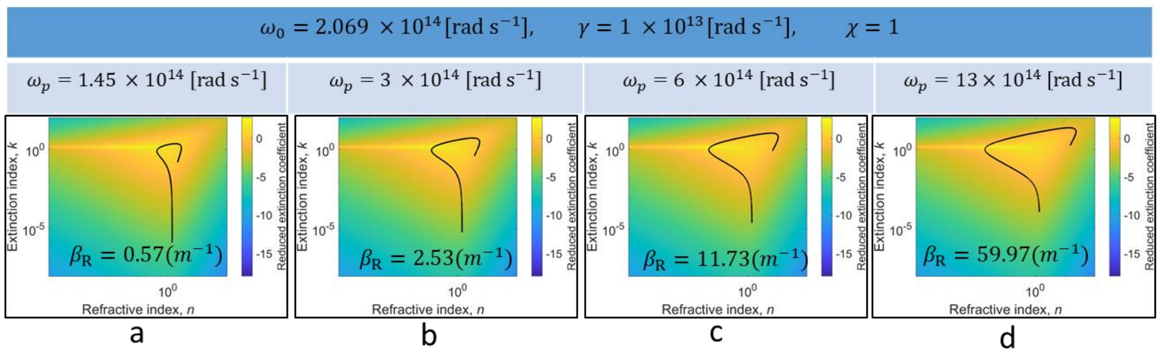

Figure 4.15. Influence of $\boldsymbol{\omega_p}$ on the opacifying behavior of the material.

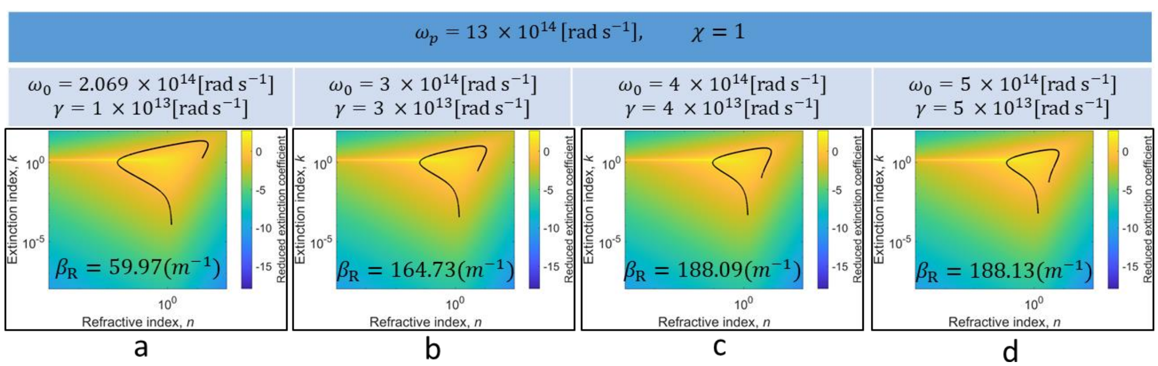

Figure 4.16. Influence of $\boldsymbol{\omega_0}$ and γ on the opacifying behavior of the material.

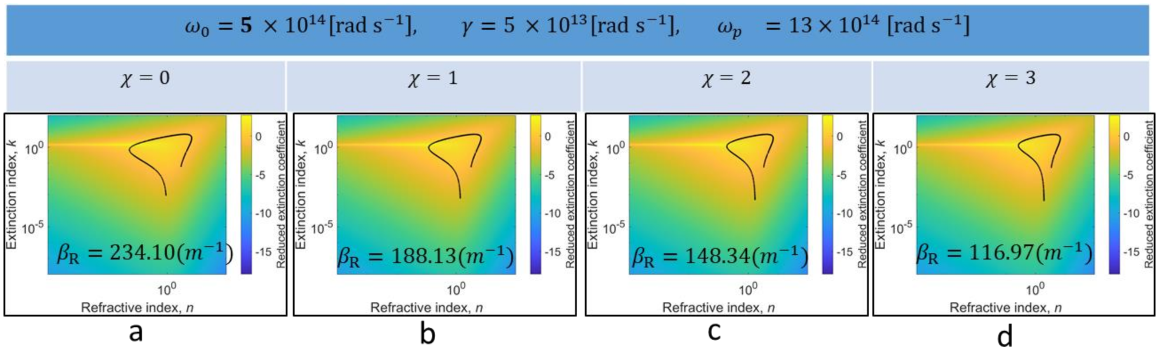

Figure 4.17. Influence of χ on the opacifying behavior of the material.

Chapter 5
Conclusion

Thermal insulation, for many years, has attracted many interests due to its vast demand in many various industries. The main function of thermal insulation is reducing the heat transfer rate significantly between the system and the ambient or between two regions of a system. Many systems, nowadays, operate at higher temperatures (above 1000 [℃]). Current thermal insulation materials have either a low service temperature, lower than 1000 [℃] or a poor thermal performance with thermal conductivities higher than 0.3 [$\mathrm{Wm^{-1}k^{-1}}$] at high temperatures Therefore, there is a strong need for developing an advanced high temperature thermal insulation design that withstands high temperatures and have a low thermal conductivity, lower than 0.1 [$\mathrm{Wm^{-1}k^{-1}}$], at such high temperatures. According to this gap, the present thesis focused on developing a materials-focused pathway to improve the performance of high temperature thermal insulation by suppression radiative transport since radiation dominates over conduction and convection at high temperatures. For this purpose, two thermal insulation deigns were considered; “Multilayered Shielding Design” and “Volumetric Extinction Design”. First, the performance of multilayered insulation design comprising highly reflective shields and low thermal conductive spacers was investigated. The investigation showed that using radiative shields having the highest reflectivity would result in the lowest radiative heat transfer. To come up with high performance materials with having a high ability to reflect the radiation, a novel methodology was created to evaluate the performance of any types of material as shields by describing the connection between the reflection of the radiation and the optical properties of the surface. In our methodology, a surface plot of hemispherical reflectivity as a function of refractive index (n) and absorptive index (k) was used in order to evaluate the performance of different materials. For various representative materials, a curve of k as a function of n was plotted and merged with the hemispherical reflectivity map to see where each curve lies in the hemispherical reflectivity plot. The results showed that metals have a much higher reflectivity compared to the non-metals such as oxides, clays, nitrides or other compounds. The performance of two metals (Al and Cu) and their oxides (Al_2O_3 and Cu_2O) were investigated as shields through an example of insulation structure. The results showed that implanting 1 and 3 shields of Cu and Al, respectively, inside the insulation medium could lower thermal conductivity to 0.08 [$\mathrm{W\ m^{-1}\ K^{-1}}$]. However, Al and Cu turn into Al_2O_3 and Cu_2O at high temperatures. Due to the results, 154 and 125 shields of Al_2O_3 and Cu_2O, respectively, were needed to reach the same thermal conductivity which indicates the practical challenge with metals in high temperature MLI designs. As a conclusion, MLI works best with metals that have the highest reflectivity to minimize the radiative losses. However, using them as highly reflective shields in the MLI design have two main limits at high temperatures. The first limit is that most of the metals have melting temperature lower than 2000 [K] which disqualifies them for using in the ultra-high temperature applications. The second and the most important limit with respect to metals is that they will oxidize at high temperatures which will result in a significant decrease in their reflectivity. Accordingly, the MLI design is fated to be either inappropriate or insufficient at high temperatures.

Then, the present work considered the volumetric extinction design as an alternative option for high temperatures. Volumetric approach utilizes radiatively participating (absorbing/scattering) particles dispersed throughout a low conductivity host medium to suppress the radiation. Based on the Rayleigh theory, a novel methodology was built to assess the performance of volumetric design to suppress the radiation with material perspective. The aim was to maximize the extinction coefficient of the design in order to minimize the radiative losses. Due to the Rayleigh theory, the reduced form of the extinction coefficient was introduced which was only a function of refractive index and absorptive index. Then, the surface plot of reduced extinction coefficient as a function of n and k was used to evaluate the performance of some materials for attenuating the radiation. For various representative materials, a curve of k as a function of n was plotted and merged with the reduced spectral extinction coefficient map to see where the curve of each material lies. Further, the influence of wavelength on the extinction coefficient of materials was investigated along with the blackbody spectral hemispherical emissive power and the Rosseland function curves for high temperatures. Rosseland mean extinction coefficient and Planck mean extinction coefficient were used to evaluate the total extinction coefficient of materials for the entire range of wavelengths. The results showed that unlike the MLI design that was shown to work best with metals, there are many non-metal materials that exhibit a very effective performance for attenuating the radiation, yet withstand high temperatures. Among the investigated materials some oxides such as Fe_3O_4, clays, and some perovskites such as $LaFeO_3$ showed a good performance. In an example of volumetric structure, the opacifying performance of Fe_3O_4 and SiO_2 as participating particles were compared. The results showed that implanting Fe_3O_4 particles inside the insulation medium with volume fraction of around 0.27% would result in a Rosseland extinction coefficient of 2.475×10^3 $[\mathrm{m}^{-1}]$, hence a thermal conductivity of 0.08 $[\mathrm{Wm}^{-1}\mathrm{K}^{-1}]$. While, more than 273% volume fraction of SiO_2 was needed to reach the same result, which indicates the excellence performance of Fe_3O_4 compared to SiO_2 to extinct radiation. In another attempt, the Lorentz oscillator model was used to capture the main effects on the opacifying performance of materials. The approach was to investigate the influence of ω_0, ω_P, γ and χ, on the shape of k vs n curves in the surface plot of reduced extinction coefficient. At the end, the complex refractive index of SiO_2 was modeled by Lorentz oscillator model. By investigating the influence of ω_0, ω_P, γ and χ, on the opacifying behaviour of SiO_2, we could introduce a hypothetical material having a Rosseland extinction coefficient of 234.10 $[\mathrm{m}^{-1}]$, while this value was 0.57 $[\mathrm{m}^{-1}]$ for SiO_2.

For the future work, the first important next step is to validate the theoretical results through an experimental approach. For MLI and volumetric designs individually, an experimental methodology has been initially developed to validate the theoretical findings. However, the experimental steps were not completed due to the COVID-19 conditions. In our theoretical methodology, we investigated materials due to their data of complex refractive index exported from the literature. The data are related to the bulk materials, however in the volumetric design we consider materials as particles inside the medium. Therefore, it is important to compare the optical properties of materials in the bulk state with the particle stat. Another important point regarding materials is that the exported data of complex refractive index of materials were related to the room temperature. Therefore, it is important to check if their complex refractive index keeps constant at high temperature.

Regarding the materials theoretical investigation, the presented methodology for each design could be a roadmap to investigate more materials in the future.

References

[1] W. Villasmil, L. J. Fischer, and J. Worlitschek, "A review and evaluation of thermal insulation materials and methods for thermal energy storage systems," *Renewable and Sustainable Energy Reviews*, vol. 103. Elsevier Ltd, pp. 71–84, Apr. 01, 2019, doi: 10.1016/j.rser.2018.12.040.

[2] G. Deshmukh, P. Birwal, R. Datir, S. Patel, and others, "Thermal insulation materials: A tool for energy conservation," *J. Food Process. \& Technol.*, vol. 8, no. 04, pp. 1–5, 2017.

[3] P. Kreider and W. Lipiński, "High-temperature gas--solid reactions in industrial processes," *Rev. Mineral. Geochemistry*, vol. 84, no. 1, pp. 499–514, 2018.

[4] B. M. A. Abdel-Banat, H. Hoshida, A. Ano, S. Nonklang, and R. Akada, "High-temperature fermentation: how can processes for ethanol production at high temperatures become superior to the traditional process using mesophilic yeast?," *Appl. Microbiol. Biotechnol.*, vol. 85, no. 4, pp. 861–867, 2010.

[5] R. Vundela Siva, K. Subash Chndra, T. Sudhir Kumar, and P. Narayanlal, "An approach to analyse energy and exergy analysis of thermal power plants: a review," *Smart Grid Renew. Energy*, vol. 2010, 2010.

[6] H. Agalit, N. Zari, and M. Maaroufi, "Suitability of industrial wastes for application as high temperature thermal energy storage (TES) materials in solar tower power plants--A comprehensive review," *Sol. Energy*, vol. 208, pp. 1151–1165, 2020.

[7] H. Zhang, J. Baeyens, G. Cáceres, J. Degreve, and Y. Lv, "Thermal energy storage: Recent developments and practical aspects," *Prog. Energy Combust. Sci.*, vol. 53, pp. 1–40, 2016.

[8] Y.-L. He and T. Xie, "Advances of thermal conductivity models of nanoscale silica aerogel insulation material," *Appl. Therm. Eng.*, vol. 81, pp. 28–50, 2015.

[9] A. Berge and P. Ä. R. Johansson, "Literature review of high performance thermal

insulation," 2012.

[10] J. R. Howell, M. P. Mengüç, K. Daun, and R. Siegel, *Thermal radiation heat transfer*. CRC press, 2020.

[11] Z. Pásztory and others, "An overview of factors influencing thermal conductivity of building insulation materials," *J. Build. Eng.*, vol. 44, p. 102604, 2021.

[12] G. H. Tang, C. Bi, Y. Zhao, and W. Q. Tao, "Thermal transport in nano-porous insulation of aerogel: factors, models and outlook," *Energy*, vol. 90, pp. 701–721, 2015.

[13] R. Nosrati and U. Berardi, "Long-term performance of aerogel-enhanced materials," *Energy Procedia*, vol. 132, pp. 303–308, 2017.

[14] Z. Li, L. Gong, X. Cheng, S. He, C. Li, and H. Zhang, "Flexible silica aerogel composites strengthened with aramid fibers and their thermal behavior," *Mater. \& Des.*, vol. 99, pp. 349–355, 2016.

[15] S. Chakraborty, A. A. Pisal, V. K. Kothari, and A. Venkateswara Rao, "Synthesis and characterization of fibre reinforced silica aerogel blankets for thermal protection," *Adv. Mater. Sci. Eng.*, vol. 2016, 2016.

[16] M. A. Hasan, R. Sangashetty, A. C. M. Esther, S. B. Patil, B. N. Sherikar, and A. Dey, "Prospect of thermal insulation by silica aerogel: a brief review," *J. Inst. Eng. Ser. D*, vol. 98, no. 2, pp. 297–304, 2017.

[17] H. Cai *et al.*, "Preparation of silica aerogels with high temperature resistance and low thermal conductivity by monodispersed silica sol," *Mater. \& Des.*, vol. 191, p. 108640, 2020.

[18] M. Alam, H. Singh, and M. C. Limbachiya, "Vacuum Insulation Panels (VIPs) for building construction industry--A review of the contemporary developments and future directions," *Appl. Energy*, vol. 88, no. 11, pp. 3592–3602, 2011.

[19] W. Villasmil, L. J. Fischer, and J. Worlitschek, "A review and evaluation of thermal insulation materials and methods for thermal energy storage systems," *Renew. Sustain. Energy Rev.*, vol. 103, pp. 71–84, 2019.

[20] R. Baetens *et al.*, “Vacuum insulation panels for building applications: A review and beyond,” *Energy Build.*, vol. 42, no. 2, pp. 147–172, 2010.

[21] S. S. Alotaibi and S. Riffat, “Vacuum insulated panels for sustainable buildings: a review of research and applications,” *Int. J. energy Res.*, vol. 38, no. 1, pp. 1–19, 2014.

[22] X. Lu, M. C. Arduini-Schuster, J. Kuhn, O. Nilsson, J. Fricke, and R. W. Pekala, “Thermal conductivity of monolithic organic aerogels,” *Science (80-.).*, vol. 255, no. 5047, pp. 971–972, 1992.

[23] M. Davraz and H. C. Bayrakci, “Performance properties of vacuum insulation panels produced with various filling materials,” *Sci. Eng. Compos. Mater.*, vol. 21, no. 4, pp. 521–527, 2014.

[24] M. Spinnler, E. R. F. Winter, R. Viskanta, and T. Sattelmayer, “Theoretical studies of high-temperature multilayer thermal insulations using radiation scaling,” *J. Quant. Spectrosc. Radiat. Transf.*, vol. 84, no. 4, pp. 477–491, 2004.

[25] M. Tychanicz-Kwiecień, J. Wilk, and P. Gil, “Review of high-temperature thermal insulation materials,” *J. Thermophys. heat Transf.*, vol. 33, no. 1, pp. 271–284, 2019.

[26] K. Daryabeigi, S. D. Miller, and G. R. Cunnington, “Heat transfer in high temperature multilayer insulation,” 2007.

[27] A. M. Papadopoulos, “State of the art in thermal insulation materials and aims for future developments,” *Energy Build.*, vol. 37, no. 1, pp. 77–86, 2005.

[28] A. Wynn, M. Marchetti, and E. Magni, “INSULATING FIREBRICK-MAXIMISING ENERGY SAVINGS THROUGH PRODUCT SELECTION.,” *Ind. Ceram.*, vol. 31, no. 2, 2011.

[29] F. Modarresifar, P. A. Bingham, and G. A. Jubb, “Thermal conductivity of refractory glass fibres,” *J. Therm. Anal. Calorim.*, vol. 125, no. 1, pp. 35–44, 2016.

[30] P. M. Sutheesh and A. Chollackal, “Thermal performance of multilayer insulation: a review,” in *IOP Conference Series: Materials Science and Engineering*, 2018, vol. 396, no. 1, p. 12061.

[31] T. Miyakita, R. Hatakenaka, H. Sugita, M. Saitoh, and T. Hirai, “Development of a new multi-layer insulation blanket with non-interlayer-contact spacer for space cryogenic mission,” *Cryogenics (Guildf).*, vol. 64, pp. 112–120, 2014.

[32] B. Wang, Y. H. Huang, P. Li, P. J. Sun, Z. C. Chen, and J. Y. Wu, “Optimization of variable density multilayer insulation for cryogenic application and experimental validation,” *Cryogenics (Guildf).*, vol. 80, pp. 154–163, 2016.

[33] B. Deng *et al.*, “Study of the thermal performance of multilayer insulation used in cryogenic transfer lines,” *Cryogenics (Guildf).*, vol. 100, pp. 114–122, 2019.

[34] T. Ji, R. Zhang, B. Sunden, and G. Xie, “Investigation on thermal performance of high temperature multilayer insulations for hypersonic vehicles under aerodynamic heating condition,” *Appl. Therm. Eng.*, vol. 70, no. 1, pp. 957–965, 2014.

[35] M. Spinnler, E. R. F. Winter, and R. Viskanta, “Studies on high-temperature multilayer thermal insulations,” *Int. J. Heat Mass Transf.*, vol. 47, no. 6–7, pp. 1305–1312, 2004.

[36] K. D. Timmerhaus and R. P. Reed, *Cryogenic engineering: fifty years of progress*. Springer Science \& Business Media, 2007.

[37] W. L. Johnson, “Thermal performance of cryogenic multilayer insulation at various layer spacings,” 2010.

[38] Y. Lei, Z. Hu, B. Cao, X. Chen, and H. Song, “Enhancements of thermal insulation and mechanical property of silica aerogel monoliths by mixing graphene oxide,” *Mater. Chem. Phys.*, vol. 187, pp. 183–190, 2017.

[39] J. Feng, D. Chen, W. Ni, S. Yang, and Z. Hu, “Study of IR absorption properties of fumed silica-opacifier composites,” *J. Non. Cryst. Solids*, vol. 356, no. 9–10, pp. 480–483, 2010.

[40] X.-D. Wang, D. Sun, Y.-Y. Duan, and Z.-J. Hu, “Radiative characteristics of opacifier-loaded silica aerogel composites,” *J. Non. Cryst. Solids*, vol. 375, pp. 31–39, 2013.

[41] J.-J. Zhao *et al.*, “Optical and radiative properties of infrared opacifier particles

loaded in silica aerogels for high temperature thermal insulation," *Int. J. Therm. Sci.*, vol. 70, pp. 54–64, 2013.

[42] M. F. Modest and S. Mazumder, *Radiative heat transfer*. Academic press, 2021.

[43] R. G. Hering and T. F. Smith, "Surface radiation properties from electromagnetic theory," *Int. J. Heat Mass Transf.*, vol. 11, no. 10, pp. 1567–1571, 1968.

[44] R. A. Rapp, "The high temperature oxidation of metals forming cation-diffusing scales," *Metall. Trans. A, Phys. Metall. Mater. Sci.*, vol. 15, no. 5, pp. 765–782, 1984.

[45] D. J. Young, *High temperature oxidation and corrosion of metals*, vol. 1. Elsevier, 2008.

[46] R. Peraldi, D. Monceau, and B. Pieraggi, "Correlations between growth kinetics and microstructure for scales formed by high-temperature oxidation of pure nickel. II. Growth kinetics," *Oxid. Met.*, vol. 58, no. 3, pp. 275–295, 2002.

[47] J. C. Ku and J. D. Felske, "The range of validity of the Rayleigh limit for computing Mie scattering and extinction efficiencies," *J. Quant. Spectrosc. Radiat. Transf.*, vol. 31, no. 6, pp. 569–574, 1984.

[48] H. C. Hulst and H. C. van de Hulst, *Light scattering by small particles*. Courier Corporation, 1981.

[49] M. R. Querry, "Optical Constants, contractor report," *US Army Chem. Res. Dev. Eng. Cent. (CRDC), Aberdeen Proving Ground, MD*, vol. 418, 1985.

[50] P. Petrik *et al.*, "Optical Properties of Oxidized, Hydrogenated, and Native Zirconium Surfaces for Wavelengths from 0.3 to 25 $μ$m- A Study by Ex Situ and In Situ Spectroscopic Ellipsometry," *Phys. status solidi*, vol. 216, no. 8, p. 1800676, 2019.

[51] A. D. Rakić, A. B. Djurišić, J. M. Elazar, and M. L. Majewski, "Optical properties of metallic films for vertical-cavity optoelectronic devices," *Appl. Opt.*, vol. 37, no. 22, pp. 5271–5283, 1998.

[52] L. Lajaunie, F. Boucher, R. Dessapt, and P. Moreau, "Strong anisotropic influence

of local-field effects on the dielectric response of \$α\$-MoO 3," *Phys. Rev. B*, vol. 88, no. 11, p. 115141, 2013.

[53] L. Gao, F. Lemarchand, and M. Lequime, "Exploitation of multiple incidences spectrometric measurements for thin film reverse engineering," *Opt. Express*, vol. 20, no. 14, pp. 15734–15751, 2012.

[54] T. Siefke *et al.*, "Materials pushing the application limits of wire grid polarizers further into the deep ultraviolet spectral range," *Adv. Opt. Mater.*, vol. 4, no. 11, pp. 1780–1786, 2016.

[55] E. Masetti, A. M. Piegari, and A. Tirabassi, "Optical characterization of low-absorbing thin films in the visible and infrared spectrum," in *Optical thin films and applications*, 1990, vol. 1270, pp. 125–132.

[56] M. A. Ordal, R. J. Bell, R. W. Alexander, L. A. Newquist, and M. R. Querry, "Optical properties of Al, Fe, Ti, Ta, W, and Mo at submillimeter wavelengths," *Appl. Opt.*, vol. 27, no. 6, pp. 1203–1209, 1988.

[57] Y. Nigara, "Measurement of the optical constants of yttrium oxide," *Jpn. J. Appl. Phys.*, vol. 7, no. 4, p. 404, 1968.

[58] M. A. Ordal, R. J. Bell, R. W. Alexander, L. L. Long, and M. R. Querry, "Optical properties of Au, Ni, and Pb at submillimeter wavelengths," *Appl. Opt.*, vol. 26, no. 4, pp. 744–752, 1987.

[59] M. R. Querry, *Optical constants of minerals and other materials from the millimeter to the ultraviolet*. Chemical Research, Development \& Engineering Center, US Army Armament~…, 1987.

[60] J. H. Weaver, C. G. Olson, and D. W. Lynch, "Optical investigation of the electronic structure of bulk Rh and Ir," *Phys. Rev. B*, vol. 15, no. 8, p. 4115, 1977.

[61] J. I. Larruquert, A. P. Pérez-Mar\'\in, S. Garc\'\ia-Cortés, L. Rodr\'\iguez-de Marcos, J. A. Aznárez, and J. A. Méndez, "Self-consistent optical constants of sputter-deposited B 4 C thin films," *JOSA A*, vol. 29, no. 1, pp. 117–123, 2012.

[62] G. Boyd, H. Kasper, and J. McFee, "Linear and nonlinear optical properties of

AgGaS 2, CuGaS 2, and CuInS 2, and theory of the wedge technique for the measurement of nonlinear coefficients," *IEEE J. Quantum Electron.*, vol. 7, no. 12, pp. 563–573, 1971.

[63] M. Veszelei, K. Andersson, C.-G. Ribbing, K. Järrendahl, and H. Arwin, "Optical constants and Drude analysis of sputtered zirconium nitride films," *Appl. Opt.*, vol. 33, no. 10, pp. 1993–2001, 1994.

[64] S. Adachi, "Optical dispersion relations for GaP, GaAs, GaSb, InP, InAs, InSb, Al x Ga1- x As, and In1- x Ga x As y P1- y," *J. Appl. Phys.*, vol. 66, no. 12, pp. 6030–6040, 1989.

[65] J. I. Larruquert, A. P. Pérez-Mar\'\in, S. Garc\'\ia-Cortés, L. Rodr\'\iguez-de Marcos, J. A. Aznárez, and J. A. Méndez, "Self-consistent optical constants of SiC thin films," *JOSA A*, vol. 28, no. 11, pp. 2340–2345, 2011.

[66] J. M. Khoshman and M. E. Kordesch, "Optical characterization of sputtered amorphous aluminum nitride thin films by spectroscopic ellipsometry," *J. Non. Cryst. Solids*, vol. 351, no. 40–42, pp. 3334–3340, 2005.

[67] F. Wooten, *Optical properties of solids*. Academic press, 2013.

[68] M. Strømme, R. Karmhag, and C. G. Ribbing, "Optical constants of sputtered hafnium nitride films. Intra-and interband contributions," *Opt. Mater. (Amst).*, vol. 4, no. 5, pp. 629–639, 1995.

[69] C. Wong, Y. Y. Teng, J. Ashok, and P. L. H. Varaprasad, "Barium titanate (BaTiO3)," in *Handbook of Optical Constants of Solids*, Elsevier, 1997, pp. 789–803.

[70] W. J. Tropf and M. E. Thomas, "Aluminum oxynitride (ALON) spinel," in *Handbook of Optical Constants of Solids*, Elsevier, 1997, pp. 777–787.

[71] J. I. Larruquert *et al.*, "Transmittance and optical constants of erbium films in the 3.25- 1580 eV spectral range," *Appl. Opt.*, vol. 50, no. 15, pp. 2211–2219, 2011.

[72] D. L. Windt *et al.*, "Optical constants for thin films of ti, zr, nb, mo, ru, rh, pd, ag, hf, ta, w, re, ir, os, pt, and au from 24 åto 1216 å," *Appl. Opt.*, vol. 27, no. 2, pp.

246–278, 1988.

[73] M. Vidal-Dasilva *et al.*, "Transmittance and optical constants of Tm films in the 2.75--1600 eV spectral range," *J. Appl. Phys.*, vol. 105, no. 10, p. 103110, 2009.

[74] T. J. Bright *et al.*, "Infrared optical properties of amorphous and nanocrystalline Ta2O5 thin films," *J. Appl. Phys.*, vol. 114, no. 8, p. 83515, 2013.

[75] J. Kischkat *et al.*, "Mid-infrared optical properties of thin films of aluminum oxide, titanium dioxide, silicon dioxide, aluminum nitride, and silicon nitride," *Appl. Opt.*, vol. 51, no. 28, pp. 6789–6798, 2012.

[76] B. Sabir, G. Murtaza, and R. M. A. Khalil, "Ab-initio prediction of structure stability, electromagnetic, optical and thermoelectric behavior of orthorhombic LaXO3 (X= Cr, Mn, Fe): For device application," *J. Mol. Graph. Model.*, vol. 94, p. 107482, 2020.

[77] D. F. Edwards and E. Ochoa, "Infrared refractive index of silicon," *Appl. Opt.*, vol. 19, no. 24, pp. 4130–4131, 1980.

[78] G. Hass and C. D. Salzberg, "Optical properties of silicon monoxide in the wavelength region from 0.24 to 14.0 microns," *JOSA*, vol. 44, no. 3, pp. 181–187, 1954.

[79] M. M. Abu-Romia and C. L. Tien, "Appropriate mean absorption coefficients for infrared radiation of gases," 1967.

[80] M. Fox, "Optical properties of solids." American Association of Physics Teachers, 2002.

[81] http://en.kdone.net/ceratech/product_view?Seq=106

[82] http://insulationet.com/en/materials/high-temperature-wool/

[83] https://www.americanelements.com/meltingpoint.html/

[84] https://www.crystran.co.uk/optical-materials/sapphire-al2o3

[85] https://www.omega.co.uk/literature/transactions/volume1/emissivitya.html

[86] https://www.mtm-inc.com/using-mli-blankets-under-poor-vacuum-conditions.html

[87] https://conceptgroupllc.com/mli-takes-our-high-temp-vacuum-insulation-to-the-next-level/